THE FAR INFRARED ABSORPTION SPECTRUM OF SILICON AND GERMANIUM UNDER HIGH OPTICAL EXCITATION

by

© Hugo Ricardo Navarro-Contreras

A Thesis

Submitted to the School of Graduate Studies

in Partial Fulfilment of the Requirements

for the Degree

Doctor of Philosophy

McMaster University

September 1979

THE FAR INFRARED ABSORPTION SPECTRUM OF SILICON AND GERMANIUM UNDER HIGH OPTICAL EXCITATION

DOCTOR OF PHILOSOPHY
(Physics)

McMASTER UNIVERSITY
Hamilton, Ontario

TITLE: The Far Infrared Absorption Spectrum of Silicon and Germanium Under High Optical Excitation

AUTHOR: Hugo Ricardo Navarro Contreras
B.Sc. (Universidad Autonoma de San Luis Potosi, Mexico)

M.Sc. (Centro de Investigacion y de Estudios Avanzados del IPN, Mexico)

SUPERVISOR: Dr. T. Timusk

NUMBER OF PAGES: xiii, 176

ABSTRACT

A study has been conducted, at low temperatures, of the far infrared absorption spectrum of silicon and germanium under high optical excitation. This work presents the first experimental observation of the absorption of both the gas of indirect excitons and the electron-hole drops (EHD) in silicon. Using the strength of the exciton absorption, a study of the coexistence of the exciton gas with the EHD was undertaken. For germanium, the absorption spectra produced by excitons and the behaviour of the exciton transitions in the presence of a small magnetic field were measured. The experimental excitonic absorption spectra in both silicon and germanium are compared with the results of the effective mass Hamiltonian model and it is found that the results of this model account well for the observed structure in both materials. A model for the response of the exciton levels to an externally applied magnetic field was developed. The comparison of the experimental results provided a check on the identification of the observed transitions between 1S to 2P exciton states in germanium. The absorption spectrum produced by EHD in silicon is compared with a calculated spectrum using the Mie theory for the absorption of radiation by small particles. The calculation included both interband and intraband transi-

tions for the valence bands. The agreement with the experiment is good and justifies an estimate of the value of the electron-hole density inside the drops in silicon. As a result of the study of the coexistence of the exciton gas with the EHD, estimates could be done for the radius of the drops in silicon.

ACKNOWLEDGEMENTS

I would like to thank Dr. T. Timusk for his supervision of this work.. I would especially like to thank Dr. D. Goodings for many helpful discussion and encouragement, as well as for his patience in reviewing the English of a substantial part of this thesis. The cooperation of Dr.C.Stager, K. Locke and R. Dinser in reviewing the English of some sections of this manuscript is also gratefully acknowledged.

I am also grateful to G. Zarate for kindly providing me with a copy of her program to calculate the dielectric constant, and to Mrs. H. Kennelly and Mrs. S. Saracini for typing the manuscript.

I thank the Consejo Nacional de Ciencia y Technologia (CONACYT), de Mexico and to the Universidad Autonoma de Puebla for their financial support.

Finally, I must thank my wife, Rocio, for her help in editing the manuscript, as well as for her unlimited patience and understanding throughout the time I was engaged in this work.

TABLE OF CONTENTS

LIST OF FIGURES

LIST OF TABLES

CHAPTER I

INTRODUCTION

It has long been recognized that when some semiconductors are subjected to an optical excitation, with radiation of energy larger than the band gap, two interesting phenomena may appear. One is the electrostatic binding of an electron and a hole to constitute an exciton. The other is that for large exciton densities at low enough temperatures, the excitons can condense into small drops of electron-hole fluid, called electron-hole drops (EHD) (Keldysh 1968). These two phenomena appear in germanium and silicon, as well as in some other semiconductor materials. Both excitons and EHD in those two materials absorb radiation in the far infrared region of the electromagnetic spectrum.

The absorption spectrum of an exciton is determined by its quantum energy levels. The absorption spectrum of of the EHD is determined by the polarization produced on the drops by the incident radiation. This response, in turn, depends on the possible internal transitions in the electron and hole bands at the energy of the incident radiation.

In this work an experimental study of the absorption spectra produced by excitons in germanium and by excitons and EHD in silicon is presented. This study is aimed at contributing to the understanding of the quantum structure of the indirect excitons in these two materials. Also, with respect to the EHD in Si, this study provides a new experimental result which is used to check the current understanding of the absorption mechanisms for these drops and the physical parameters that affect this absorption. The theoretical determination of the exciton energy levels in a semiconductor with degenerate valence bands, as in germanium and silicon, was first considered by G. Dresselhaus (1956) in the effective mass approximation. In this model the effect of the crystal structure is taken into account by assuming that the electron in the conduction band can be described as a particle with a negative charge and a mass determined by the local curvature of the band. A similar assumption is made for the hole in the valence band, assigning it a positive charge. It is also assumed that the electron and the hole interact according to the Coulomb law, modified by the static dielectric constant of the crystal. Dresselhaus made the first rough estimates for the binding energies of indirect excitons in both Ge and Si. McLean and Loudon (1960) classified the exciton states for these two materials, according to their symmetry properties, and calculated the two possible ground state energies using variational techniques in the effective mass approximation. The indirect excitons were experimentally detected in Ge (1957) and Si (1959) by MacFarlane, McLean, Quarrington and Roberts by looking at the absorption edge of these materials. Button et al. (1959) detected the two ground states of indirect excitons in germanium and studied their Zeeman effect, looking at the slope of the transmission curve in this material. Shaklee and Nahory (1970) measured, at high resolution, the derivative of the indirect absorption edge in silicon and from that work they obtained the value of the binding energy of the lowest ground state of the exciton. They also measured the energy separation between the ground state and one of the two possible 2S states. Recently a series of experiments have given a lot of information on the exciton structure in Ge. These are the far infrared absorption experiments of Vavilov et al. (1973), Kononenko et al. (1974) and Buchanan and Timusk (1976). The spectra from these experiments provided a wealth of resolved structure that could be compared to more detailed calculations of the exciton spectrum in germanium. Kobayashi and Narita (1976) reported an almost structureless emission in the far infrared in silicon centered at 11.5 meV, that they interpreted as $2P \rightarrow 1S$ exciton transitions.

A very comprehensive theoretical treatment in the effective mass approximation, aimed at providing a complete description of the energy states of the excitons in Ge and Si, has been developed by Lipari and Altarelli (LA) (1976-1977). Their work provides a lot of physical insight into the role played by the different interactions that contribute to the energy of the exciton quantum levels. Their results for the exciton transitions in Ge are in good agreement with most of the observed transitions in the far infrared experiments. Their model also provides a quantum characterization of the most important exciton states, which is very useful in describing the response of these states to externally applied fields.

The first experimental observation leading to the identification of the presence of EHD in silicon was done by Pokrovskii and Svistunova (1969). They looked at the band edge recombination luminiscence for this material. Vavilov, Zayats and Murzin (1969) first observed the absorption spectrum of the EHD in Ge. They explained their observations in terms of heavily damped plasma oscillations of the electron-holes. Their experimental result was later confirmed by Timusk and Silin (1975) who also studied the far infrared absorption of the EHD in doped germanium samples. To completely explain the observed line shape of the absorption, Murzin et al. (1975) and Rose et al. (1975) included interband transitions in the valence band along with damped plasma oscillations, as absorbing mechanisms. Zarate and Timusk (1979) have used this model sucessfully to fit the complete absorption curve of the EHD in Ge.

Although the EHD in silicon and germanium were first observed almost simultaneously, very few physical parameters of the drops in silicon are known in contrast to the extensive results which have been obtained for germanium. Recently from several experiments, Dite et al. (1976) and Shah et al. (1977) have constructed the phase diagram for the exciton gas and the EHD in silicon, showing the coexistence boundary. These two works improved this situation somewhat. This thesis presents a study of the exciton concentration or density of the gas of excitons in coexistence with EHD in silicon. The observed concentrations are analyzed using Pokrovskii's model (1972) for the rate of change of the concentrations with time of excitons and electron-hole pairs in the drops.

In Chapter two of this thesis a description of the experimental techniques used is given. Chapter three describes the theoretical model of Lipari and Altarelli for indirect excitons. Chapter four presents and discusses the experimental results for the indirect exciton spectrum in Ge and its response to a magnetic field. A model is also proposed to analyze the magnetic experiments. Chapter five presents the first experimental observation of the spectra of indirect excitons in silicon. The measured variation with temperature of the concentration of an exciton gas in coexistence with the EHD is also presented in this chapter. Finally, Chapter six presents and discusses the first observation of EHD far infrared absorption and the fit of the theory.

CHAPTER II

EXPERIMENTAL PROCEDURE

1. Introduction

A high concentration exciton gas was generated in silicon and germanium by optically pumping one of the surfaces. The laser operates at wavelengths that correspond to photon energies larger than the energies of the band gaps of the materials considered. For silicon, a krypton laser (Spectra-Physics) operating at a red line of wavelength 6471 Å (which corresponds to photons of energy 1.92 eV) was used. The indirect band gap in this material is 1.17 eV at 0 K. Incident powers at the sample ranged between 100 mW to 500 mW with the laser focused at a 1 mm^2 spot. For germanium, a commercial (SYLVANA) CW neodynium YAG: laser also focused to a spot of 1 mm^2 was used. The wavelength of this laser is 1.06 μm and corresponds to an energy of 1.17 eV. The band gap energy in germanium is 0.744 eV at 0 K. The incident power at the sample in this case varied from 30 mW to 90 mW.

In silicon, the measurements were done at temperatures in the range of 5K to over 20K. For this material at these temperatures, the exciton gas coexists with drops of condensed electron-hole fluid. Hence, the absorption of this phase could also be observed and studied. The measurements in germanium were conducted mainly at 4.2 K. At this temperature in this material, the electron-hole drops have almost completely evaporated and their absorption spectrum is unobservable.

The absorption is obtained by taking the natural logarithm of the ratio of the spectrum with the laser off, represented by $I_o(\omega)$ (background), to the spectrum obtained with the laser on; i.e., with the exciton gas and the EHD present, represented by $I(\omega)$. This logarithm is related to the absorption constant α by $\ln(I_o/I) = \alpha d$, where d is the thickness of the absorbing region. Typical values of the overall absorption signal produced by the exciton gas together with the EHD in silicon varied from 0.5% to 3% of the total radiation incident on the detector. The exciton gas in germanium produced absorption of 8% to 20% of the spectral region of interest.

2. Samples

A high purity silicon crystal (donated by Hughes Aircraft Co.), of resistivity 30,000 Ohm-cm, and dimensions of 26 mm diameter, 1.4 mm thick, was used. It had an estimated concentration of less than 10^{12} cm^{-3} electrical active impurities. The estimate was done using the resistivity tables for Si (Irvin 1962). The circular faces of this wafer were <111> faces. One of the surfaces was carefully polished to a finish of one micron. Before each experiment, this surface was polished with syton (a commercial polish of Dow Corning Co.), and then etched with CP4, a mixture of 10% hydrofluoric acid, 20% glacial acetic acid, and 60% of nitric acid.

The germanium sample was a very high purity crystal with a concentration of electrical active impurities, estimated (in the same way as for Si), to be less than 2×10^{10} cm^{-3}. Its dimensions are 3 x 15 x 15 mm (purchased from General Electric Company, Valley Forge, Pa.). The flat surfaces had a <100> orientation. The surface facing the incoming radiation was also polished to a finish of 1 micron. Every three to four experiments, the surface of the sample had degraded in quality and had to be repolished with syton and etched with CP4.

3. Optics

The far infrared absorption measurements were done using Fourier transform spectroscopy. A Michelson interferometer was used over the spectral ranges of 5 to 45 meV (40 to 360 cm^{-1}). A lamellar grating interferometer was used in the range of 1.2 to 5 meV (10 to 40 cm^{-1}). The Michelson interferometer is a commercial instrument (RIIC FS 720) modified with a stepping motor drive (Slo-Syn HS25V) guided through an interface by the commands of a minicomputer. The lamellar interferometer is also a commercial instrument (Beckman LR100) with the same stepping motor driven by the same system.

For the Michelson, many of the measurements on excitons in silicon were done using a FCS (SYLVANIA) tungsten halogen lamp as a source of light. For reasons of stability, a SM35 (American Ultraviolet Co.) mercury arc lamp with a fused quartz envelope later proved to be superior. Later on, both interferometers used this lamp as a source of light.

The light of frequency over 700 cm^{-1} was filtered with black polyethylene after going through the sample and before reaching the detector. This is done to eliminate radiation of unwanted frequencies which would otherwise overwhelm the far infrared signal. For most experiments, a sapphire window was used which eliminated the radiation above 360 cm^{-1} (45 meV). For the EHD in pure silicon studies, the sapphire window was replaced by a silicon window that transmitted radiation below 700 cm^{-1} (85 meV), when used with a beamsplitter of Mylar of 3.5 μm in thickness. This beamsplitter has a first minimum of reflected energy at 840 cm^{-1}. For the other experiments in the Michelson, a 50 G (12 μm) Mylar beamsplitter that gives a maximum at 120 cm^{-1} (15 meV) and a minimum at 240 cm^{-1} (30 meV) of reflected radiation, was used. In some cases, the spectral region was further reduced using alkalide-halide filters wedged to 1 or 2 degrees and 1 to 2 mm in thickness. The wedge is done to avoid internal multiple reflections from creating spurious maxima in the signal (interferogram). NaCl was used to cut frequencies over 170 cm^{-1} (21.0 meV). KCl in series with a LiF filter were used to eliminate frequencies over 140 cm^{-1} (17.5 meV).

4. Experimental Set-Up

The experimental set-up was required to incorporate the following features: firstly, it had to hold the sample. Secondly, it had to allow both the laser and far infrared beams to hit the same well-defined area of the crystal. Thirdly, it had to conduct the enormous heat generated by the laser away from the sample. Fourthly, it was necessary to capture the emerging far infrared radiation from the sample but prevent unwanted radiation from reaching the detector and producing unnecessary noise. How this is accomplished is illustrated in the description of the cryostat used, given below.

A stainless steel cryostat was used to do all measurements. A drawing of the system is shown in Fig. 2-1. The cryostat is designed to fit inside a glass liquid He^4 dewar 4" in diameter. The cryostat consists of two separate vacuum-tight chambers - a large sample chamber, in which a light pipe that supports the sample is inserted; and the detector chamber. The two chambers communicate through a 1/4" hole at the bottom of the sample chamber. This hole is covered and vacuum-sealed with a stainless steel flange that has the sapphire or silicon window centered with the hole. The seal is done with an indium O-ring .05" in diameter. The seal was done very carefully to be leak-tight at low temperatures. This prevented any He^4 from getting into the detector chamber and putting the detector in thermal communication with the rest of the

Figure 2-1

Inside look of the cryostat used in the experiments. The sample is mounted near the bottom of the sample chamber in strong thermal contact with the sample holder. The interior of the He^3 can that cools the detector is also shown. The detector is almost completely thermally isolated from the cryostat. It is only weakly thermally coupled to the base of the He^3 liquid can by the copper leads.

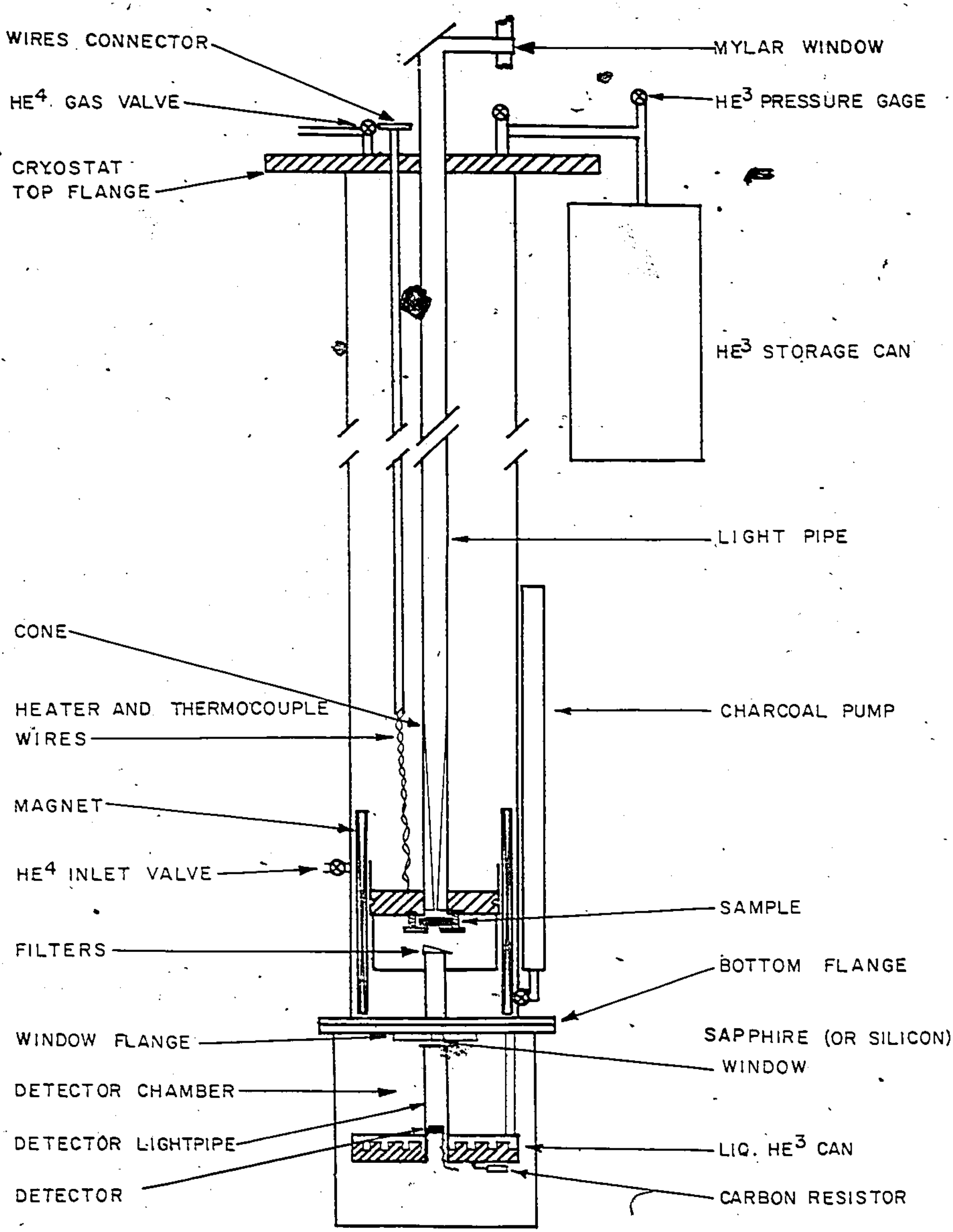
WIRES CONNECTOR
HE4 GAS VALVE
CRYOSTAT TOP FLANGE
MYLAR WINDOW
HE3 PRESSURE GAGE
HE3 STORAGE CAN
LIGHT PIPE
CONE
HEATER AND THERMOCOUPLE WIRES
CHARCOAL PUMP
MAGNET
HE4 INLET VALVE
SAMPLE
FILTERS
BOTTOM FLANGE
WINDOW FLANGE
SAPPHIRE (OR SILICON) WINDOW
DETECTOR CHAMBER
DETECTOR LIGHTPIPE
LIQ. HE3 CAN
DETECTOR
CARBON RESISTOR

cryostat. There is an inlet valve 4" above the bottom of the sample chamber. This valve can be operated from outside the cryostat. This valve is opened when the experiment is to be done with the sample submerged in liquid He^4.

The detector chamber is a stainless steel can machined out of one piece, 3" in height by 3" in diameter. It is screwed to the bottom flange of the cryostat, as shown in Fig. 2-1. An indium O-ring seal was used to make it leak-tight. It was found that steel screws have to be torqued to above 25 foot pounds to achieve a reliable seal with 0.06" diameter indium wire. The detector chamber was pumped to a pressure of the order of 10^{-6} Torr. The vacuum was done through a 1/4" diameter stainless steel tube located outside the cryostat, that extended all the way through the top flange. A valve outside the cryostat closed this tube. After achieving this vacuum, a few Torrs of hydrogen gas were admitted to the detector chamber in the cooling process of the system, in order to provide thermal contact with the rest of the cryostat. This tube was also used to conduct the leads for the detector, and a calibrated carbon resistor (Speer 470 Ω) was used to measure the temperature of the detector chamber. The detector leads are miniature coaxial cables 0.006" in diameter. The resistor leads are 0.003" diameter copper, teflon-coated wires (Omega Eng. Inc.).

The detector (Fig. 2-1) is a doped germanium bolometer for use at 0.3 K (Drew and Sievers, 1967). The detector is cooled by a closed He^3 refrigeration system. This system consists of a storage can, a charcoal pump and a liquid He^3 condensing can. The storage of He^3 gas is in a can 6" long by 3" in diameter. This can contains most of the gas at room temperature and at a pressure of 60 lbs/inch^2. It is located outside at the top of the cryostat, as shown in Fig. 2-1. This storage is connected via a 1/4" diameter stainless steel tube to the liquid He^3 can inside the detector chamber. This can consists of two pieces: the top cover made out of stainless steel, and the base which was machined from a solid piece of copper with grooves extending upwards to increase the area of thermal contact between the copper and the liquid He^3. To lower the temperature of the liquid He^3 to 0.3K, the He^3 gas is pumped by a charcoal adsorption pump. This pump consists of a stainless steel can 6" long and 1/2" diameter, positioned 2" above the detector chamber (Fig. 2-1). Inside the can, there is activated charcoal loosely packed in copper mesh bags to allow access of the gas to as much charcoal surface as possible. The pump is connected to the liquid He^3 can and the main storage through a 1/4" bellows valve (Nupro SS 4UW-SW), which can be operated from outside the cryostat.

The liquid He^3 can has a 1/2" diameter hole. At the top of the stainless steel cap of the can, a brass cone of 1/4" interior diameter, is soldered in alignment with this hole. This cone extends to almost touch the sapphire or silicon window at the top, leaving a clearance of about 1 mm between them. This arrangement captures most of the radiation transmitted by the window. At the back of the cone, a small brass disk is screwed onto the He^3 can. The detector is attached to this small disk and the leads pass through a small orifice in it.

To start the operation of the detector, the following procedure was followed. With the He^3 valve closed, the whole cryostat was left to cool down to liquid nitrogen temperature by keeping the outer jacket of the glass dewar filled with the liquid nitrogen. When the whole cryostat was below the ice point, He^4 cold gas which had evaporated from a liquid He^4 bath was allowed to flow through to avoid condensation of water or solid nitrogen. In the meantime, the temperature of the detector was monitored measuring the thermal emf developed between the copper lead connected to the carbon resistor inside the detector chamber, and the stainless steel wall of the cryostat. When this emf stabilized, indicating that the cryostat was in thermal equilibrium with the 4.2 K He^4 gas, liquid helium was transferred to the glass dewar, filling the space outside the cryostat. Pumping over the He^4 gas, the temperature was lowered to 1.2 K. After the transfer of the liquid He^4, the thermal emf was counterbalanced with a differential voltmeter (Hewlett-Packard 3420B), and by passing a current of one micro-ampere through the carbon resistor, the temperature of the detector was measured. When the temperature of the detector was 1.2 K, the He^3 has condensed, and the charcoal pump valve was then opened to start pumping on the He^3. This finally lowers the temperature of the detector to 0.3 K.

The sample is sandwiched between indium pads to improve the thermal contact with the sample holder. While the sample is in He^4 exchange gas, a very good thermal path to He^4 liquid is needed to carry away the heat from the laser. To measure the temperature of the sample, a copper-gold with 0.07% Fe thermocouple was used. It was placed very close to the small aperture of the cone and pressed between the indium pad covered with a small piece of dielectric tape, and the sample. This thermocouple was calibrated using a (Lake Shore Cryotronics - CGR 1-10000) calibrated resistor. The thermal emf of this thermocouple was measured in all experiments, using a 0°C bath, formed of ground ice and cold water as a reference point. It was found that monitoring the temperature was very essential when there was exchange gas in the sample chamber. The operation of the laser always heated the samples appreciably. To care for this, the temperature of the sample was always kept constant by the use of the electrical heater. Thus, if the temperature of the sample varied, there was always the possibility to restore the original temperature, changing the power output of the heater.

The magnet consists of a superconducting coil wound around an aluminum cylinder, of 4500 turns, 3" long and 2.15" in diameter. The magnet was placed around the sample holder and could be slid into position so as to have the sample halfway between the ends (see Fig. 2-2). The superconducting leads and the copper leads that bring the current to the magnet were soldered to two heavy copper rings of 1" length and 1" diameter, to help in the dissipation of the heat generated by the current on the leads. With this arrangement, magnetic fields as high as 15 KOe at 4.2 K were easily achieved with the magnet in exchange gas.

The brass light pipe is inserted into the cryostat (Fig. 2-1). The pipe has a brass flange soldered at the top which is screwed and secured at the top flange of the cryostat. The sample holder plate is attached at the bottom of this pipe. The light pipe has a 3/4" outer diameter at the outside of the cryostat and narrows to 1/2" diameter for most of the length that goes inside the cryostat. The sample holder is a heavy copper disk designed to help in the heat dissipation of the sample. At the top of the brass flange, a Cajon-Ultra-Torr connector is allowed to pass through a stainless steel pipe of 1/4" diameter pipe. This tube carries the leads for a heater, which is wrapped around the sample holder (Fig. 2-2) and the wires of the thermocouple. In the magnetic field experiments, another Cajon connector is used to bring in the leads which feed the current to a superconducting magnet around the sample holder (shown in Figs. 2-1 and 2-2). The sample holder and the sample are covered

Figure 2-2

Diagram of the sample set-up in the magnetic experiments. The figure shows an inner view of the magnet with the sample holder inserted. In the magnetic experiments, no filter was used except for black polyethylene to block radiation above 700 cm^{-1}.

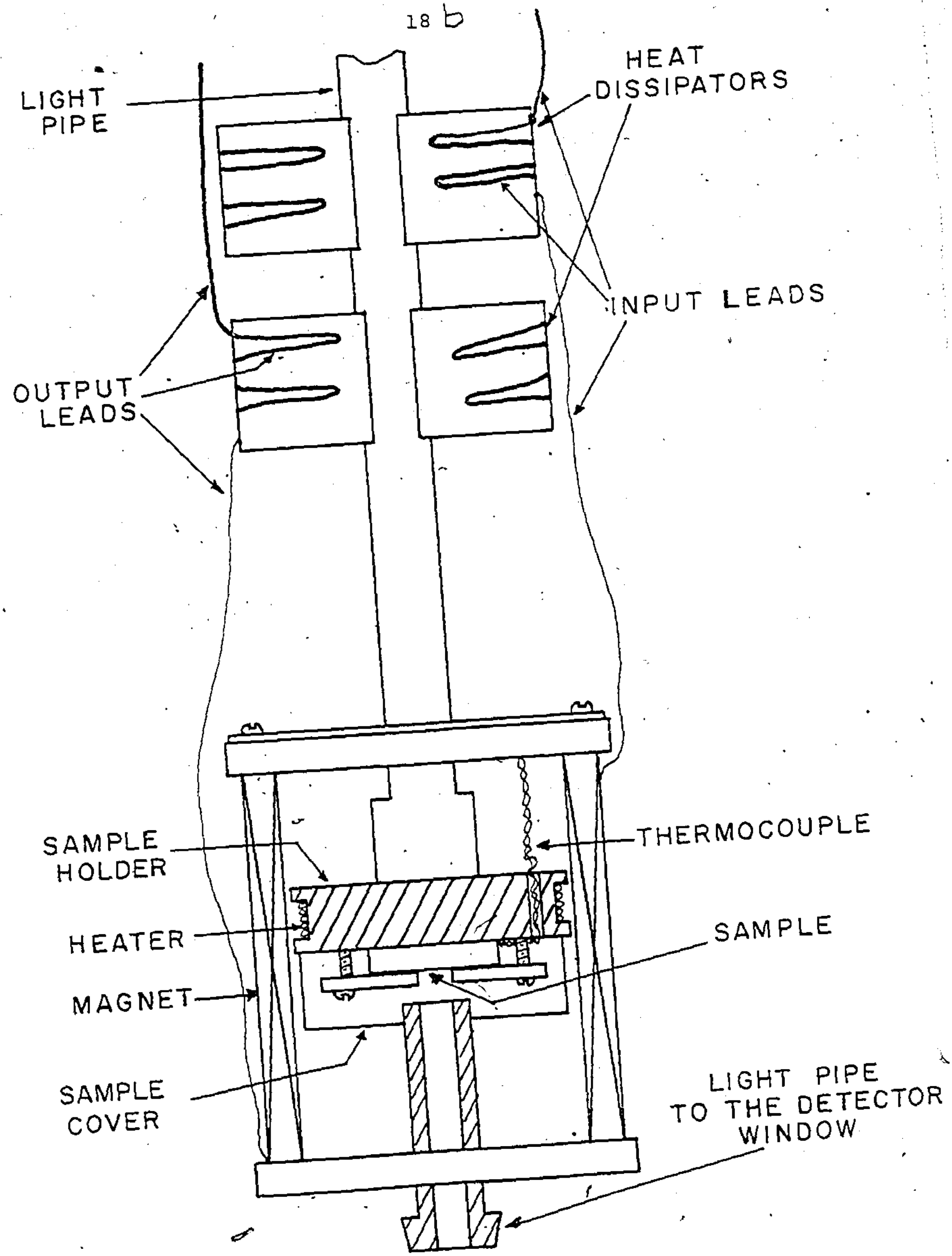
LIGHT PIPE
HEAT DISSIPATORS
INPUT LEADS
OUTPUT LEADS
SAMPLE HOLDER
THERMOCOUPLE
HEATER
SAMPLE
MAGNET
SAMPLE COVER
LIGHT PIPE TO THE DETECTOR WINDOW

with a brass-made cap. The cap has a pipe at the centre. The pipe is a brass rod with a 1/4" hole bored through it. The function of the cap is to prevent stray radiation from reaching the detector. This pipe is brought almost into contact with the detector window. The function of this pipe is to collect the radiation passing through the sample and bring it to the detector. At the top end of this small pipe, facing the sample, the filters are placed with the black polyethyelene wrapped around and securely fastened with teflon tape. The sample chamber could be connected to the helium gas evaporated from the liquid He^4 bath outside the cryostat, through the valve at the top of the flange shown at the left in Fig. 2-1, and work in exchange gas conditions.

The radiation from the interferometer is fed through the window at the top of the light pipe, indicated in the upper right side of Fig. 2-1. This window was (for most of the measurements) a solid piece of white high density polyethyelene of 1 mm thickness. For the measurements with the lamellar interferometer, a Mylar window of 25 G (6 μm) was used. The radiation is reflected towards the bottom at the flat mirror at 45° of the incoming radiation, as shown in Fig. 2-1. This mirror is a polished brass piece with a hole covered with a piece of microscope slide glass (Can-Lab) of 1 mm thickness. The function of this window is to admit the laser beam used to create the population of excitons and EHD in the sample under study. At the bottom of the light pipe, the far infrared radiation is condensed to pass through the sample by a cone of either 1/8" or 1/16" diameter at the narrow part. The sample is held in place by a square copper piece thermally connected to the sample holder disk by braided copper soldered to both pieces. This cover has a 3/8" hole to allow the passage of radiation towards the filters and the detector.

5. Data Collection and Processing System

The signal arriving to the germanium bolometer is amplified by a Brookdeal 450 low noise preamplifier and averaged by a Brookdeal 411 lock-in amplifier with a time-constant, typically 0.3 or 1 second. The radiation is chopped inside the interferometer. The reference signal for the lock-in amplifier is obtained using a light emitting diode LED and a phototransistor. They are mounted in a small holder in the back of the chopper facing the blades. The light of the emitting diode is reflected by a stripe of white paint that is painted on each blade. The chopper is driven by a synchronous motor with a variable frequency power supply to permit chopper frequencies in the range of 30 to 120 Hz. The chopper is located between the mercury lamp and the interferometer.

A block diagram of the complete data collection and processing system is shown in Fig.2-3. The diagram shows that a Data General Corporation Nova-2 minicomputer controls the

Figure 2-3

Block diagram of the data acquisition and processing system. The NOVA 2 minicomputer controls the execution of the experiments through the series of interfaces shown next to it. It also performs the fourier transform of the interferograms as they are collected. The average spectrum obtained is displayed in an oscilloscope connected to the display interface.

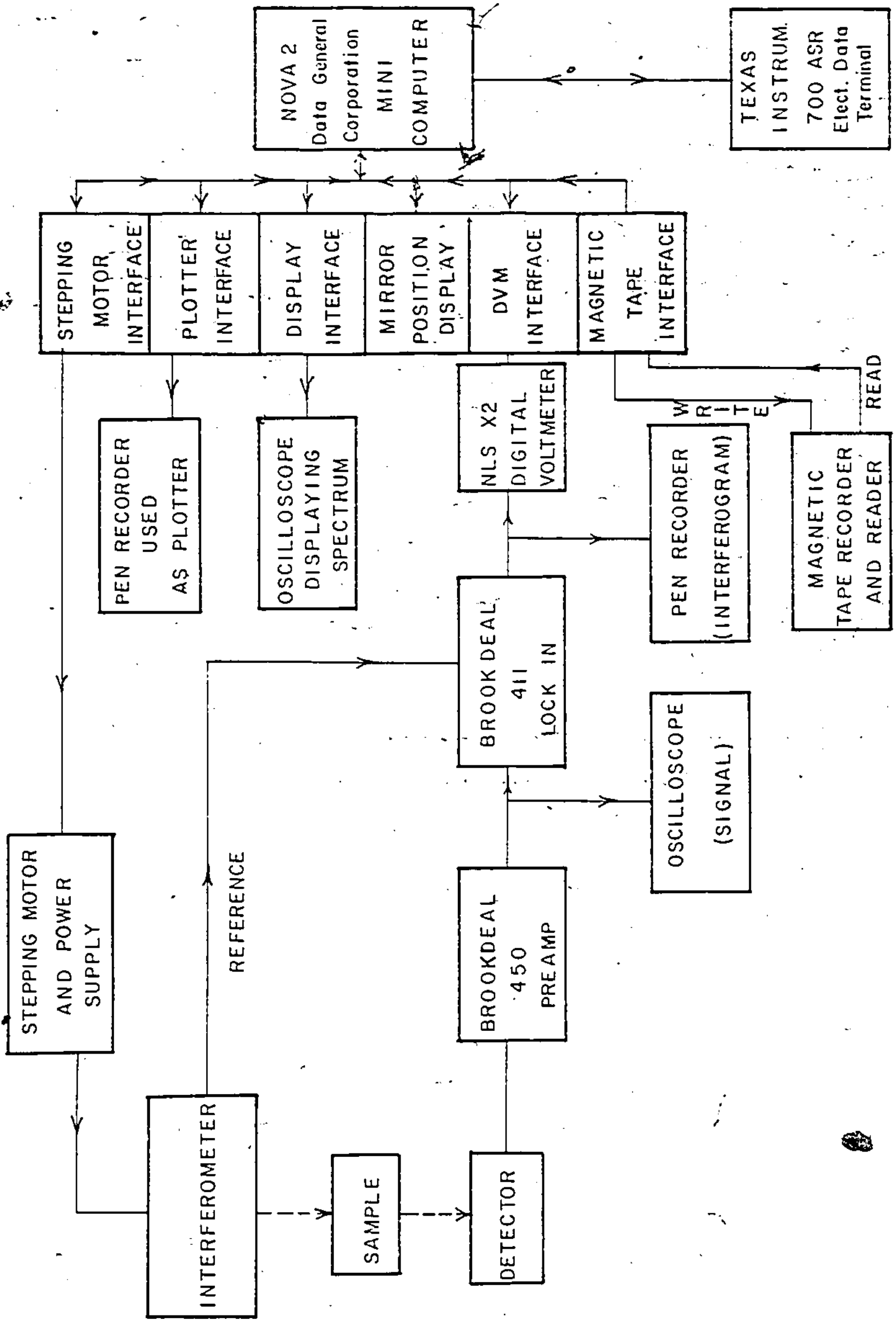
NOVA 2
Data General
Corporation
MINI
COMPUTER
TEXAS
INSTRUM.
700 ASR
Elect. Data
Terminal
STEPPING
MOTOR
INTERFACE
PLOTTER
INTERFACE
DISPLAY
INTERFACE
MIRROR
POSITION
DISPLAY
DVM
INTERFACE
MAGNETIC
TAPE
INTERFACE
PEN RECORDER
USED
AS PLOTTER
OSCILLOSCOPE
DISPLAYING
SPECTRUM
NLS X2
DIGITAL
VOLTMETER
WRITE
READ
PEN RECORDER
(INTERFEROGRAM)
MAGNETIC
TAPE RECORDER
AND READER
BROOK DEAL
411
LOCK IN
OSCILLOSCOPE
(SIGNAL)
STEPPING MOTOR
AND POWER
SUPPLY
REFERENCE
BROOKDEAL
450
PREAMP
INTERFEROMETER
SAMPLE
DETECTOR

execution of the experiment through a series of interfaces. These interfaces are used to transmit commands from the minicomputer to the devices used in the performance of the experiment. They also receive the information sent by the devices and transmit it to the minicomputer. To run the experiment, the minicomputer uses a program written in CALL*BASIC (Thewalt, 1972). This language is a modification of SINGLE USER BASIC of Data General Corporation, to allow the interaction between BASIC and subroutines written in machine language used to control the peripheral devices. A detailed description of the stepping motor interface which was constructed for this project, is given in Appendix A. It serves as an illustration of the organization of an interface.

In a typical experiment, the minicomputer (at a given command) turns on the stepping motor, driving the movable mirror of the interferometer to its starting position for a complete scan, at a rate of 300 steps per second. After waiting in that position for one second for the lock-in to integrate the signal, it reads in the voltage as measured by the NLS X2 digital voltmeter, stores the value of the voltage as a data point in memory, and then moves the mirror to the next position where the same process is repeated. In the waiting period between moving the mirror and reading in the data, the minicomputer can send the actual averaged spectrum to the display interface and plot it, ~~if~~ requested, through the plotter interface, on a chart recorder. The frequency of all these operations is checked using an internal real time clock of the computer that counts in hundredths of a second. At the end of a specified number of data points called the interferogram, the minicomputer does a fast fourier transform of these points. The program is set to accumulate the spectrum averaging the new spectrum with the old already recorded, using the appropriate weight for this last one. In many experiments, a magnetic tape recorder and reader of Digi Data Co. was used to record the interferograms before processing them, with the aim of doing a more detailed analysis after the experiment. A 700 ASR Texas Instrument Electronic Data Terminal allowed the operator to control the minicomputer when necessary. The interferogram was symmetric with respect to the zero optical path difference point, or central maximum. The numbers of points in it could be any number up to 512 per side. The main limitation was the size of the memory.

6. Noise

Figures for the signal to noise ratio varied with the experiment. In silicon, depending on the spectral band, this ratio varied from 2000-7000:1, with the best figures for the wider spectral bands. In germanium, where the work was done mostly at the fixed spectral band of 10 to 50 cm^{-1}, the figures varied from 1200-2500:1. In both silicon and germanium, it was found that a troublesome source of noise was due to fluctuations in isotropic emission by EHD in the far infrared, as observed by Vavilov, Zayats and Murzin (1969), although it was not so severe above 6 K in silicon. Several precautions were taken to minimize this noise. The first one was the stabilization of the laser power output, stabilizing the power supply and the flow of cooling water. A second precaution was a limitation of the aperture between the detector and the hole of the copper piece covering the sample, to allow only the relatively narrow infrared beam to pass, and minimize the capture of the isotropic emission by the EHD. Running the chopper at high frequencies usually helped in minimizing this noise. Another suspected source of noise was gas oscillations in the light pipe. To avoid it, small cuts were sawed in this pipe and, in general, no closed space was allowed inside the sample chamber.

In the magnetic measurements, it was observed that the operation of the magnet decreased the total value of the signal by a few percent and introduced an additional amount of noise. For magnetic experiments, typically we had 1200:1 signal to noise ratio. Because of this, all backgrounds were measured using the same magnetic field applied in the measurement of the spectrum with the excitons present.

In the operation of the interferometer, there are several sources of error that affect the computation of the spectrum. The most frequently encountered are thermal or electronic drift of the interferogram, stepping errors, and incorrect localization of the "central maximum" of the interferogram. The central maximum is the signal at zero optical path difference. The incorrect localization of the central maximum and the drift of the interferogram were taken care of by recording two-sided interferograms (Bell, 1972) and mathematically processing them. A two-sided interferogram consists of a scan where the optical path difference is varied between distances -L to +L from the central maximum. The effect of random stepping errors is minimized by repeatedly scanning the same interferogram and averaging all the corresponding spectra.

Two-sided interferograms have the disadvantage of introducing extra noise in the computed spectrum (Bell, 1972). This fact explains why the noise levels present in many of the spectra reported in this thesis are substantially larger than the smaller noise levels reported for the interferograms.

The resolution of a spectrum is inversely proportional to the total optical path length scanned. Hence, large resolutions imply long scanning times. As a consequence, the noise level in the signal poses a practical limit to the resolution that can be achieved. To reproduce the same noise level on a spectrum at higher resolution, a larger number of spectra had to be averaged. The number of scans necessary is equal to the square of the factor by which the resolution is improved times the old number of scans.

Some systematic sources of error, i.e., false peaks in the interferogram produced by some multiple internal reflection, equally affect the background and signal spectra. By dividing the average of a large number of these spectra, any false resultant information will tend to cancel.

CHAPTER III

THEORY OF INDIRECT EXCITONS

1. Introduction

An exciton is a bound state of an electron promoted to the conduction band and of a hole in the valence band. The mechanism for binding is provided by the electrostatic attraction between the positive hole and the negative electron.

In general the excitons can be classified into two types according to the strength of the Coulomb interaction. The Frenkel exciton is tightly bound, and the hole and the electron are separated by a radius of dimension comparable to the lattice constant. The other type is the Wannier exciton. In this case the electron and the hole are more loosely bound, with a radius many or several times as large as the lattice constant. The excitons in germanium or silicon comply very well with the physical characteristics of the Wannier exciton.

When the actual band structure of a material is considered, the lowest energy exciton is made up of $\vec{k}$ states for the electron near or at some local minimum of the conduction band. For the hole the $\vec{k}$ states are those near or at the maximum points of the valence band. If the minimum of the conduction band and the maximum of the valence band coincide in k space, the associated exciton is called a direct exciton. For some materials the minimum of the conduction band is not over the maximum of the valence band. In this case the exciton is called an indirect exciton. The creation of an indirect exciton requires the emission of a phonon, or absorption if the phonon is already thermally excited in the crystal, which provides the k vector difference of the two extremal points between the conduction and valence band. The decay of the indirect exciton requires the emission or absorption of the phonon.

Schematic pictures of the band structure of germanium and silicon are provided in figures 3-1 and 3-2. There it can be seen that there are two local minima for germanium and one for silicon in the conduction band. The valence bands in both materials have a single absolute maximum. In germanium both direct and indirect excitons can exist and have been observed. In silicon there can exist just indirect excitons associated with the first conduction band.

In this work only the spectra of indirect excitons in Ge and Si are presented and studied. The direct excitons in Ge have an observed ground state at energy 1.6 meV below the direct band edge (Johnson 1968). Hence the transitions between its quantum levels have by necessity energies smaller than this value, and slightly above 1 meV. These energies are just below the lower limit of the spectral region (1.5 meV) that could be reliably studied under the conditions for operating the lamellar interferometer. Also the intensity of this absorption is ruled by the relative population of the states in the two conduction band minima which is proportional to the Boltzmann factor $\exp(-\Delta E/kT)$, where ΔE is the energy difference between the two conduction band minima.

The exciton spectrum is usually compared with that of the hydrogen atom. This picture is quantitatively accurate only for materials with nondegenerate, isotropic and parabolic bands (Dresselhaus 1956). The description of the band structures for Ge and Si given below in section (2) of this chapter, makes it very clear that this is not the case for these two semiconductors.

Dresselhaus in the work mentioned above introduced an extension of the so called effective mass model of an exciton, to include the case of excitons in insulators or semiconductors in the general case of degenerate and non-isotropic bands. A method in which the exciton Hamiltonian is separated into various terms according to their symmetry was introduced by Lipari and Altarelli in a series of papers (Lipari and Altarelli 1976,1977) called for short LA from here on. This method is described in two works for acceptor states by Balderschi and Lipari (Baldereschi and Lipari 1973,1974). The method is very successful in explaining the exciton spectrum and provides a

Figure 3-1

Schematic energy band structure for germanium. Only the bands involved in this work are shown. The zero of energy is chosen at the valence band maximum. The two upper valence bands correspond to electron states with $\vec{J} = 3/2$. The split-off band of $\vec{J} = 1/2$ is .29 eV below the two other valence bands at the Γ point. The conduction band is .89 eV above the maximum of the valence band. E_g is the energy difference between the minimum point of the conduction band which is at the L point, and the maximum of the valence band. Group theory classification of the electron states in the bands is given at the center of the Brillouin zone and at the points at the boundaries of the zone. The generic nomenclature of these points and of the directions is displayed at the top of the diagram. In round parentheses is given the classification of the states when the spin of the electron is ignored.

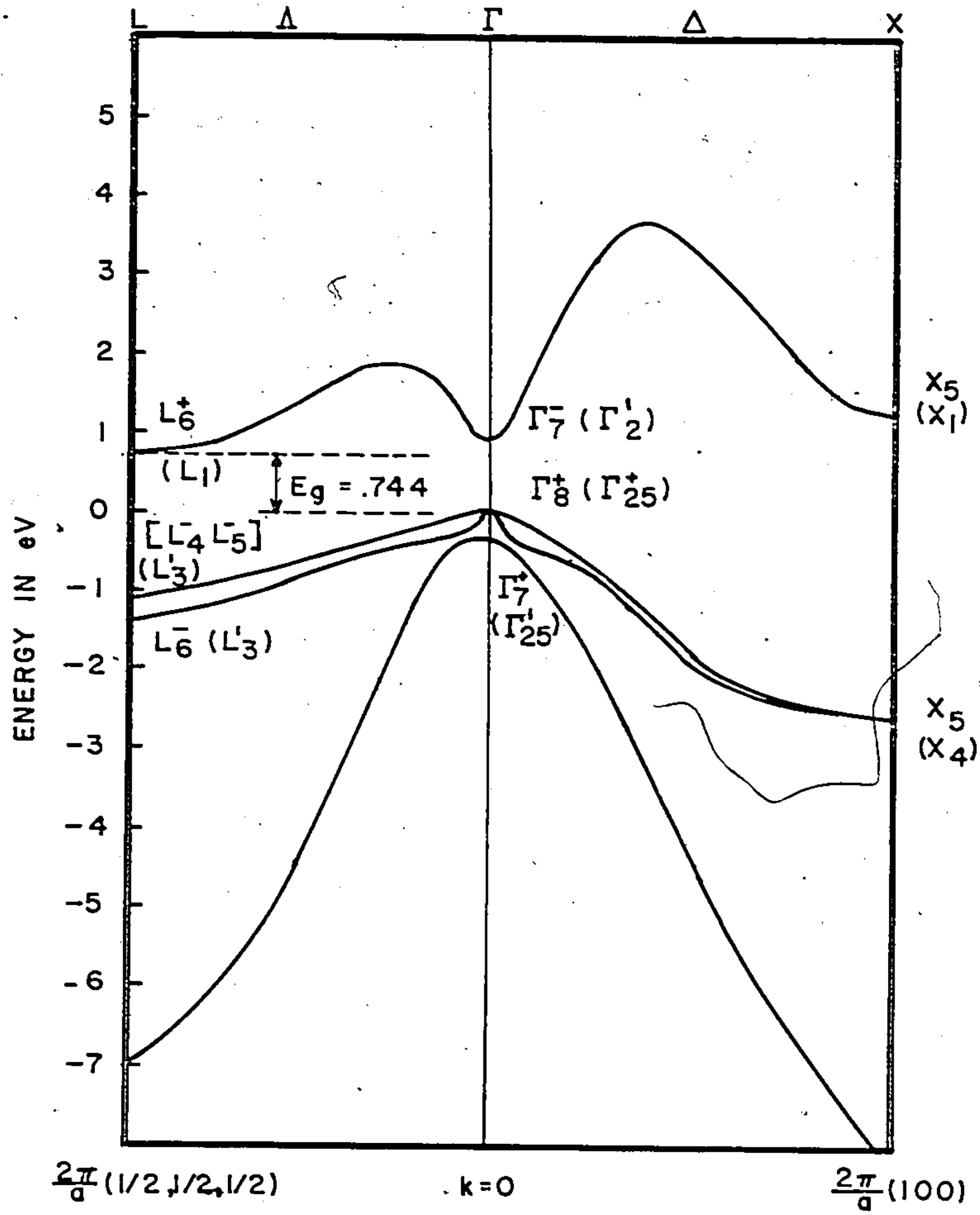
L
Λ
Γ
Δ
X
5
4
3
2
1
0
-1
-2
-3
-4
-5
-6
-7
ENERGY IN eV
L_6^+
(L_1)
$E_g = .744$
$[L_4^- L_5^-]$
(L_3')
$L_6^- \ (L_3')$
$\Gamma_7^- \ (\Gamma_2')$
$\Gamma_8^+ \ (\Gamma_{25}^+)$
Γ_7^+
(Γ_{25}')
X_5
(X_1)
X_5
(X_4)
$\frac{2\pi}{a}(1/2,1/2,1/2)$
k=0
$\frac{2\pi}{a}(100)$

Figure 3-2

Schematic energy band structure for silicon. Only the bands involved in this work are shown. The spin-orbit splitting of .044 eV of the valence band $\vec{J} = 1/2$ at $\vec{k} = 0$ is shown exaggerated, the same as the split in energy between the heavy and light hole bands, which are the upper and the one immediately down below. The zero of the energy is taken again at the maximum of the valence bands. The group theory classification of the electron states of the most important symmetry points are given in the diagram. In the round parentheses the classification for these states is also provided for the case when the spin of the electron is not considered.

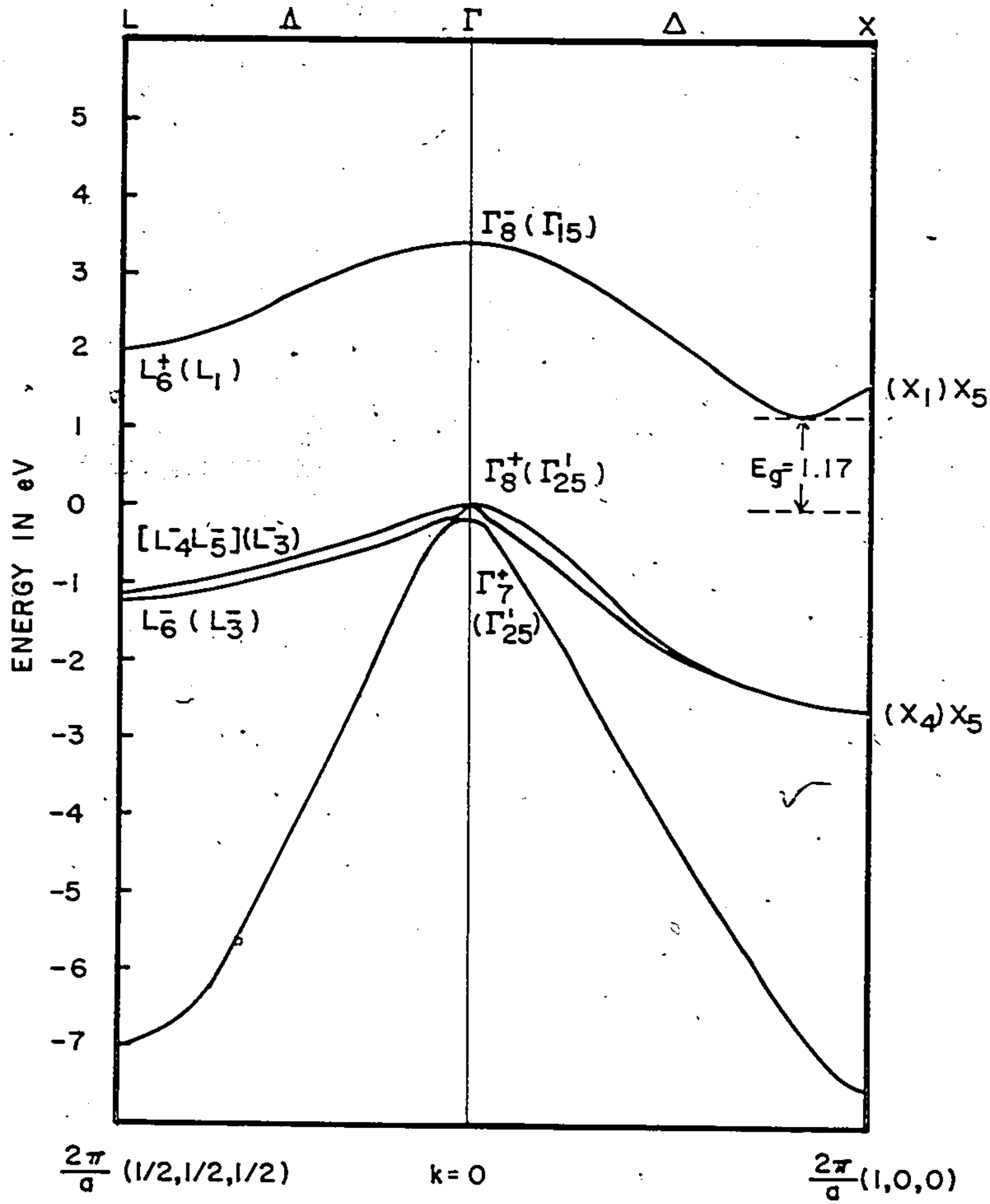
L
Λ
Γ
Δ
X
5
4
3
2
1
0
-1
-2
-3
-4
-5
-6
-7
ENERGY IN eV
$\Gamma_8^-(\Gamma_{15})$
$L_6^+(L_1)$
$(X_1)X_5$
$E_g = 1.17$
$\Gamma_8^+(\Gamma_{25}')$
$[L_4^- L_5^-](L_3^-)$
Γ_7^+
(Γ_{25}')
$L_6^-(L_3^-)$
$(X_4)X_5$
$\frac{2\pi}{a}(1/2,1/2,1/2)$
$k=0$
$\frac{2\pi}{a}(1,0,0)$

physical insight into the meaning and importance of the different terms of the exciton Hamiltonian. Hence this method is presented and discussed in section (3) of this chapter.

2. Band Structure

Germanium and silicon have the diamond structure which consists of a fcc Bravais lattice with a basis of two atoms at positions (0,0,0) and $(\frac{1}{4},\frac{1}{4},\frac{1}{4})$ per lattice point. The point group symmetry of the diamond structure is the cubic group O_h. In appendix B a brief description of this and other symmetry groups involved in this work is given. The band structure of Ge and Si can be seen in figs. 3-1 and 3-2, (Herman 1955, Cardona 1972), where only the relevant bands for this thesis are shown. The notation used to classify the symmetry states is that of G. F. Koster (1957). The figures show that in both germanium and silicon the valence band maximum occurs at the point $\vec{k}=0$. The hole state at this point has a fourfold degeneracy of symmetry classification Γ_8^+. This state is derived from $p_{3/2}$ states of the free atom. The four states correspond to $\vec{J}=3/2$ and $M_j = \pm 3/2, \pm 1/2$. Below this state there is another maximum of another valence band, of symmetry Γ_7^+. States at this maximum originate from $p_{1/2}$ states of the free atoms. The state is twofold degenerate with $M_j = \pm 1/2$. This state is split from the Γ_8^+ by the spin-orbit interaction, of the spin of the band forming electron, with the angular momentum of its atomic state. The values of the spin-orbit splittings, are given in table 3-1, as well as other values of the parameters involved in the description of the valence bands near the maximum. The Γ_8^+ level splits into two bands as $\vec{k}$ moves away from the center of the Brillouin zone. They are called the heavy and light hole bands. The heavy band corresponds to the upper valence band in fig.3-1 and 3-2, of larger radius of curvature. The light hole band is the other band and has smaller radius of curvature near $\vec{k}=\vec{0}$. These bands have constant energy surfaces that are distorted from spherical shape. The light hole band is very nearly spherical. The warping of the heavy hole band is more marked. For these bands the energy near $\vec{k}=\vec{0}$ is given by the expression (Dresselhaus, Kip, Kittel, Elliot 1954):

$$E(k) = Ak^2 \pm (B^2k^4 + C^2(k_1^2k_2^2 + k_2^2k_3^2 + k_3^2k_1^2))^{1/2} \quad . \quad (3\text{-}1)$$

The values of A,B,C are listed in table 3-1. The other valence band with the state Γ_7^+ at k=0, has very nearly spherical energy surfaces at values close to $\vec{k}=\vec{0}$. The energy of the k states of this band are given by:

$$E(k) = -\Delta + Ak^2 \qquad (3\text{-}2)$$

where Δ is the magnitude of spin-orbit splitting mentioned before and A is the same constant as for the two other bands. The mass of their holes will be called m_{3h}.

In germanium the minimum of the first conduction band is located at the L point, which is at the zone boundary in

Table 3-1

Energy band parameters for the hole states near $\vec{k} = \vec{0}$ and the electron states near the conduction band minima in germanium and silicon. The parameter Δ is written in meV, A, B and C are in units of $\hbar^2/2m$.

Holes	A	B	C	Δ	m_{hh}	$m_{\ell h}$
Ge	13.38	8.48	13.15	290	0.347	0.042
Si	4.28	0.75	4.85	44	0.523	0.154

Electrons	$m_{\ell e}$	m_{te}	m_{de}	m_{oe}
Ge	1.58	0.082	0.22	0.12
Si	9.9163	0.1905	0.3216	0.26

Note: The density of states mass m is defined as the geometric average of the longitudinal and transverse masses $m_{de}^3 = m_\ell m_t^2$. The optical mass is defined by the average $3m_{oe} = m_\ell + 2m_t$.

All band parameters quoted here are taken from Brinkman and Rice (1973).

the <111> directions. As a consequence of the symmetry of the diamond lattice, there are four equivalent energy minima in this case. The constant energy surfaces corresponding to values of $\vec{k}$ near the conduction band minima, are very elongated ellipsoids of revolution. They have their major axes along the <111> directions. The ratio of longitudinal m_{el} to transverse m_{et} masses, is around 20. Table 1 lists the experimental values of these masses, for both Ge and Si. The symmetry of these k states at the L point is L_1 when spin is ignored, or the extended representation L_6^+ of the double group when the spin of the electron is considered. In silicon the minimum of the conduction band is along the <100> line. The symmetry of a general point in this line is Δ_1 when spin is neglected and Δ_6 when spin is considered. The position of the minimum is quoted as $\frac{2\pi}{a}$ (0.86,0,0) by Kittel (1963). By the symmetry of the Brillouin zone, there are six equivalent energy minima for this conduction band. The constant energy surfaces are also ellipsoids with the major axes along <100> directions. The ratio of the longitudinal to the transverse mass is around 4.5.

3. Theory

In the effective mass model for the exciton it is assumed that the effect of the crystal structure is reflected in that the electron in the energy minimum of the conduction band can be described as a particle with negative charge and a mass determined by the local curvature of the band. A similar assumption is done for the hole assigning it positive charge. It is furthermore assumed that the electron and the hole interact according to the Coulomb law, which is modified by the static dielectric constant of the medium. Then the Hamiltonian for the relative motion of the electron and hole can be expressed mathematically as follows:

$$H_{ex} = H_e(\vec{p}_e) - H_h(\vec{p}_h) - \frac{e^2}{\varepsilon_0 |\vec{r}_e - \vec{r}_h|} \qquad (3\text{-}3)$$

where the subscripts e and h refer to the electron and hole respectively. In this equation and from here on small p represents the momentum conjugate to the respective coordinate. H_e is the kinetic energy of the electron near the conduction band minimum and H_h is the Kohn-Luttinger Hamiltonian which describes the hole kinetic energy near $\vec{k}=\vec{0}$ (Luttinger and Kohn 1955) and (Luttinger 1956).

The constant energy surfaces for the electrons are ellipsoids with cylindrical symmetry and hence the electron Hamiltonian is:

$$H_e = \frac{1}{2m_{et}}(p_1^2 + p_2^2) + \frac{p_3^2}{2m_{el}} \qquad (3\text{-}4)$$

where m_{et}, m_{el} are the longitudinal and transversal masses as listed in table 1, and p_1, p_2, p_3 are the electron momentum components along the principal axes of the ellipsoid. The subscript 3 represents the major axis. For germanium this system of coordinates is different from the crystal cubic axes x,y,z also used for the hole Hamiltonian.

The Kohn-Luttinger Hamiltonian for the hole in the valence band is:

$$-H_h(\vec{p}_h) = (\gamma_1 + \frac{5}{2}\gamma_2)\frac{p^2}{2m_e} - \frac{\gamma_2}{m_e}\sum_i p_i^2 J_i^2$$
$$- \frac{2\gamma_3}{m_e}(\{p_x p_y\}\{J_x J_y\} + \{p_y p_z\}\{J_y J_z\} + \{p_z p_x\}\{J_z J_x\}) \quad (3-5)$$

where $\{ab\} = \frac{1}{2}(ab+ba)$, γ_1, γ_2, γ_3 are parameters introduced by Luttinger (1956) and are listed in table (3-2), J is the angular momentum corresponding to spin 3/2. This Hamiltonian is valid in the limit of strong spin-orbit coupling i.e. when the valence band splitting is much larger than the exciton binding energy.

An exciton of wave vector $\vec{k}$ is formed from electron and hole wave packets with wave vectors $\vec{k}_e$ and $\vec{k}_h$ respectively, such that:

$$\vec{k} = \vec{k}_e - \vec{k}_h \,. \quad (3-6)$$

The analysis of the Hamiltonian will be restricted to exciton states with $\vec{k}_0 = \vec{k}_e - \vec{k}_h$, i.e. to states with the electron and the hole at the extremum points of the bands. In this case (Dresselhaus 1956) the exciton Hamiltonian can be written in terms of the relative momentum $\vec{p}$ conjugate to the relative coordinate $\vec{r}' = \vec{r}_e - \vec{r}_h$ in the following way:

$$H_{ex} = H_e(\vec{p}) - H_h(\vec{p}) + \frac{e^2}{r} . \qquad (3\text{-}7)$$

The exciton wavefunction can be written as:

$$\psi(\vec{r}_e,\vec{r}_h) = \sum_i F^i_{ex}(\vec{r}_e-\vec{r}_h)\phi^i_h(r_h)\phi_e(\vec{r}_e) \qquad (3\text{-}8)$$

where ϕ_e and ϕ_h are the Bloch functions for the electron and the hole, F^i_{ex} is the envelope function which describes the relative electron-hole motion and is an eigenfunction of Hamiltonian (3-7), and i runs over the four degenerate valence band states.

Once the full exciton Hamiltonian is written in terms of the momentum p conjugate to the relative coordinate $\vec{r} = \vec{r}_e - \vec{r}_h$, it can be separated in terms of different symmetry. To do this Lipari and Balderschi (1973), introduced the following cartesian, traceless, symmetric tensors:

$$P_{ik} = 3p_ip_k - \delta_{ik}p^2 \qquad (3\text{-}9)$$

$$J_{ik} = \frac{3}{2}(J_iJ_k + J_kJ_i) - \delta_{ik}J^2 . \qquad (3\text{-}10)$$

In terms of these tensors the Hamiltonian can be written as follows:

$$H = \left(\frac{\gamma_1}{m_0} + \frac{1}{\mu_{0e}}\right)\frac{p^2}{2} - \frac{e^2}{\varepsilon_0 r} - \frac{1}{2\mu_{1e}} P_{33} - \frac{1}{9m_0}[\gamma_3 - (\gamma_3 - \gamma_2)\delta_{ik}]P_{ik}J_{ik} \tag{3-11}$$

where repeated indices are to be summed as in the Einstein convention. μ_{0e} and μ_{1e} are defined as

$$\frac{1}{\mu_{0e}} = \frac{1}{3}\left(\frac{2}{m_{et}} + \frac{1}{m_{el}}\right) \tag{3-12}$$

$$\frac{1}{\mu_{1e}} = \frac{1}{3}\left(\frac{1}{m_{et}} - \frac{1}{m_{el}}\right) \tag{3.13}$$

μ_{0e} can be thought of as the "spherical mass" of the electron, and μ_{1e} represents the "deviation of the sphericity" mass. The Cartesian tensors can be expressed in terms of irreducible spherical tensors of the second rank $P_q^{(2)}$, $J_q^{(2)}$, with $q = -2, -1, 0, 1, 2$. Spherical tensors of rank one, which are formed from antisymmetrical combinations of Cartesian tensor components, are absent because of the symmetry of the Cartesian tensors. The two spherical tensors of rank zero P_0^0, J_0^0, are also absent because they are equal to the trace of the Cartesian components and these by definition have vanishing trace. Using the definitions of the scalar and vector products of irreducible tensors (A. R. Edmonds 1974), the Hamiltonian for the exciton can be written as:

$$H_{100} = \left(\frac{1}{\hbar^2} p^2 - \frac{2}{r}\right) - \frac{\mu}{9\hbar^2}\left(P^{(2)} \cdot J^{(2)}\right) - \sqrt{\frac{2}{3}}\,\mu_{01} P_0^{(2)} \tag{3-14}$$

$$+ \frac{\delta}{9\hbar^2}\left\{[P^{(2)} \times J^{(2)}]^4_{-4} + \frac{\sqrt{70}}{5}[P^{(2)} \times J^{(2)}]^4_0 + [P^{(2)} \times J^{(2)}]^4_{-4}\right\}.$$

Here $P^{(2)}, J^{(2)}$ represent spherical tensors of second rank, p the linear relative momentum. The Hamiltonian has been divided by the effective Bohr radius a_0 and the exciton Rydberg R_0. These two quantities and μ_0, μ, μ_1, δ are defined as follows:

$$R_0 = \frac{e^4}{2\hbar^2}\frac{\mu_0}{\varepsilon_0^2} \tag{3-15}$$

$$a_0 = \frac{\hbar^2 \varepsilon_0}{\mu_0 e^2} \tag{3-16}$$

$$\frac{1}{\mu_0} = \frac{1}{\mu_{0e}} + \gamma_1 \tag{3-17}$$

$$\mu = \frac{1}{5}(6\gamma_3 + 4\gamma_2)\mu_0 \tag{3-18}$$

$$\delta = (\gamma_3 - \gamma_2)\mu_0 \tag{3-19}$$

$$\mu_{01} = \frac{\mu_0}{\mu_{ie}}. \tag{3-20}$$

The subscript 100 in H_{100} indicates that ellipsoidal constant energy surfaces for the electron are along the <100> direction. The values of all the parameters in equations (3-15) to (3-20) for both germanium and silicon are listed in table 3-2. The

Hamiltonian H_{100} applies for the excitons in silicon. Inspecting the different terms of the Hamiltonian (3-14), it is seen that the first two terms are scalar operators and the third one is the scalar product of two spherical tensors. Then these three terms are invariant under any rotation i.e. they have spherical symmetry. The fifth term is a sum of components of a tensor of rank four. These components transform like the Y_m^4 spherical harmonics and hence they represent the components of a cubic potential (M.T. Hutchings, 1964), expressed in spherical tensors. The fourth term $P_0^{(2)}$ is equal to:

$$P_0^{(2)} = (2p_z^2 - p_x^2 - p_y^2) \tag{3-21}$$

and it has d-like symmetry ($D_{\infty h}$ symmetry), which is the lowest symmetry for this Hamiltonian. This term comes from the non-sphericity of the constant energy surfaces for the electron and introduces symmetry axes in reciprocal space along the <111> direction for Ge and along the <100> for Si. The cubic symmetry is reduced to that of the group $L(C_{3v})$ for germanium and to the group $\Delta(C_v)$ for silicon. In this way this term introduces additional splittings in the energy levels of a system for which the constant energy surfaces of the electron are spherical, such as the direct exciton in germanium.

For the indirect exciton in germanium the ellipsoidal axes of the electron Hamiltonian do not coincide with the hole Hamilton axes. Then it is necessary to rotate either the electron or the hole Hamiltonian, to write the whole exciton Hamil-

Table 3-2

List of parameters used in the exciton Hamiltonian. R_0 is in meV. a_0 is in angstroms and $\gamma_1, \gamma_2, \gamma_3$ are in units of $\hbar^2/2m$ $\mu_0, \mu, \mu_a, \delta$ are dimensionless quantities.

	γ_1	γ_2	γ_3	μ_0	μ	μ_{0_1}	δ	R_0	a_0
Ge	13.38	4.24	5.69	0.046	0.469	0.178	0.067	12.90	49
Si	4.28	0.38	1.44	0.123	0.252	0.171	0.130	2.65	176.7

Expressions of the Luttinger parameters in terms of the Dresselhaus-Kittel parameters are given as $\gamma_1 = A$, $\gamma_2 = B/2$ and $\gamma_3 = \frac{1}{2\sqrt{3}} \ (3B^2 + C^2)^{1/2}$ by (N.O. Lipari and A. Baldereschi 1971).

tonian, in a common set of coordinates. LA found that it is better to rotate the hole Hamiltonian axes to express them in the ellipsoidal axes of the electron. The reason for this is that the final expression for the exciton Hamiltonian has simpler symmetry in this set of axes. The rotation has to be carried out explicitly just for the cubic terms. This is done using the rotation matrices in the J=4 representation and the fact that the Euler angles of rotation between the <100> and the <111> directions are $\alpha = \frac{3}{2}\pi$, $\beta = \cos^{-1}(1/\sqrt{3})$, and $\gamma = \frac{3}{4}\pi$. The new rotated spherical tensor operator $(T')^4_m$ is expressed in terms of the old operators T^4_m according to:

$$(T')^4_m = \sum_{m'=-4}^{4} T^4_{m'} D^4_{m'm}(\alpha,\beta,\gamma) \quad . \tag{3-22}$$

The expressions for the rotation matrix elements $D^4_{m'm}$ are given by Edmonds (1974).

The result of the rotation is the exciton Hamiltonian for which the conduction band minima are along the <111> direactions. It is given by (Lipari and Altarelli 1977)

$$\begin{aligned} H_{111} = {} & \frac{1}{\hbar^2} P^2 - \frac{2}{r} - \left(\frac{2}{3}\right)^{1/2} \mu_{01} P^{(2)}_0 - \frac{1}{9\hbar^2}\mu(P^{(2)}\cdot J^{(2)}) \\ & + \frac{1}{9\hbar^2}\delta\{\frac{4}{3}\, i[P^{(2)}\times J^{(2)}]^4_{-3} - \frac{2\sqrt{70}}{15}[P^{(2)}\times J^{(2)}]^4_0 \\ & + \frac{4}{3}\, i[P^{(2)}\times J^{(2)}]^4_3\} \quad . \end{aligned} \tag{3-23}$$

This exciton Hamiltonian is very similar to the Hamiltonian (3-14). The only difference lies in the cubic term which has different components and coefficients. But the symmetry characterization of the five terms remains the same. Here it is important to analyze the contribution to the spectrum from the terms of different symmetry. The reasons for this are essentially two: first, the addition of a term of lower symmetry will split some of the essential degeneracies of the energy levels produced by terms of higher symmetry; second it is possible to make a qualitative estimate of the relative contribution of each term to the final spectrum. To do this analysis, the Hamiltonians (3-14) and (3-23) are written in the following symbolic way:

$$H_{ex} = H_{sph} + H_{cubic} + H_d \tag{3-24}$$

where the subscripts label the symmetry of the different terms of the Hamiltonian.

The simplest Hamiltonian that gives a lot of information about the physics of the problem is the spherical Hamiltonian given by:

$$H_{sph} = \left(\frac{1}{\hbar^2} p^2 - \frac{2}{r}\right) - \frac{\mu}{9\hbar^2} \left(P^{(2)} \cdot J^{(2)}\right) . \tag{3-25}$$

The first two terms inside the bracket represent a hydrogenic system with the well known spectrum, in Rydberg units,

$$E(\mu = 0) = -\frac{1}{n^2} \qquad (3\text{-}26)$$

where n is the usual atomic principal quantum number. It can be used to classify the eigenstates, together with the different allowable values of the original angular momentum L, and its projection along some z axis, L_z.

For $\mu \neq 0$ it is necessary to consider the spin $\vec{J} = 3/2$ of the hole and the term,

$$\frac{\mu}{9\hbar^2} \left(P^{(2)} \cdot J^{(2)}\right) . \qquad (3\text{-}27)$$

In this case the total spherical Hamiltonian (3-25) can be thought of as describing the hydrogenic atom perturbed by this term, which is a kind of "spin-orbit" interaction which couples the spin $\vec{J} = 3/2$ of the hole with $\vec{L}$, the orbital angular momentum of the exciton. In this case the states can be classified following the L-S coupling scheme used for atomic systems. Then the states are $|n,L,J,F,F_z\rangle$, where $\vec{F} = \vec{L} + \vec{J}$ is the total angular momentum.

In this case the hydrogenic nS states can give rise only to $nS_{3/2}$ states, and the nP states split into $nP_{1/2}$, $nP_{3/2}$ and $nP_{5/2}$. Figure 3-3 shows a diagram of the successive splittings of the hydrogenic states produced by the addition of the different terms until the full exciton Hamiltonian is obtained. In contrast to the hydrogen atom this spin orbit is not zero for the S states and their energy is also shifted with respect to the hydrogenic spectrum. The reason for this is that the spherical tensor $P^{(2)}$ is not directly proportional to the angular momentum as in the atomic case. This is one of the contributing factors that makes the ionization energy of the exciton higher than the value predicted for the Rydberg in equation (3-15).

A crude estimate of the relative magnitude of the "spin-orbit" coupling term for the indirect exciton in Ge and Si as compared with the atomic spin-orbit coupling is obtained by dividing the coefficient $\mu/9 \approx .1\ \mu$ for exciton coupling by the square of the fine structure constant $\alpha = 1/137$ (Baym 1974). Using the values of table 2, this gives that the strength of the coupling is 860 times stronger for the exciton in germanium, and 470 times higher for the exciton in silicon, than for the atomic case. In table 3-3 the expected values for the energy shift of the hydrogenic states 1S, 2S and 2P produced by this spin-orbit coupling are given in the spherical approximation (A. Baldereschi and N. O. Lipari 1973).

The addition of the cubic term to the spherical Hamiltonian lowers the symmetry to that of the point group O_h. The states of a system described by the spherical plus the cubic potential are further split. The eigenstates in this case can be classified according to the cubic group representation, and the splittings also can be worked out immediately (A. Balderachi and N. O. Lipari 1974). Their results are that the $S^{3/2}$ (Γ_8^+) states shift in energy but do not split. The same happens for

Figure 3-3

Qualitative splitting of the energy levels 1S, 2P of a system described by the different Hamiltonians formed by the successive addition of each of the terms of a given symmetry of the exciton Hamiltonian (3-24) to the hydrogen Hamiltonian. R_0 is the Rydberg defined in equation (3-15). Δ_0 is the magnitude of the ground state splitting. Case a) shows the hydrogen spectrum. The 2P level is at 0.25 R_0 below the ionization edge. Case b) represents the system for which the spherical Hamiltonian (3-25) applies, i.e. when the spin-orbit coupling (3-27) is added. Case c) represents a system in which the cubic symmetry of the hole has to be taken into consideration. Finally d) represents the spectrum of an exciton with the levels classified as if the conduction band minima were along the Δ lines.

The separation between the levels is arbitrary, as is the ordering of the levels. Only the ground state has been drawn so as to reflect the sign of the new term added in each case.

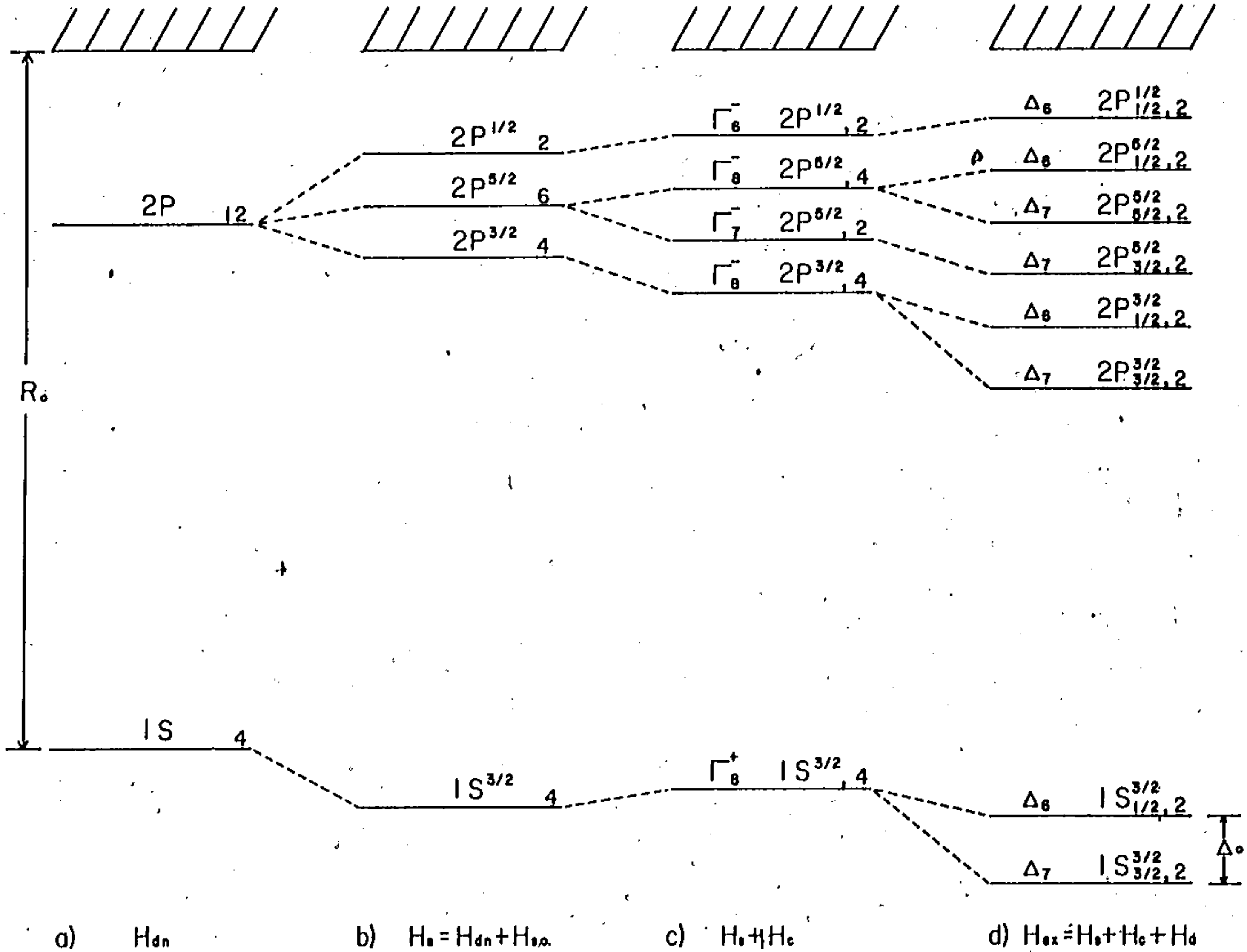

2P 12
1S 4
R_o
2P$^{1/2}$ 2
2P$^{5/2}$ 6
2P$^{3/2}$ 4
1S$^{3/2}$ 4
Γ_6^- 2P$^{1/2}$, 2
Γ_8^- 2P$^{5/2}$, 4
Γ_7^- 2P$^{5/2}$, 2
Γ_8^- 2P$^{3/2}$, 4
Γ_8^+ 1S$^{3/2}$, 4
Δ_6 2P$^{1/2}_{1/2}$, 2
Δ_6 2P$^{5/2}_{1/2}$, 2
Δ_7 2P$^{5/2}_{5/2}$, 2
Δ_7 2P$^{5/2}_{3/2}$, 2
Δ_6 2P$^{3/2}_{1/2}$, 2
Δ_7 2P$^{3/2}_{3/2}$, 2
Δ_6 1S$^{3/2}_{1/2}$, 2
Δ_7 1S$^{3/2}_{3/2}$, 2
Δ_o
a) H_{dn}
b) $H_s = H_{dn} + H_{s.o.}$
c) $H_s + H_c$
d) $H_{ex} = H_s + H_c + H_d$

Table 3-3

Spin-orbit splitting of the 2P levels, and energy shift of the 1S level for the exciton in the spherical approximation, defined by the Hamiltonian (3-25)

Ge	Level	Energies in Rydbergs	in meV.	Energy shift in Rydbergs	Energy shift in meV	in kOe
	$1S^{3/2}$	1.25	3.31	0.25	0.66	114.0
	$2P^{3/2}$	0.46	1.22	0.21	0.56	96.3
	$2P^{5/2}$	0.30	0.80	0.05	0.14	23.8
	$2P^{1/2}$	0.18	0.48	-0.07	-0.18	31.5
Si						
	$1S^{3/2}$	1.13	14.58	0.13	1.68	289.7
	$2P^{3/2}$	0.39	5.03	0.14	1.81	312.0
	$2P^{5/2}$	0.26	3.35	0.01	0.13	22.3
	$2P^{1/2}$	0.19	2.45	-0.06	0.77	133.7

Note: The energy shift is measured against the expected value of the level in the hydrogenic spectrum. To get the energy in Kilo-Oersteds the value of the Bohr magneton was used $\mu_B = 5.788\times10^{-6}$ meV/ Oe.

$P^{1/2}(\Gamma_6^-)$ and $P^{3/2}(\Gamma_8^-)$ states, but $P^{5/2}$ splits into a two fold degenerate level $P^{5/2}$ (Γ_7^-) and a fourfold degenerate $P^{5/2}(\Gamma_8^-)$ state. The values of the δ parameters are smaller than those for μ and are listed in table 3-2.

The last term of the Hamiltonian (3-24) $H_d = (2/3)^{1/2}\mu_{01}P_0^{(2)}$ comes from the anisotropy of the conduction band. This term splits the levels of an F term into separate levels of different absolute value of F_z. Due to Kramers theorem, which says that for crystals with inversion symmetry the minimum degeneracy of levels of half integer spin is two, (in the absence of a magnetic field), then the states having F_z of opposite sign are degenerate. Then in this case the $S^{3/2}$ states split into two levels $S^{3/2}_{1/2}$, $S^{3/2}_{3/2}$. The possible P states are six and they are $P^{1/2}_{1/2}$, $P^{3/2}_{1/2}$, $P^{3/2}_{3/2}$, $P^{5/2}_{1/2}$, $P^{5/2}_{3/2}$, $P^{5/2}_{5/2}$. The effect of this conduction anisotropy combines with the cubic anisotropy of the valence band and both effects produce a large appreciable splitting of the exciton levels.

The actual eigenstates of the full exciton Hamiltonian are no longer pure $|n,L,J,F,F_z\rangle$ states but a linear combination of them, with coefficients that are functions of the radial coordinate. The actual envelope wavefunctions, eigenstates of the full Hamiltonian (3-14), (3-23) can be written as:

$$F(\vec{r}) = \sum_i f^i(\vec{r})\,|L^i,J,F^i,F_z^i\rangle \qquad (3\text{-}28)$$

where the sum is to be performed over the different possible values of $\vec{F}$ for a given L, and in principle all the different components F_z for a given value of F. Because the exciton Hamiltonian is invariant under time reversal in zero magnetic field, parity is a good quantum number for its eigenstates. Hence the expansion (3-28) has to be done including just states of the same parity i.e. it runs only over even or odd values of L. Also because the cubic terms of the Hamiltonian couples only terms that have $F_z = 0, \pm 4$, the expansion (3-28) is further restricted to states with F_z values that obey this restriction for silicon. For Ge the expansion is restricted to terms that differ in $F_z = 0, \pm 3$. Using variational techniques Lipari and Altareli (1977) obtained the energy eigenvalues of the different 1S, 2S and 2P states of the exciton. Their values are listed in tables 3-5 and 3-6 and they are compared with the experimental values for germanium and silicon in the two following chapters.

From their results, the values of the ground state splitting between the two states $1S^{3/2}_{1/2}$ and $1S^{3/2}_{3/2}$ are given as $\Delta_0 = 1.01$ meV for germanium and $\Delta_0 = 0.46$ meV for silicon. To get better agreement with experiment for the energy states in silicon, they added a contribution of $\Delta = 0.3$ meV to all energy states produced by the split-off band $\vec{J} = 1/2$, which is just 44 meV below the $\vec{J} = 3/2$ bands. This value was calculated by perturbation theory (A. Baldereschi and H. O. Lipari 1973).

The exciton states can be classified according to the group theory representations of the symmetry group for the whole exciton Hamiltonian. In the process of classifying the states, their final degeneracy is also obtained. The group theory classification scheme can be compared with the one in terms of the states $|nL,J,F,F_z\rangle$ or $nL^F_{F_z}$, using the rotation properaties of the states $L^F_{F_z}$ under the different operations that compose the exciton symmetry group. Although the actual exciton states are not pure 1S or 2P states, the largest or the two larger contributing states in the expansion (3-28) for the wavefunction are used for labelling the state.

The symmetry of the exciton (3-8) is determined by the direct product of the representations for the envelope, hole, and electron wavefunctions.

As was mentioned in section (2) of this chapter, or from figure 3-1, the symmetry of the hole state at $\vec{k} = \vec{0}$ is Γ_8^+. The conduction bands have symmetries Δ for silicon and L for germanium when the spin of the electron is neglected. The S states of the envelope function are spherically symmetric and so they do not have to be considered in the direct product. The envelope P states have Γ_{15} symmetry of the point group O_h. Then the symmetry products of the exciton wavefunctions are:

For S states:

<u>Silicon</u> $\qquad \Gamma_8^+ \otimes \Delta_1 = (\Delta_6 + \Delta_7) \otimes \Delta_1 = \Delta_6 + \Delta_7$

<u>Germanium</u> $\Gamma_8^+ \otimes L_1 = (L_4^+ + L_5^+ + L_6^+) \otimes L_1 = L_4^+ + L_5^+ + L_6^+$

For P states:

<u>Silicon</u> $(\Gamma_{15} \otimes \Gamma_8^+) \otimes \Delta_1 = 3\Delta_6 + 3\Delta_7$

<u>Germanium</u> $(\Gamma_{15} \otimes \Gamma_8^+) \otimes L_1 = 2(L_4^- + L_5^-) + 4L_6^-$

where all products have been evaluated under the compatibility tables of appendix B. The numeric factors in front of some of the representations indicate how many independent times a representation was obtained when doing the product. Now the Δ_6 and Δ_7 representations are two-dimensional, so they represent states with a remaining two-fold degeneracy. The states $L_6^{\pm}$ are also bidimensional, but the representations $L_4^{\pm}$, $L_5^{\pm}$ are one dimensional. However because the electron Hamiltonian is also invariant under time reversal, and since $L_4^{\pm}$ and $L_5^{\pm}$ are complex conjugates of each other, they are degenerate, because they represent a particle of half spin (Bassani and Parravicini 1975). In table 3-4 the results of the classification for the exciton levels are listed.

The allowed optical transitions between the 1S to 2P states can be obtained also using group theory. The electric dipole operator can be written as a spherical tensor of rank one (Baym 1974). Hence the dipole operator transforms in the same way as the spherical harmonics Y_{lm} under the symmetry operations of the group O_h. The Y_{lm} spherical harmonics form a basis for

Table 3-4

Classification of indirect exciton states in germanium and silicon in terms of representations of their symmetry group. The correspondence with the $|L\ J\ F\ F_z\rangle$ representation is given in the last column

Atomic type	symmetry group classification	L,F,F_z
Si:		
1S	Δ_6	$\|0,\frac{3}{2},\frac{1}{2}\rangle$
	Δ_7	$\|0,\frac{3}{2},\frac{3}{2}\rangle$
2P	$3\Delta_6$	$\|1,\frac{1}{2},\frac{1}{2}\rangle, \|1,\frac{3}{2},\frac{1}{2}\rangle$
		$\|1,\frac{5}{2},\frac{1}{2}\rangle$
	$3\Delta_7$	$\|1,\frac{3}{2},\frac{3}{2}\rangle, \|1,\frac{5}{2},\frac{3}{2}\rangle$
		$\|1,\frac{5}{2},-\frac{5}{2}\rangle$
Ge		
1S	$L_4^+ + L_6^+$	$\|0,\frac{3}{2},\frac{3}{2}\rangle$
	L_6^+	$\|0,\frac{3}{2},\frac{1}{2}\rangle$
2P	$4L_6^-$	$\|1,\frac{1}{2},\frac{1}{2}\rangle, \|1,\frac{3}{2},\frac{1}{2}\rangle$
		$\|1,\frac{5}{2},\frac{1}{2}\rangle, \|1,\frac{5}{2},-\frac{5}{2}\rangle$
	$2(L_4^- + L_5^-)$	$\|1,\frac{3}{2},\frac{3}{2}\rangle, \|1,\frac{5}{2},\frac{3}{2}\rangle$

the D^{-1} representation of the rotation-inversion group. This representation is compatible with the Γ_{15} representation of the O_h group. Hence the electric dipole operator transforms as the Γ_{15} representation under the operations of the cubic group. Using the compatibility tables in appendix B between representations of the group O_h and the L and Δ symmetry groups, the dipole operator transforms according to the representations $L_1' + L_3'$ under the group L, and $\Delta_1 + \Delta_5$ under the group Δ. From the compatibility tables it can then be shown that all optical transitions between the two groups of states 1S, 2P are allowed, for both the excitons in germanium and silicon.

Table 3-5

Theoretical values for the energies of transitions between 1S to 2P states for indirect excitons in germanium (Lipari, Altarelli and Tosatti 1977).

transition energy (meV) From $1S^{3/2}_{1/2}$	From $1S^{3/2}_{3/2}$	Final state
1.27	2.29	$(2P^{3/2}_{3/2}, 2P^{5/2}_{3/2})$
2.05	3.07	$2P^{3/2}_{1/2}$
2.30	3.33	$(2P^{5/2}_{1/2}, 2P^{5/2}_{-5/2})$
2.40	3.42	$(2P^{5/2}_{-5/2}, 2P^{3/2}_{3/2})$
2.41	3.43	$(2P^{5/2}_{-5/2}, 2P^{5/2}_{1/2})$
2.72	3.74	$2P^{1/2}_{1/2}$

The calculated ground state energies are 4.20 meV for the $1S^{3/2}_{3/2}$ state and 3.18 for the $1S^{3/2}_{1/2}$ state. The ground state splitting is 1.02 meV. The most important contributing terms have been written first for the 2P states.

Table 3-6

Theoretical values of the energies for transitions between 1S to 2P for indirect excitons in silicon (Timusk, Navarro, Lipari and Altarelli 1978).

Transition energy (meV) From $1S^{3/2}_{1/2}$	From $1S^{3/2}_{3/2}$	Final state
9.56	10.01	$2P^{3/2}_{3/2}$
9.92	10.37	$(2P^{3/2}_{1/2}, 2P^{5/2}_{1/2})$
10.93	11.38	$(2P^{3/2}_{1/2}, 2P^{5/2}_{1/2})$
11.01	11.47	$2P^{5/2}_{5/2}$
12.04	11.59	$2P^{5/2}_{3/2}$
12.31	11.85	$2P^{1/2}_{1/2}$

The ground state splitting energy is 0.46 meV.

CHAPTER IV

EXCITONS IN GERMANIUM

1. Introduction

In this chapter the far infrared absorption spectrum of the indirect exciton in germanium (sec. 2) is studied. The observed transitions are compared with the theoretical model proposed by LA, discussed in the previous chapter. As a further test of the theoretical understanding of this spectrum, its response to an externally applied magnetic field was measured (sec. 3). To analyze the observed behaviour of the transitions with the field applied, a simplified magnetic Hamiltonian is introduced (sec. 4). Finally in the last section, as a conclusion to the analysis of the experimental facts presented in this chapter, a scheme for the 1S and 2P states for the indirect excitons in Ge is presented.

2. Experimental Results and Discussion

The measured exciton absorption spectra in germanium are presented in figures 4-1, 4-2 and 4-3. The quantity plotted is $\alpha d = -\ell n\ (I_0/I)$, the absorption constant times the depth of the absorption region, versus the energy of the photons absorbed.

Figure 4-1 shows the absorption spectrum at 3 K. A series of lines of varying intensity can be observed in the region between 2 to 3.5 meV. The positions of their peaks are 2.15, 2.25, 2.43, 2.88, 3.15, 3.35 and 3.44 meV with an accuracy in their positions of 0.01 meV. The peak at 2.15 meV is just barely larger than the noise level of the baseline. There is also observable an absorption shoulder next to the peak at 3.15 meV whose maximum centers around 3.06 meV. Also the line that peaks at 3.35 meV is not completely resolved from the transition peaking at 3.44 meV.

Figure 4-2 shows the exciton absorption spectrum at 4.2 K and in a wider spectral region. In the region from 2 to 3.6 meV a series of discrete transition lines can again be seen. The lines at 2.15, 2.43, 3.14, 3.35 and 3.44 meV are again present. There are several changes to be noted. First the line that appeared as the broad shoulder at 3.05 meV at 3 K has increased almost two times in intensity and peaks at 3.03 meV. Also the line at 2.88 meV has grown in intensity and is barely visible as part of a shoulder on the low energy side of the peak at 3.03 meV. Second, the peak whose apparent position was 2.25 meV at 3 K is no longer visible, and instead a shoulder that peaks at 2.35 meV is seen at the low energy side of the peak at 2.43 meV. At the other side of this peak a new shoulder is visible that corresponds to a line with energy 2.55±0.02 meV. In addition to these features, there is below 2 meV some other structure visible. There are two possible peaks at 1.40 and 1.06 meV, but their intensity is just barely higher

FIGURE 4-1

Exciton absorption spectrum in germanium at 3°K. In this figure the spectral region is restricted to show only the discrete transitions between the internal exciton states. The structure above 3.5 meV is the onset of a continuous absorption that extends to energies above 7 meV. The spectral resolution is 0.06 meV.

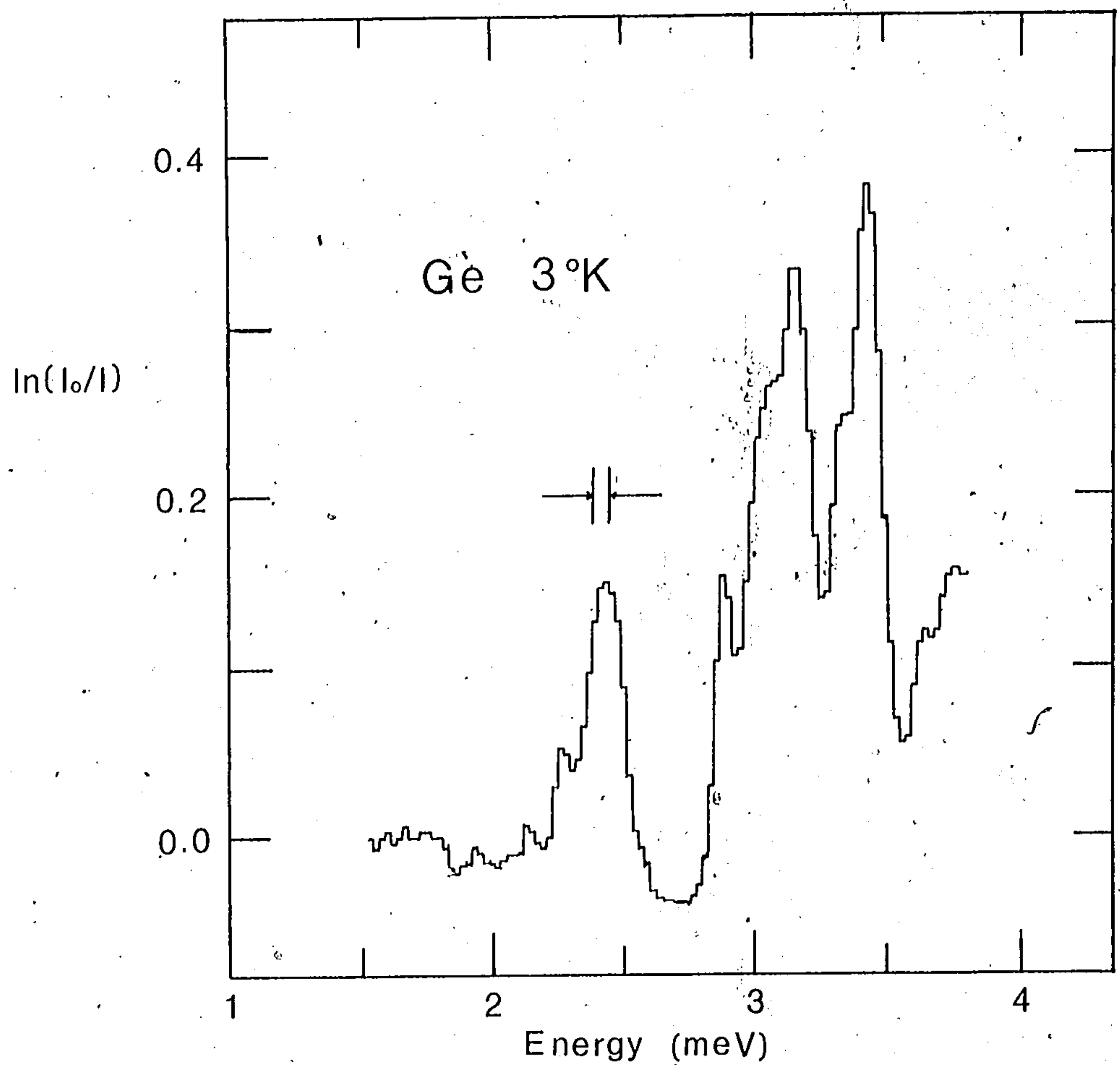
Ge 3°K
ln(I₀/I)
0.4
0.2
0.0
1
2
3
4
Energy (meV)

FIGURE 4-2

The absorption spectrum of excitons in germanium at 4.2°K. In addition to the discrete transitions a continuous absorption tail for energies above 3.5 meV is clearly visible. The structure in this tail is due to noise. The resolution is 0.06 meV.

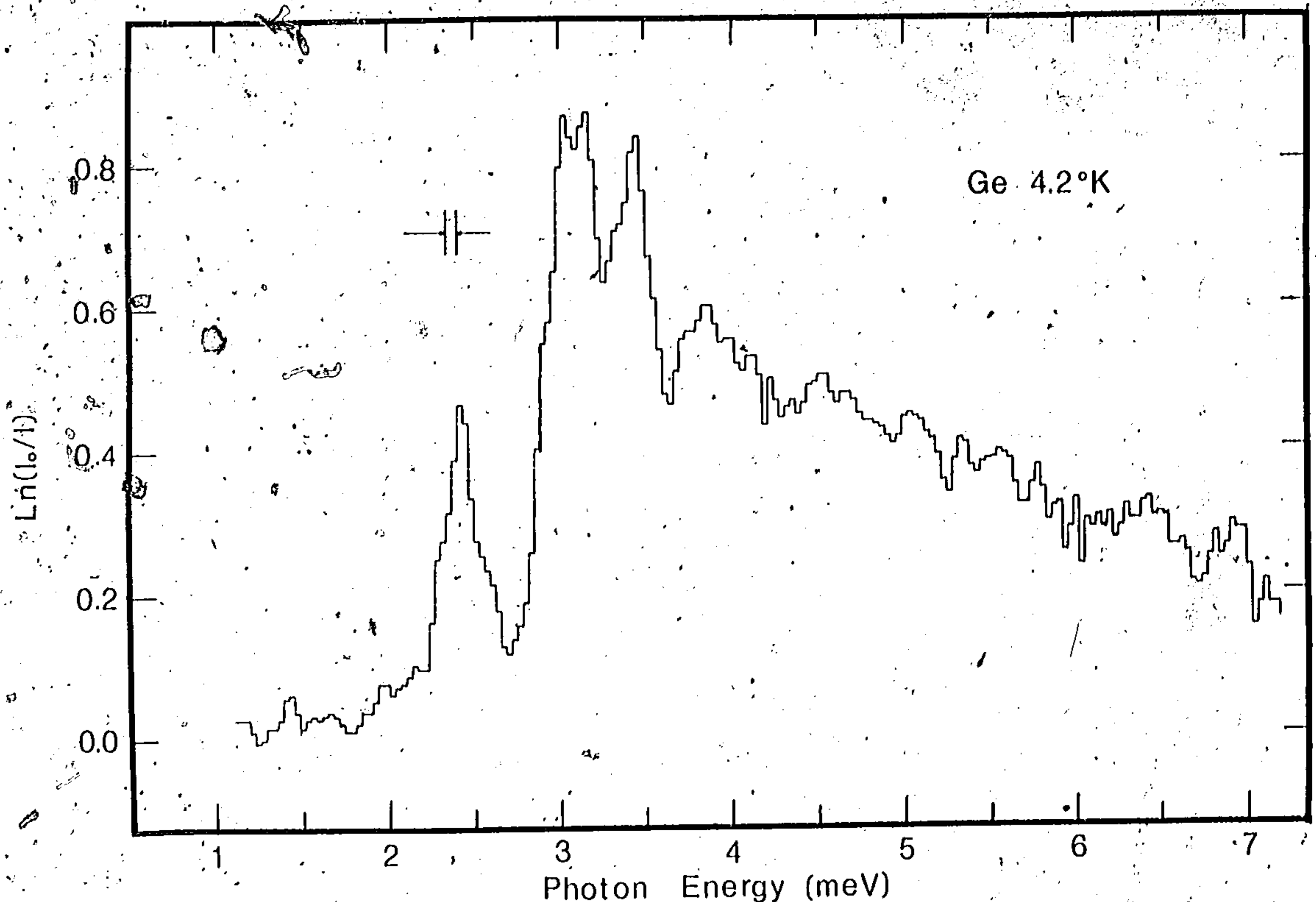
Ge 4.2°K
Ln(Io/I)
0.8
0.6
0.4
0.2
0.0
1
2
3
4
5
6
7
Photon Energy (meV)

than the baseline noise. Above 3.6 meV an absorption continuum can be seen that reaches its maximum value at 3.85 meV and extends to energies higher than 7 meV.* The structure on this tail is due to noise.

Figure 4-3 shows the exciton spectrum at 5 K in the spectral region from 1.5 to 5.5 meV. The peaks which are clearly visible are at 2.15, 2.45, 2.56, 3.03, 3.15 and 3.45 meV, with 0.01 meV of accuracy in the position. There is also some very important structure visible, in particular a very strong intensity shoulder with maximum centered at 2.37 meV, a new peak at 2.72 meV and a shoulder with maximum centered at 3.70 meV. There is some structure below 2 meV but the high level of the noise for this spectrum in this region makes very difficult the identification of any possible transitions in this region. The spectrum at this temperature displays quite clearly the trend of the lines at 2.37, 2.56 and 3.03 meV to grow with temperature, while the peaks at 2.45, 3.16 and 3.45 remain at more or less the same ratio in intensity as they appear at 3 K. Also at 5 K the peaks appear broadened and as a consequence the line at 3.35 meV is no longer visible having been overlapped by the peak at 3.45 meV which has an estimated width larger than .32 meV. At both 5 K and 4.2 K a shoulder on the low energy side of the 3.03 meV line is visible. As the width of all the lines increases with temperature, it is very difficult to assign this shoulder completely to the line at 2.88 meV.

FIGURE 4-3

The absorption spectrum of excitons in germanium at 5 K. The region below 1.5 meV is dominated by noise. The resolution is 0.06 meV.

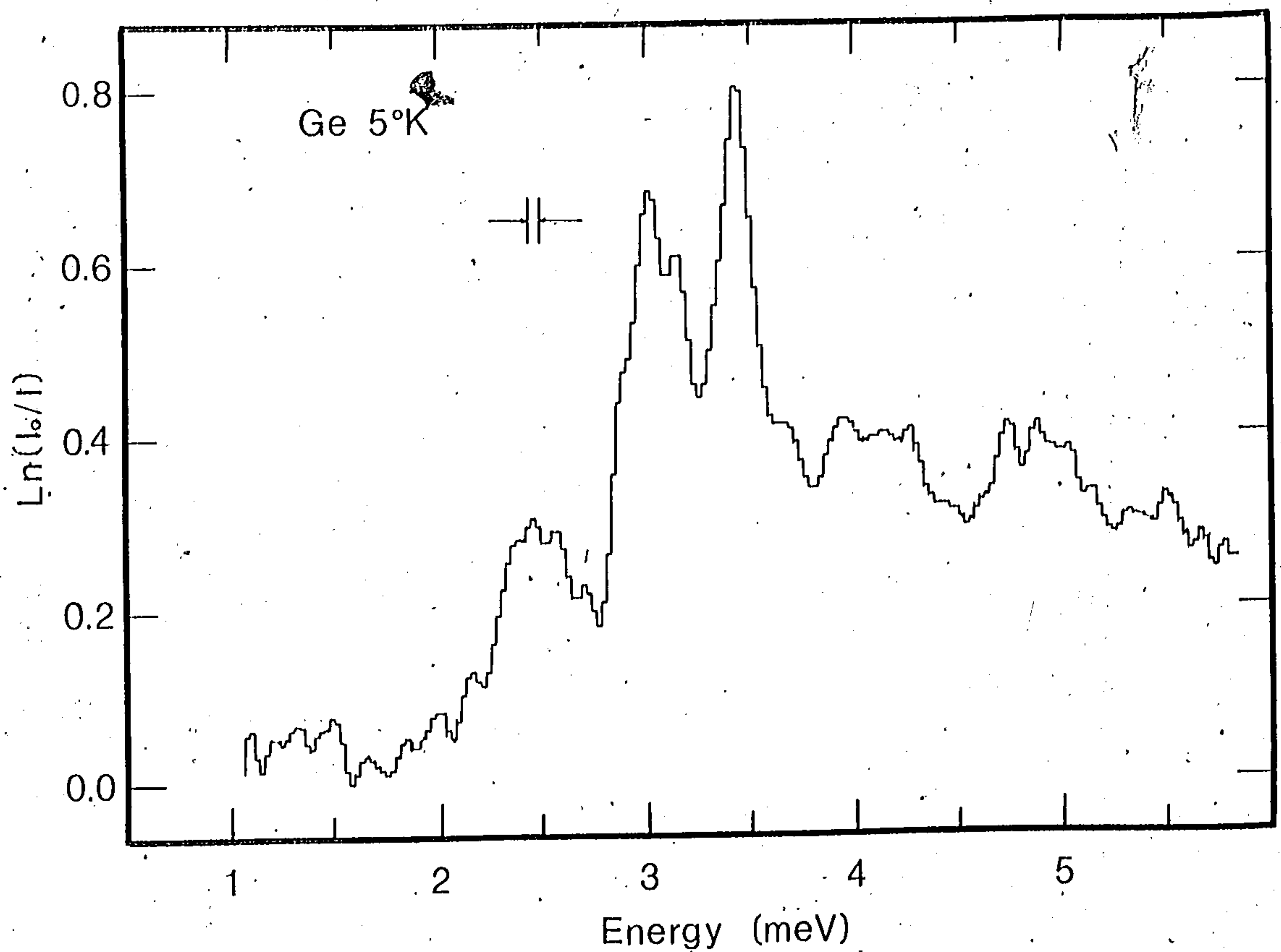
Ge 5°K
0.8
0.6
0.4
0.2
0.0
Ln(I₀/I)
1
2
3
4
5
Energy (meV)

A possible explanation is the onset of transitions from the "heavy" $1S^{3/2}_{1/2}$ ground state to the continuum, similar to the continuous absorption tail produced by the "light" ground state discussed below.

The continuous absorption tail extending from 3.75 to energies higher than 7 meV shows a maximum at 3.85 meV at 4.2 K and at 3.98 at 5 K. The tail corresponds in energy to transitions to the ionization continuum from the deeper ground state $1S^{3/2}_{3/2}$. The noise in the tail is high in the three spectra presented. In the work of Buchanan and Timusk (1976) it is found that the maximum of the ionization continuuum is around 4.2 meV. The ionization energy for the lowest ground state has been measured as 4.17 meV by Frova et al (1975) and theoretically calculated as 4.20 meV by Lipari; Alterelli and Tosatti (1977). This kind of behaviour for transitions to the continuum that start and peak after the ionization energy, has been obtained theoretically for excitons with highly anisotropic, ellipsoidal and nondegenerate valence and conduction bands, in the limit of infinite reduced mass in the direction of anisotropy by Shinada and Sugano (1966). These conditions are not completely satisfied for the excitons in Ge which involve valence bands which are degenerate and nearly spherical. Then one will expect that an extension of the energy might produce a similar result for the excitons in Si and Ge.

Summarizing the three sets of experimental observations it is possible to say the following: there is a set of transition lines whose relative intensity is almost insensitive to the temperature with positions at 2.15, 2.43, 3.14, 3.35 and 3.44 meV. There is also a set of transitions with temperature dependent intensity at 2.35, 2.55, 2.88 and 3.03 meV and another group of possible transitions at 2.72 and 3.70±0.02 meV. For almost all transitions the accuracy in the position is 0.01 meV. Transitions from the "shallower ground state" will be dependent on the temperature-varying population of the level. Hence the strongly temperature sensitive transition can be identified as originating from the upper ground state $1S^{3/2}_{1/2}$. Another useful criterion in the assignation of transitions is the measured value of the ground state splitting of 1.01±0.03 meV (Frova et al. 1975). Comparing the values obtained for the lines in the experiment one can see the following pairs of lines separated by 1.01±0.03 meV: (2.15, 3.14), (2.43, 3.44), (2.35, 3.35) and (2.72, 3.70) meV. A final identification of the observed transitions can be made combining the present experimental results with the theoretical calculations of LA. This is presented in table 3-5. In table 4-1 the assignations in this table were made by LA based on the experimental work of Kononenko et al. (1974) and Buchanan and Timusk (1977). The only new contribution is the observation of transition lines at 2.72 and 3.70 meV, which agree well with the theoretical values for the transitions $1S^{3/2}_{1/2} \rightarrow 2P^{1/2}_{1/2}$ and $1S^{3/2}_{3/2} \rightarrow 2P^{1/2}_{1/2}$ respectively.

The agreement between the LA results and the observed transitions is extremely good for most of them. However, at least one of the expected transitions (at 1.27 meV) in table 4-1 has not been observed. Also the nature of the strong peaks at 2.88 and 3.03 meV is not well established in their work. These peaks have been assigned as transitions from the $1S^{3/2}_{1/2}$ ground state to P states of higher order series, due to their strong temperature dependence. Their unusually large intensity, could be at least partially explained if these two levels have energy dispersion relations which parallel in k space the dispersion relation of the heavy ground state. This is equivalent to saying that these two states have heavy effective masses. In this case the joint density of states is enhanced, a quantity to which the optical absorption is directly proportional. Buchanan and Timusk (1976) have also suggested as an extra explanation the possibility for these states to have long recombination lifetimes. But to the best of our knowledge no experimental or theoretical work can substantiate either of these two propositions at the present time.

3. The Exciton Spectrum in a Small Magnetic Field

The nature of the exciton transitions in germanium can be further probed by looking at their response to an externally applied magnetic field. Experiments done in this physical situation provide new information that can be used to check the

Table 4-1

Comparison between theory and experimental results for optical transitions between different energy levels of indirect excitons in germanium.

Observed transitions Energy (meV)	Theory Energy (meV)	Assigned transitions
	1.27	$1S^{3/2}_{1/2}\to(2P^{3/2}_{3/2}2P^{5/2}_{3/2})$
2.15	2.05	$1S^{3/2}_{1/2}\to 2P^{3/2}_{1/2}$
2.35	2.29,2.30	$1S^{3/2}_{3/2}\to(2P^{3/2}_{3/2}2P^{5/2}_{3/2})$;$1S^{3/2}_{1/2}\to(2P^{5/2}_{1/2}2P^{5/2}_{-5/2})$
2.43	2.40,2.41	$1S^{3/2}_{1/2}\to(2P^{5/2}_{3/2}2P^{3/2}_{3/2})$;$1S^{3/2}_{1/2}\to(2P^{5/2}_{-5/2}2P^{5/2}_{1/2})$
2.55		
2.72	2.72	$1S^{3/2}_{1/2}\to 2P^{1/2}_{1/2}$
2.87		
3.03		
3.04	3.07	$1S^{3/2}_{3/2}\to 2P^{3/2}_{1/2}$
3.35	3.33	$1S^{3/2}_{3/2}\to(2P^{5/2}_{1/2}2P^{5/2}_{-5/2})$
3.44	3.42,3.43	$1S^{3/2}_{3/2}\to(2P^{5/2}_{3/2}2P^{3/2}_{3/2})$;$1S^{3/2}_{3/2}\to(2P^{5/2}_{-5/2}2P^{5/2}_{1/2})$
3.70	3.74	$1S^{3/2}_{3/2}\to 2P^{1/2}_{1/2}$

theoretical understanding of the exciton spectrum. Hence a series of experiments described in this section were performed to test the identification of exciton levels provided by the theoretical model of Lipari and Altarelli. It is important to work in the régime of small fields. Too strong a field will alter radically the theoretical picture discussed in chapter III, as the effect of the field becomes comparable with or larger than some of the other terms in the exciton Hamiltonian (3-23). In the régime of small fields it is possible to use perturbation theory as a mathematical tool to analyze the results, using the same scheme of states provided by the theory at zero field.

Although a precise estimate of values of the field for which perturbation theory gives reasonable results is very hard to come by, a feeling for it can be obtained by looking at the effect produced by the different terms of the Hamiltonian. As an example, the effect of the "spin-orbit coupling" term in the spherical approximation eq. (3-25), was discussed in chapter 3. There in table 3-3 it can be seen that the energy shifts produced by this term of the Hamiltonian alone correspond to magnetic fields of several tens of kOe. The combined effect of all terms of the Hamiltonian is to produce a large scattering in the energy of the levels, from 2.35 to 3.74 meV for 2P levels, compared with an expected value of 3.14 meV for n = 2 states for a hydrogenic system with an effective Rydberg constant of 4.18

meV. The resulting separation between the energy levels varies typically by several tenths of an meV, which again corresponds to magnetic energies produced by fields of several tens of kOe. The only exception is the separation between the calculated positions of the states $(2P^{5/2}_{-5/2}, 2P^{5/2}_{1/2})$ and $(2P^{5/2}_{3/2}, 2P^{3/2}_{3/2})$ which is calculated by LA to be 0.02 meV, which corresponds to 3.5 kOe. The two levels are so close that they cannot be resolved under the conditions in which all experiments for indirect excitons at zero field were performed. In any case these two states belong to different irreducible representations and hence their wavefunctions have expansions in terms of different sets of states $nL^F_{F_z}$, i.e. the two expansions are composed of states with independent F_z values. Hence there cannot be an interaction between these two levels as their expansions are totally uncoupled. As a consequence these two levels can cross each other without affecting their respective magnetic behaviour.

Another useful criterion to define the small field régime is the value of the dimensionless reduced field $\gamma = e\hbar H/(2\mu_0 R_0 C)$ introduced by Altarelli and Lipari (1973). R_0 is the exciton Rydberg constant (3-15) and μ_0 is the exciton "reduced mass" (3-17). In their work Altarelli and Lipari found that a perturbative treatment for the simplified hydrogenic model for excitons is good for values of γ below about

0.4 for the ground state. Using this value an upper limit of 8.5 kOe is obtained for the validity in indirect excitons in Ge.

With these facts in mind the magnetic responses of the exciton transitions in Ge were measured experimentally from zero to 7 kOe in steps of 500 Oe. The magnetic field was applied parallel to the <100> crystallographic direction. In this geometry the excitons associated with the four electronic ellipsoidal constant energy surfaces along the <111> directions produce the same contribution to the spectrum. The Faraday configuration was used in which the radiation incident on the crystal propagates parallel to the magnetic field. Figure 4-4 shows the spectra of indirect excitons in germanium at 0, 2, 4, 6 kOe at 4.2 K. The resolution is 0.1 meV which is two times less precise than for the spectra of figures 4-1, 4-2 and 4-3, except for the spectrum at 4 kOe which was done at a resolution of 0.06 meV.

At 0 kOe three peaks are indicated and labelled as E_1, E_2 and E_3. They correspond to a line at $E_1 = 2.43$ meV, E_2 to the coalescence of the peaks at 3.03 and 3.14 meV, and E_3 to a line at 3.44 meV. For the spectra at the other values of the field in the figure, only the peaks which were consistently observed when incrementing the field have been labelled and indicated. From the figure it is immediately noticeable that there is almost no magnetic response of the exciton line E_1.

Figure 4-4

Absorption spectra of indirect excitons in germanium at four different values of the magnetic field. The magnetic field was applied parallel to the <100> direction of the crystal in the Faraday configuration. The baselines of the spectra at 2, 4 and 6 kOe have been shifted. The zero of the absorption for each of the spectra is given by the corresponding baseline. Notice that the spectrum at 4 kOe has been done at higher resolution, to show the two split lines E_3 and E_6. At 6 kOe the line E_3 has moved further in the high energy direction and at the lower resolution it appears as a shoulder on the line E_6.

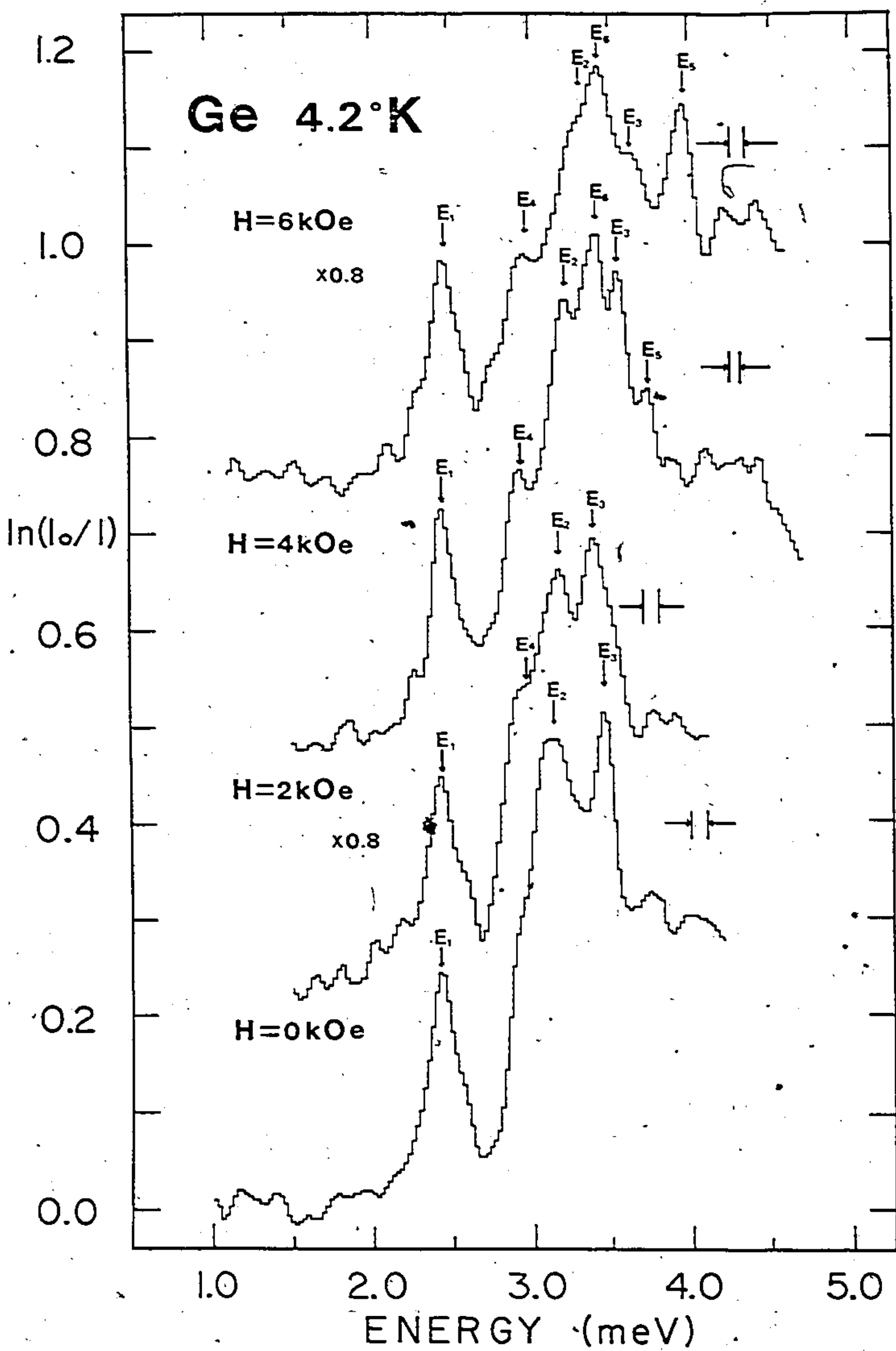
Ge 4.2°K
H=6kOe
x0.8
H=4kOe
H=2kOe
x0.8
H=0kOe
E1
E2
E3
E4
E5
E6
ln(Io/I)
0.0
0.2
0.4
0.6
0.8
1.0
1.2
1.0
2.0
3.0
4.0
5.0
ENERGY (meV)

9

From the low energy side of the peak E_2 a new peak is observable when the magnetic field increases. It has been labelled E_4. It is remarkable that at 2 kOe the appearance of the line E_4 coincides with the "sharpening" of the exciton line E_2. The latter is eventually displaced until it coalesces with the line E_3 at 6 kOe, where it is seen as a shoulder. Thus it has been possible to trace E_2 as the exciton line at 3.14 meV moving with the magnetic field, and E_4 as a line coming from 3.03 meV. The E_3 exciton line shows already a widening at 2 kOe and an apparent shift to lower energies, with a component starting to emerge at the high energy side. At 4 kOe the line E_3 has already split and the low energy component which has been labelled E_6 is clearly visible. There is also a new line on the high energy side of E_3 which seems to originate also from the line at 3.44 meV.

In figure 4-5 all the observed transitions are plotted as a function of magnetic field. The solid lines in the figure are the fit of the theoretical model discussed in the next section. The points plotted at zero field are only the transitions observed at the lower resolution absorption curve of figure 4-4. In addition to the exciton lines already discussed, there are some other transitions, the positions of which fall on a smooth curve when plotted as a function of the field. They have been labelled E_7, E_7', E_8 and E_9. The transitions E_7, E_7' seem to originate from the exciton line at 2.35

Figure 4-5

Diagram of the observed energies of the exciton transitions in germanium as function of the magnetic field in the Faraday configuration. For the exciton line (E_1, E_1') the size of the circles encompasses the uncertainty in its position. The three points shown with dotted horizontal bars represent possible transitions observed as very faint shoulders. The solid lines represent the theoretical fit obtained with the model discussed in the text. The primed exciton labels refer to the low energy going transitions, "partners" of the transition of same label.

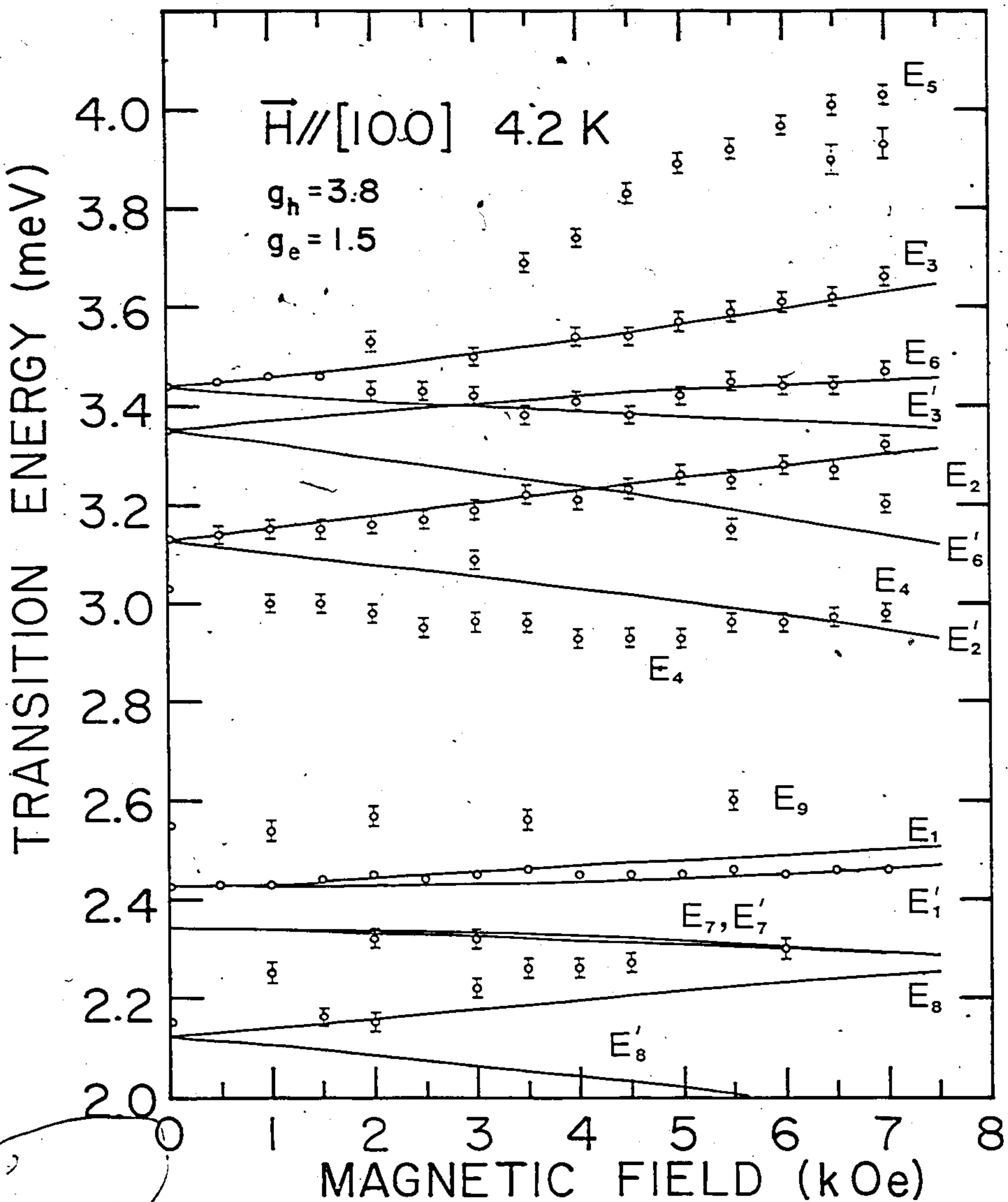

$\vec{H}$//[100] 4.2 K
g_h = 3.8
g_e = 1.5
TRANSITION ENERGY (meV)
MAGNETIC FIELD (kOe)
4.0
3.8
3.6
3.4
3.2
3.0
2.8
2.6
2.4
2.2
2.0
0
1
2
3
4
5
6
7
8
E_5
E_3
E_6
E_3'
E_2
E_6'
E_4
E_2'
E_4
E_9
E_1
E_1'
E_7, E_7'
E_8
E_8'

meV at zero field. At the lower resolution at which these experiments were done, only three points could unquestionably be distinguished for these transitions, and the point at 6 kOe might also be a superposition with the exciton line labelled as E_8. The transition lines E_8 at 1.5 and 2 kOe almost certainly originate from the line that peaks at 2.15 meV at zero magnetic field. The three points between the theoretical lines E_8 and (E_7, E_7') at 3.5, 4 and 4.5 kOe are very probably the peaks of the envelope of the three exciton lines E_7, E_7' and E_8. The negative-going branch of the E_8 transition, E_8' approaches very quickly energies below 2 meV where it could not be reliably studied because the transition was too weak. There is another set of transitions labelled by E_9 which seem to originate from the line at 2.55 meV. These transitions always appeared as a small shoulder on the exciton line from 2.43 meV (E_1, E_1'). Then the negative-going corresponding transitions having very similar shifts in energy with the field, will have to move towards the (E_1, E_1') lines and consequently they will be very hard to detect. Below the E_2 line there are three points almost parallel to it. They correspond to transitions barely resolved from the E_2 peaks. They might correspond to a superposition of the positive-going branch of the exciton line E_4 with E_3 at 3 kOe and E_6 at 5.5 and 7 kOe. In the region from 3.0 to 3.50 meV many possible transitions are expected to be piled together. On the top of that, the absorption produced from transitions to the continuum from the shallow ground state is also superimposed in this same region. The resolution of most experiments was 0.1 meV. When all of these factors are combined together, it is not surprising that we do not observe all the transitions which are theoretically possible.

4. Theoretical Model for the Exciton Response to a Small Magnetic Field

The more rigorous treatment in the effective mass model of the response of the exciton levels to an externally applied magnetic field requires finding the energy eigenstates of the Hamiltonian

$$H_{ex} = H_e(\vec{p}_e + \frac{e}{c}\vec{A}(\vec{r}_e)) - H_h(\vec{p}_h - \frac{e}{c}\vec{A}(\vec{r}_h)) - \frac{e^2}{\varepsilon|\vec{r}_e - \vec{r}_h|} + g_e\beta\vec{S}_e\cdot\vec{h} \quad (4\text{-}1)$$

where the vector potential is chosen to represent a uniform magnetic field $\vec{h}$:

$$\vec{A}(\vec{r}) = \frac{1}{2}(\vec{h}\times\vec{r}) . \quad (4\text{-}2)$$

The electron Hamiltonian is defined by eq. (3-4) with $\vec{p}_e \to \vec{p}_e + \frac{e}{c}\vec{A}(\vec{r}_e)$ and H_h is the full Luttinger Hamiltonian that describes the magnetic response of a hole state in the valence band (Luttinger 1956). The magnetic energy of the electron spin is not included in H_e so it has to be added as an extra term in eq. (4-1), where β is the Bohr magneton $\beta = \frac{e\hbar}{(2m_o c)} = 5.788 \times 10^{-6}$ meV/Oe, g is the g-factor of the electron and $\vec{S}_e$ the spin operator of the electron.

To work in the set of relative coordinates Dimmock (1967) has shown that the wavefunction for an exciton at rest in the presence of a magnetic field can be written,

$$F(\vec{r}_e,\vec{r}_h) = V^{-1/2}\exp\left(\frac{ie}{2\hbar c}\,\vec{H}\cdot(\vec{r}_e\times\vec{r}_h)\right)\times \times \sum_{j=1}^{r} f_j(\vec{r}_e-\vec{r}_h)\phi_c(\vec{r}_e)\phi_{vj}(\vec{r}_h) \tag{4-3}$$

where V is the volume of the crystal and ϕ_c, ϕ_{vj} are the bloch functions of the conduction electron and of the hole in the jth valence band, respectively. The sum is over the four degenerate valence bands. The envelope functions $f_j(r)$ where r is the relative coordinate, are eigenfunctions of the exciton Hamiltonian in terms of the relative coordinates:

$$H_{ex} = H_e\left(-i\vec{\nabla}_r + \frac{e}{c}\,\vec{A}(\vec{r})\right) - H_h\left(i\nabla_r + \frac{e}{c}\,\vec{A}(\vec{r})\right) - \frac{e^2}{\varepsilon r} + g_e\beta\vec{S}_e\cdot\vec{h}\ . \tag{4-4}$$

This Hamiltonian can be grouped in three terms in powers of the magnetic field h, written as follows

$$H_{ex}(\vec{h}) = H_{ex}(\vec{h}=0) + H_1(\vec{h})+H_2(h^2) \tag{4-5}$$

where $H_{ex}(h=0)$ is the same exciton Hamiltonian as eq. (3-7) or (3-23) in the particular case of germanium. $H_1(\vec{h})$ and $H_2(h^2)$ represent the Hamiltonian terms involving the magnetic field to the first and second powers, respectively.

The full Hamiltonian (4-5) is very complicated mathematically, and no exact solutions have been found for any values of the field. Several authors have discussed solutions to the problem of the excitons in a magnetic field using different approximations to the magnetic terms of the exciton Hamiltonian. These include, among others, Button et al. (1959), and Altarelli and Lipari (1973,1974) for the very similar problem of direct excitons. In particular a general treatment applying to the régime of small fields for indirect excitons in germanium is lacking in the literature. For this reason it was felt that it would be useful to study a simplified model that incorporates the most important physical characteristics of the exciton model of LA discussed in chapter 3. The LA model successfully explains many of the experimentally observed exciton transitions at zero field and provides a useful characterization of most of the states participating in the transitions.

The simplest Hamiltonian linear in the magnetic field should include: first, the interaction of the field with the orbital angular momentum of the exciton envelope function which describes the relative motion of the electron and hole; second, the interaction of the field with the "intrinsic spin" of the hole $\vec{J} = 3/2$; and third, the field interaction with the spin of the electron. Then the magnetic part of the Hamiltonian is

$$H_{mag}(\vec{h}) = (g_h - g_e)\beta\vec{L}\cdot\vec{h} + g_h\beta\vec{J}\cdot\vec{h} - g_e\beta\vec{S}_e\cdot\vec{h} . \qquad (4\text{-}6)$$

No quadratic terms in the field (diamagnetic terms) have been included in (4-6). The reason for this is that the magnetic fields under which most of the experiments were done were very small, and it is likely that any diamagnetic term would make a very small contribution, especially for the spectra at the smaller fields. In eq. (4-6) g_h is the g-factor of the hole in the bound excitonic system. It is interesting that for the two ground states ($\vec{L} = 0$, $\vec{F} = \vec{J}$) this proposed Hamiltonian is completely equivalent to the one proposed for the ground states by Button et al. (1959).

In the Faraday configuration the radiation has only two possible polarization states, called σ_+ and σ_-, which are in the plane perpendicular to the field. Hence dipolar transitions which require a polarization vector along the field are absent. This restricts the possible transitions to states which have $\Delta F_z = \pm 1$ and $\Delta F = -1, 0, 1$. Another selection rule is that dipolar transitions between 1S and 2P states cannot allow the spin of the electron to flip, or, equivalently, only transitions with $\Delta S = 0$ are allowed. These transition rules have very important consequences. For instance dipolar transitions from the lower ground state $1S^{3/2}_{\pm 3/2}$ cannot exist to any of the 2P states having $F_z = \pm 3/2$. By contrast transitions from the $1S^{3/2}_{\pm 1/2}$ ground state can exist to 2P states with $F_z = \mp \frac{1}{2}$ or $\pm \frac{3}{2}$.

A very important physical feature of the exciton states which has to be considered is that while the hole "spin" $\vec{J} = 3/2$ is strongly coupled to the orbital angular momentum $\vec{L}$ to give $\vec{F} = \vec{L} + \vec{J}$, the spin of the electron does not participate in any coupling scheme and hence is completely free apart from its coupling to the magnetic field $\underline{h}$. In this case the electron spin operator commutes with the exciton Hamiltonian and it is a good quantum number. Then the exciton eigenfunction (3-28) will not be a mixed combination of electron spinors. As discussed in detail in appendix C this situation also has the very important consequence for the spectral lines that no further splitting occurs due to the electron spin. We note that it was assumed that the exciton envelope wavefunction when spin has to be considered explicitly is:

$$F^{\pm}(\vec{r}) = \sum_i f(r)\,|n,L^i,F^i,F_z^i>\alpha^{\pm} \qquad (4\text{-}7)$$

where $\alpha^{\pm}$ represents a spinor with spin component up (plus) or down (minus).

As defined by eq. (4-7) the exciton wavefunction has no well-defined unique angular momentum L, but instead it is an infinite series of states $nL^F_{F_z}$. In principle one could just add the contribution to the magnetic energy of each one of the states weighted by the appropriate factor by which it contributes to the wavefunction. Unfortunately, the very restricted knowledge of the wavefunction available in the literature imposes the need of some extra assumptions in order to do the fit, as discussed below.

If just first-order perturbation theory could be used to fit the data plotted in the diagram of figure (4-5), a detailed knowledge of the radial function $f(\vec{r})$ in eq. (4-7) would not be necessary. The percentage contributions of the most important states $nL^{F}_{F_z}$ to the final probability amplitude were published by Lipari, Altarelli and Tosatti (1977). They are reproduced in table 4-2. Indeed perturbation theory was used but only to obtain "initial" values of g_e and g_h. But a look at the experimental results of figure (4-5) clearly shows that first order alone might not give the best fit to the observed behaviour of most of the transitions. As a detailed knowledge of the radial wavefunctions was not available, the simplifying assumption was made that all 2P states share the same common normalized radial function. In this case it has to be assumed that the orthogonality between wavefunctions describing different levels of the 2P multiplet has to be satisfied by the linear combination of states $nL^{F}_{F_z}$.

The complete magnetic Hamiltonian is given by

$$H_{ex}(\vec{h}) = H_{ex}(\vec{h}=0) + H_{mag}(\vec{h}) \qquad (4\text{-}8)$$

with $H_{mag}(\vec{h})$ given by (4-6). The proposed magnetic term is so relatively simple that it was decided to diagonalize this new Hamiltonian to obtain the eigenenergies of the different levels in the presence of the field.

To proceed with the diagonalization of the Hamiltonian a further simplification has to be made for the envelope wavefunctions. As mentioned before, these functions are an infinite series of $nL^{F}_{F_z}$ states. But the series are strongly convergent and also only the contribution to the probability amplitude of the first one or two states is available as shown in table 4-2. Hence it was decided to use just these angular functions, with the square root of the percentage coefficient given there as the coefficient of the states in the expansion, to represent the whole exciton envelope wavefunction. The "natural" simplification of keeping just the largest angular term and hence having a hydrogenic wavefunction, was felt not to be good enough to represent the physical situation of the exciton. This is because the characterization of the levels at 3.35 and 3.44 meV have very similar and actually symmetric expansions in the first two terms. In this case a strong interaction between these two states will be expected as the field is increased. The resulting hydrogenic approximation would give to these two levels radically different natures ($2P^{5/2}_{1/2}$ for the state at 3.35 and $2P^{5/2}_{5/2}$ for the other state), decoupling them completely, and the interaction expected for these two states would not be reproduced.

Table 4-2

Energy of the exciton states in germanium with the percentage contribution of the largest $nL^F_{F_z}$ states to the envelope wavefunction

State	percentage of component states	Energy (meV)
$1S^{3/2}_{3/2}$		0.0
$1S^{3/2}_{1/2}$		1.01
$(2P^{3/2}_{3/2}, 2P^{5/2}_{3/2})$	(62,10)	2.28 (theory)
$2P^{3/2}_{1/2}$	80	3.14
$(2P^{5/2}_{1/2}, 2P^{5/2}_{-5/2})$	(40,27)	3.35
$(2P^{5/2}_{3/2}, 2P^{3/2}_{3/2})$	(68,11)	3.42 (theory)
$(2P^{5/2}_{-5/2}, 2P^{5/2}_{1/2})$	90	3.73

From Lipari, Altarelli and Tosatti (1977).

The only possible transitions from the lower ground state $1S^{3/2}_{3/2}$ is to 2P states having $F_z = \frac{1}{2}$ in the presence of the magnetic field as discussed before. Now for the $1S^{3/2}_{1/2}$ ground state only the peak appearing at 2.43 meV at zero field might involve a transition to a 2P $F_z = 3/2$ series state, $1S^{3/2}_{1/2} \rightarrow (2P^{5/2}_{3/2}, 2P^{3/2}_{3/2})$, but this peak also involves the transition $1S^{3/2}_{1/2} \rightarrow (2P^{5/2}_{-5/2}, 2P^{5/2}_{1/2})$. As the line E_1 in fig. 4-5 does not show an observable tendency to split, it was impossible to trace experimentally the transition to the state with $F_z = 3/2$. For these reasons the diagonalization was only performed for the two sets of four possible 2P states with either $F_z = \pm \frac{1}{2}$. Under the simplified Hamiltonian (4-6) the result for the energy of the four split ground states (ignoring the additional double splitting of each of these states due to the electronic spin), performing the diagonalization, is identical to the expression for their energy in first order perturbation theory. The actual evaluation of the energy matrix elements is discussed in appendix C.

5. Results and Conclusions

The best fit to the experimental data is shown by the solid lines in Fig. 4-5. The best combination of values of g_e and g_h were $g_e = 1.5 \pm 0.3$ and $g_h = 3.8 \pm 0.2$, where any pair of values gives a reasonable fit. Fig. 4-6 shows schematically the transitions used for the fit. The fit was done in the following way: using first order perturbation theory and the slopes of the lines defined by the transitions E_3 and E_2, preliminary values of g_e and g_h were obtained. These values were then used to calculate the matrix elements of the Hamiltonian (4-8) and, from it, after diagonalizing it, the energy of the exciton levels for fields in steps of 250 Oe. The new set of calculated transitions was compared with the experimental data. Special attention was paid to the fit to the lines E_2, E_3 and to the peak composed of E_1, E_1'. During the process of doing the fit, it was found that the energy of the states was far more susceptible to the value of g_h than to that of g_e. Hence, the value of g_e was fixed first and then g_h was varied systematically. After the best value of g_h was established, g_e was varied to improve the fit. The uncertainty of g_h was established first by requiring that the calculated line E_3 not be more than twice the magnitude of the error bars from the observed E_3 point at 7 KOe. Secondly, the line E_2 was required to "pass through" as many of the observed E_2 points as possible. The uncertainty in g_e was established by looking at the increment necessary to displace the line an extra amount in energy equivalent to the magnitude of one error bar from the same point at 7 KOe.

It can be seen in Fig. 4-5 that the calculated transitions with the Hamiltonian provide a good fit for most of the peaks observed in the presence of the magnetic field. This model explains well why the E_1, E_1' lines at the resolution used, appear as a single peak. This is also the calculated case for the E_7, E_7' transitions. It also accounts well for the high-energy transitions E_2 and E_3. From the fit, it is also suggested that the apparent bending upward to higher energies for the peak E_6 is due to the cross-over of the high energy transition $1S_{-3/2}^{3/2} \rightarrow (2P_{1/2}^{5/2}, 2P_{-5/2}^{5/2})$ which comes from the line at 3.35 meV at zero field, with the negative-going transition E_3', which, according to Fig. 4-6, corresponds to $1S_{3/2}^{3/2} \rightarrow (2P_{5/2}^{5/2}, 2P_{-1/2}^{5/2})$. The exciton transitions E_4 and E_9 have not been fitted because of lack of knowledge about the characterization of the higher nP states to which they have to be assigned at zero field. The transitions E_4 show a very interesting bend towards higher energies which is difficult to attribute only to the superposition with transitions of the line E_2'. This bending may be due to the state originating from 3.03 meV being repelled by a similar P state of the same n and belonging to the same characterization ~~series~~ defined by Fz.

The transition E_5 could not be fitted by any dipolar transition between any of the 1S to 2P states. This transition can be extrapolated backwards to an energy of 3.16 meV at zero field. Then the E_5 line might be originating by a transition from the $S_{1/2}^{3/2}$ ground state to the continuum. This corresponds to the breaking of the exciton and the electron and the hole going to the first respective Landau level. Indeed, the energy necessary for this transition to the electron and light hole first Landau levels comes very close to actual observed energies of the transitions E_5. Such dipolar transitions are allowed from the exciton states $1S^{3/2}_{\pm 1/2}$ to the hole states $J = 3/2$, $M_J = \mp 1/2$, when the spin of the electron does not flip. The E_5 transitions are the only ones with an energy slope comparable to the transitions in the presence of a magnetic field observed by Muro and Nisida (1976). These two authors also noticed the very similar slope of those transitions, which they attributed originate from the exciton, to the energy slope of cyclotron resonances in the hole bands.

The value of g_e obtained in the fit is almost the same as that obtained by Button et al (1959), who got g_e=1.6±0.2, fitting the response of the ground states of the exciton in the high magnetic field regime, with the field along the <100> direction. The g_e value of the free electron in the same conduction band minimum in Ge has been calculated as 1.7 by Roth and Lax (1959), for the magnetic field applied in that direction. The present value of $g_h = 3.8 \pm 0.2$ is, however, 2.5 times that of the work of Button et al. It is closer and still smaller than their estimated value $g_h = 6.4$ for the free hole, thus pointing out the importance of binding effects for the magnetic response of the hole. Figures 4-7 and 4-8 show the magnetic splitting of the 2P and 1S states calculated with the values of g_e, g_h obtained in this work.

The information obtained from the experiments discussed in this chapter, i.e., the position of the observed transitions at zero field combined with the characterization of the states which was used to fit the transitions in the presence of a magnetic field, was used to determine the energy levels of the 1S and 2P states of the indirect excitons in Ge, shown in Fig. 4-9. The magnetic experiments were very insensitive to transitions to 2P states of the series with $F_z = 3/2$. Hence, as discussed in the text of this chapter, their position is not so well established experimentally as those of the other 2P states, and their positions are shown as dotted lines in Fig. 4-9. The energy of the states $(2P^{3/2}_{3/2}, 2P^{5/2}_{3/2})$ entered in the figure are theoretical values of LA. The energy separation of the two ground states obtained in these experiments is consistent with the value of Frova et al. Finally, the position of the $2P^{1/2}_{1/2}$ state was determined by the energy of the transition to it from the shallower ground state $1S^{3/2}_{1/2}$.

Figure 4-6

Schematic transitions used to fit the experimental results plotted in Fig. 4-5. These transitions correspond to the solid exciton lines drawn in that figure.

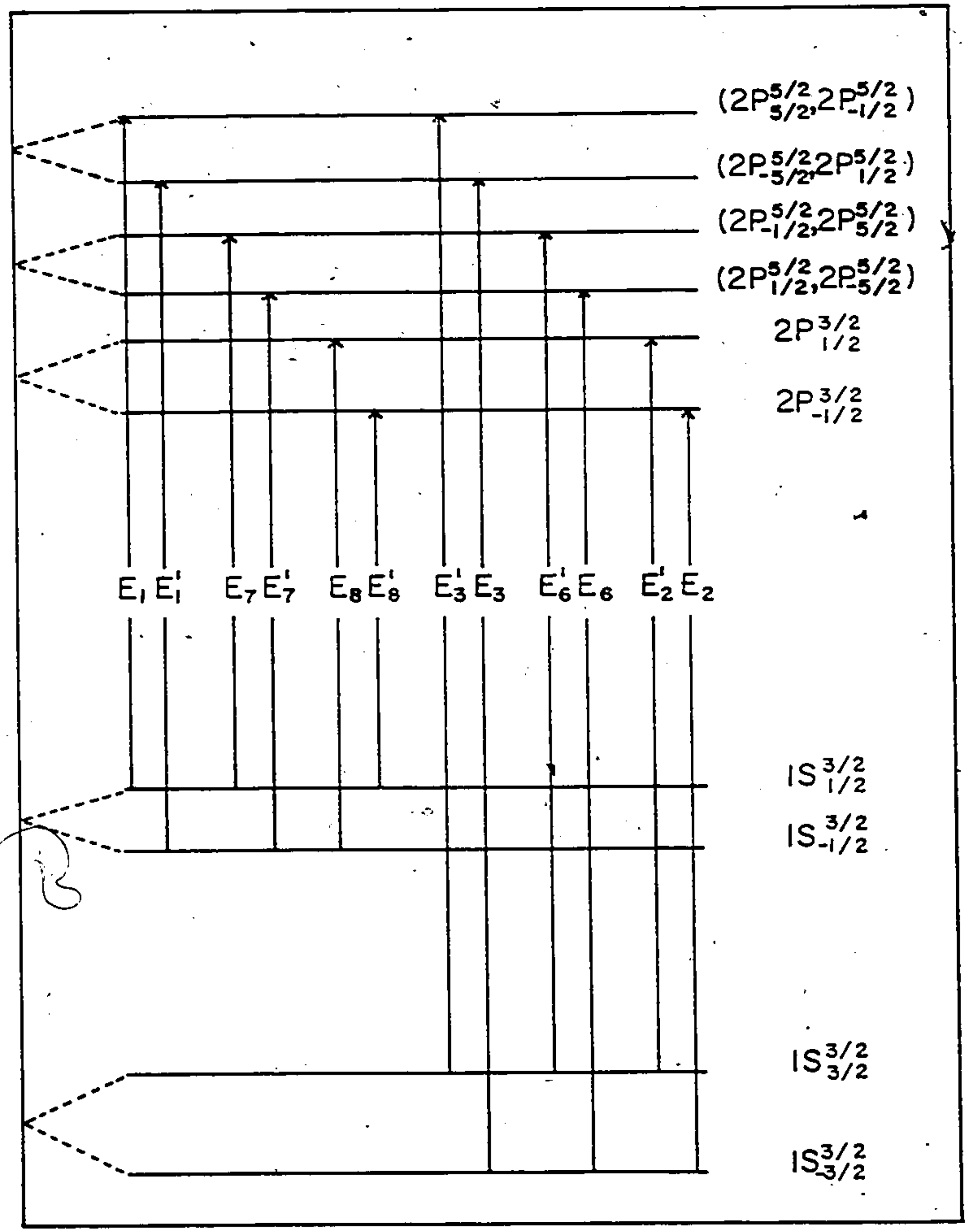

$(2P^{5/2}_{3/2}, 2P^{5/2}_{-1/2})$
$(2P^{5/2}_{-3/2}, 2P^{5/2}_{1/2})$
$(2P^{5/2}_{-1/2}, 2P^{5/2}_{3/2})$
$(2P^{5/2}_{1/2}, 2P^{5/2}_{-3/2})$
$2P^{3/2}_{1/2}$
$2P^{3/2}_{-1/2}$
E_1 E_1' E_7 E_7' E_8 E_8' E_3' E_3 E_6' E_6 E_2' E_2
$1S^{3/2}_{1/2}$
$1S^{3/2}_{-1/2}$
$1S^{3/2}_{3/2}$
$1S^{3/2}_{-3/2}$

Figure 4-7

Fan diagram for the 2P states as a function of the magnetic field, constructed with the parameters g_h and g_e indicated and the theoretical model proposed in this work. Only the levels with electronic spin component $S_z=1/2$ are shown. The levels with S_z-1/2 have a similar diagram, but with each point shifted downwards in energy gy $-g_e$ H. The energies of the two $F_z=3/2$ type states have been calculated only by first order perturbation theory.

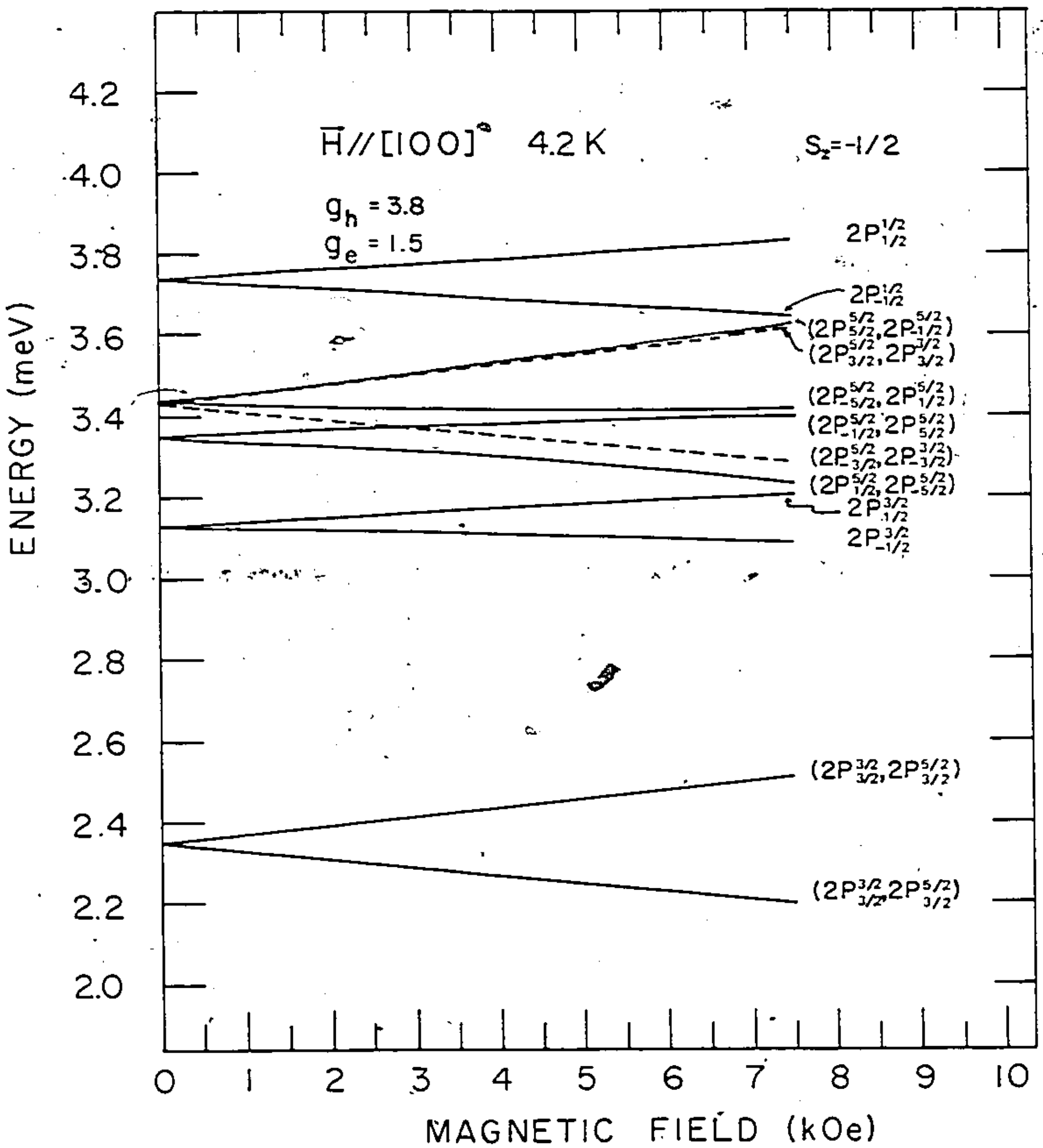

H//[100] 4.2 K
S_z=-1/2
g_h = 3.8
g_e = 1.5
2P^{1/2}_{1/2}
2P^{1/2}_{-1/2}
(2P^{5/2}_{5/2}, 2P^{5/2}_{-1/2})
(2P^{5/2}_{3/2}, 2P^{3/2}_{3/2})
(2P^{5/2}_{-5/2}, 2P^{5/2}_{1/2})
(2P^{5/2}_{-1/2}, 2P^{5/2}_{5/2})
(2P^{5/2}_{-3/2}, 2P^{3/2}_{-3/2})
(2P^{5/2}_{1/2}, 2P^{5/2}_{-5/2})
2P^{3/2}_{1/2}
2P^{3/2}_{-1/2}
(2P^{3/2}_{3/2}, 2P^{5/2}_{3/2})
(2P^{3/2}_{3/2}, 2P^{5/2}_{3/2})
ENERGY (meV)
4.2
4.0
3.8
3.6
3.4
3.2
3.0
2.8
2.6
2.4
2.2
2.0
0
1
2
3
4
5
6
7
8
9
10
MAGNETIC FIELD (kOe)

Figure 4-8

Fan diagram for the two ground states as a function of the magnetic field, constructed from the model proposed in the text. The solid bars represent the levels with electronic spin component $S_z = -1/2$. The broken lines indicate the states with electronic spin component $S_z = 1/2$.

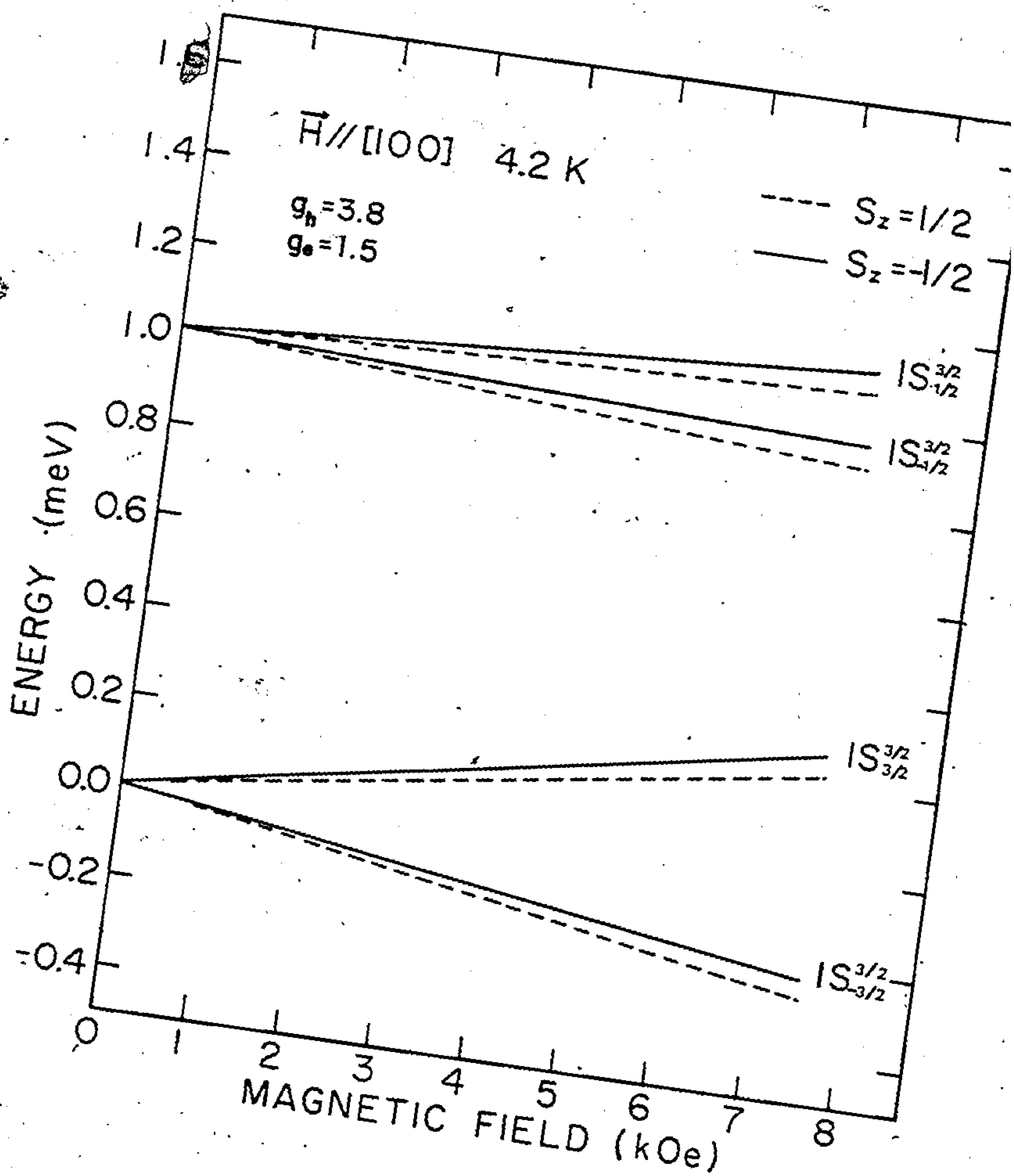

H // [100] 4.2 K
g_h=3.8
g_e=1.5
S_z=1/2
S_z=-1/2
$|S^{3/2}_{1/2}$
$|S^{3/2}_{-1/2}$
$|S^{3/2}_{3/2}$
$|S^{3/2}_{-3/2}$
ENERGY (meV)
MAGNETIC FIELD (kOe)

Figure 4-9

Indirect exciton spectrum in germanium, 1S and 2P states. The states in solid lines were obtained from the experiments discussed in the text. The energies of the states in dotted lines were taken from the theoretical model of Lipari and Altarelli. The energies are expressed in meV.

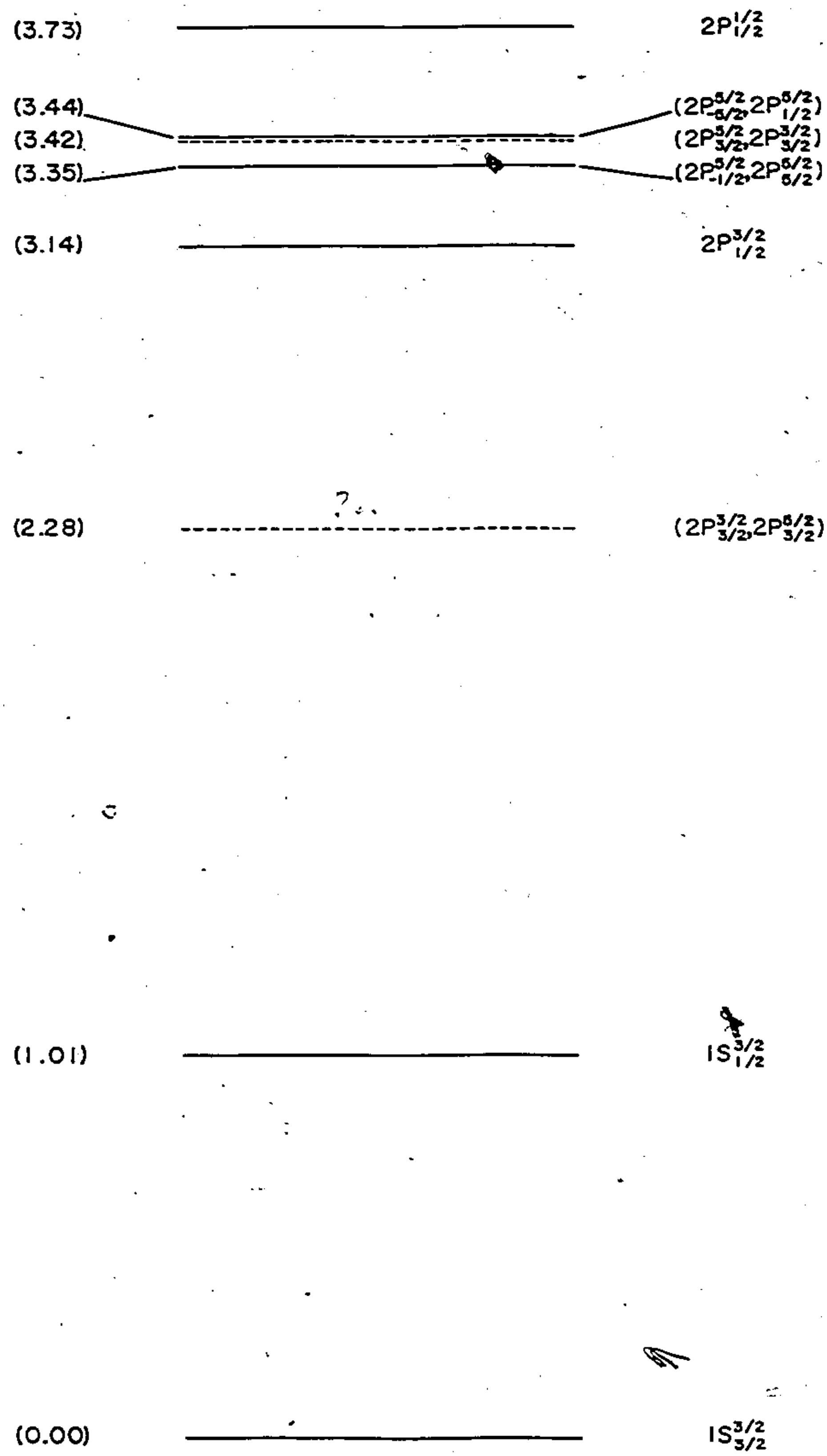
(3.73)
$2P^{1/2}_{1/2}$
(3.44)
$(2P^{3/2}_{-5/2}, 2P^{5/2}_{1/2})$
(3.42)
$(2P^{3/2}_{3/2}, 2P^{3/2}_{3/2})$
(3.35)
$(2P^{3/2}_{-1/2}, 2P^{5/2}_{5/2})$
(3.14)
$2P^{3/2}_{1/2}$
(2.28)
$(2P^{3/2}_{3/2}, 2P^{5/2}_{3/2})$
(1.01)
$1S^{3/2}_{1/2}$
(0.00)
$1S^{3/2}_{3/2}$

CHAPTER V

EXCITONS IN SILICON

1. Introduction

The LA model of the exciton Hamiltonian predicts that transitions between 1S to 2P states for the excitons in silicon have energies between 9.56 and 12.31 meV (Table 3-6). The absorption spectrum of silicon was studied under optical excitation in spectral regions ranging from 2 to 20 meV at several different temperatures from 6K to over 20K. The exciton absorption spectrum was found experimentally in the expected frequency region. The dependence of the absorption with temperature of the exciton gas in equilibrium with drops of electron-hole fluid is the subject of study in the second half of the chapter.

2. Experimental Results and Discussion

Figures 5-1, 5-2, 5-3, and 5-4 show the measured absorption spectra of the exciton gas in silicon at temperatures of 6.5K, 13K, 8.5K and 6K, and excitation powers of 160 mW, 240 mW, 180 mW and 100 mW respectively. These excitations produce a concentration of the exciton gas of the order of 10^{14} to 10^{15} cm^{-3}, a level well above the estimated impurity concentration of less than 10^{12} cm^{-3} of the crystal used. The temperature of the excitons was estimated to be higher than the crystal temperature measured by the thermocouple. A noticeable broadening of the exciton spectrum was observed by raising the excitation laser power for the same nominal temperature of the crystal read by the thermocouple. This is indicative of a substantial heating of the exciton gas to temperatures above that of the lattice. The temperature of all exciton spectra has been corrected for this effect. The amounts of the corrections were established by measuring the exciton spectra at 250 mW and 400 mW at the same nominal temperature of 13K. The two spectra were then fitted with three gaussian peaks at the positions of the "average peaks" at 10.20, 11.4 and 12.0 meV, to obtain the width of these lines. The width of the lines was then extrapolated for zero power at that temperature. Then, assuming a linear dependence of the zero power width with the temperature, it was possible to compare the actual width of a spectrum of a given power and temperature, with the temperature that produced the same width for the zero power line. For instance, the line width at 160 mW and 6K nominal temperature had the same width as the 8K extrapolated zero power line. Roughly, 80 mW produced 1K higher temperature for the exciton gas.

Figure 5-1 shows the exciton spectrum at an experimental resolution of 0.20 meV and 16.5K of temperature. There is a series of peaks at 10.38, 11.40 and 11.98 meV as the most prominent features of this spectrum. At the low energy side

Figure 5-1

Spectrum of indirect excitons in silicon at 0.2 meV of resolution, 160 mW of excitation power and 16.5K of temperature. The peaks of energies between 10 to 12.30 meV correspond to 1S→2P transitions. The peaks at higher energies probably correspond to transitions from the two ground states to higher series of P states.

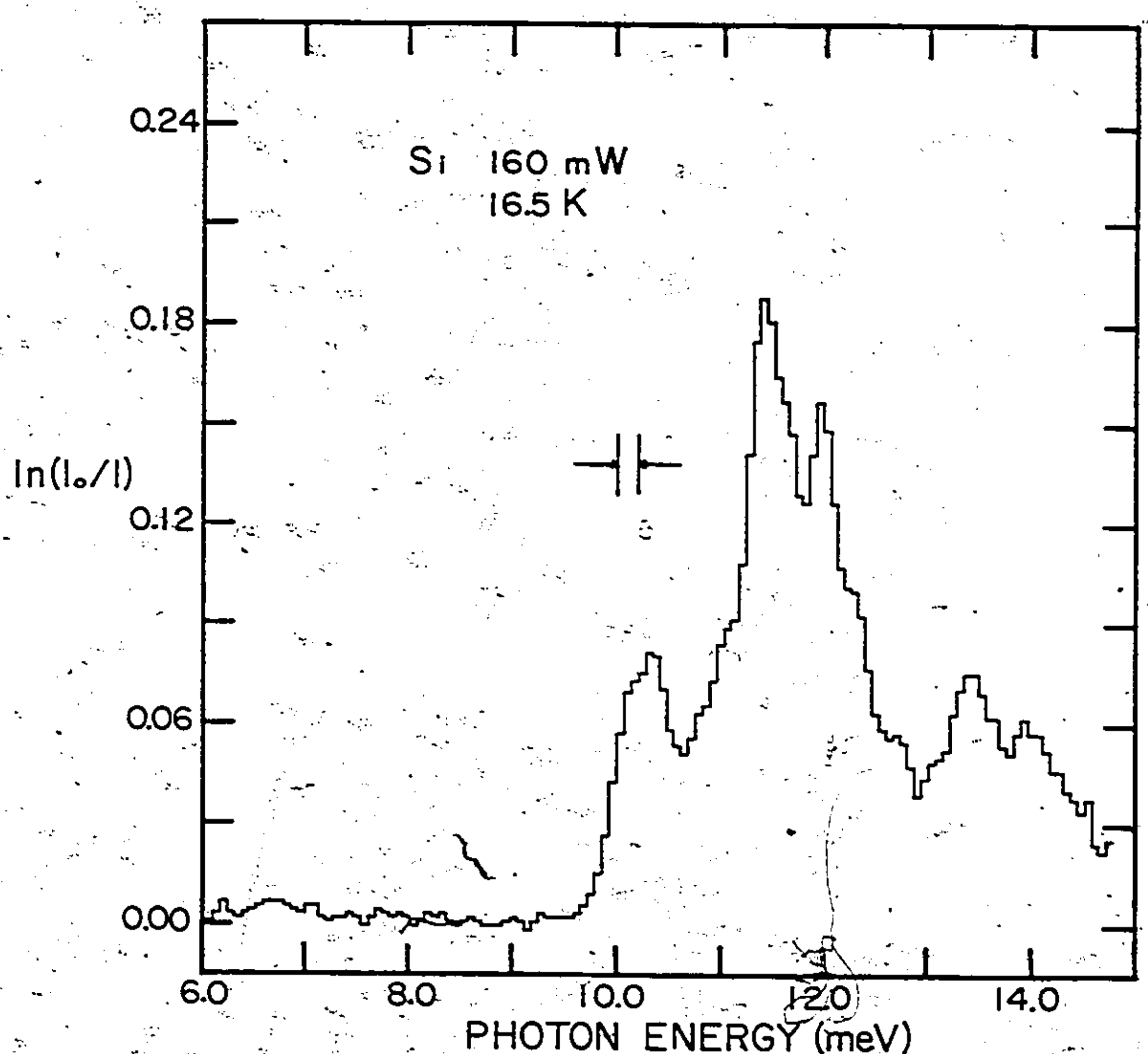
Si 160 mW
16.5 K
ln(I₀/I)
0.24
0.18
0.12
0.06
0.00
6.0
8.0
10.0
12.0
14.0
PHOTON ENERGY (meV)

of the peak, there is a strong shoulder indicative of the line centered at 10.1 meV visible at lower temperatures in the other spectra. Other structures indicative of some other possible transitions are visible at 11.06, 12.30, 12.70 and 13.4 meV. The peaks are measured with an uncertainty of the lines of around 0.02 meV in their position. The uncertainty of the lines in the shoulders is higher but difficult to estimate.

For the spectrum of Figure 5-2, the instrumental spectral resolution is 0.34 meV. The most prominent features are the two peaks at 10.2 and 11.45 meV, plus the shoulder at the high energy side of this peak, which corresponds to another peak at 12.0 meV. These peaks are in the energy region where the 1S to 2P transitions are expected (Table 3-6). In the figure, two possible extra peaks are observable at 13.40 and 14.0 meV. These very probably correspond to the envelope of transitions to P states of higher n series. A high energy tail extending from energies around 14 meV to above 20 meV can also be seen. This tail corresponds to transitions from the two split ground states to the ionization continuum starting at 14.7 meV (Shaklee and Nahory, 1970) and is very similar to that of excitons in Ge (Figure 4-2). This spectrum is typical of the kind of resolution that could be obtained at these temperatures.

As shown in Figures 5-2 and 5-3, it was necessary to

Figure 5-2

Spectrum of indirect excitons in silicon at 13K of tempreature, 240 mW of excitation power, and 0.32 meV of resolution. This spectrum has been measured in a larger spectral region to show the absorption tail above 14 meV which corresponds to transitions to the ionization continuum from the two ground states. The structure visible in this tail is due to noise.

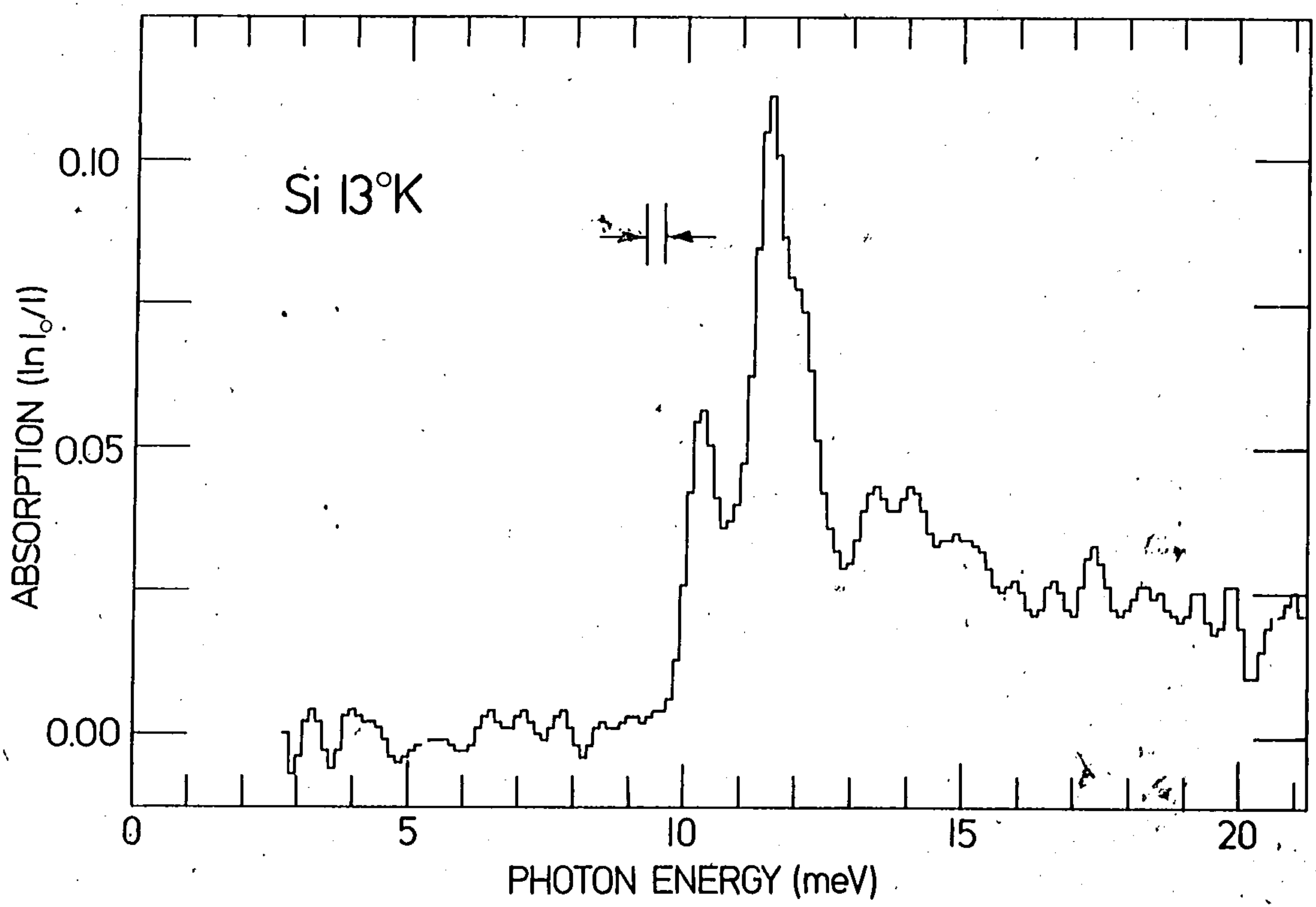
Si 13°K
ABSORPTION (ln I₀/I)
0.10
0.05
0.00
0
5
10
15
20
PHOTON ENERGY (meV)

Figure 5-3

Spectrum of the indirect excitons in silicon at 8K of temperature, 180 mW of excitation power and 0.2 meV of resolution. The structure below 9.5 meV is due to noise.

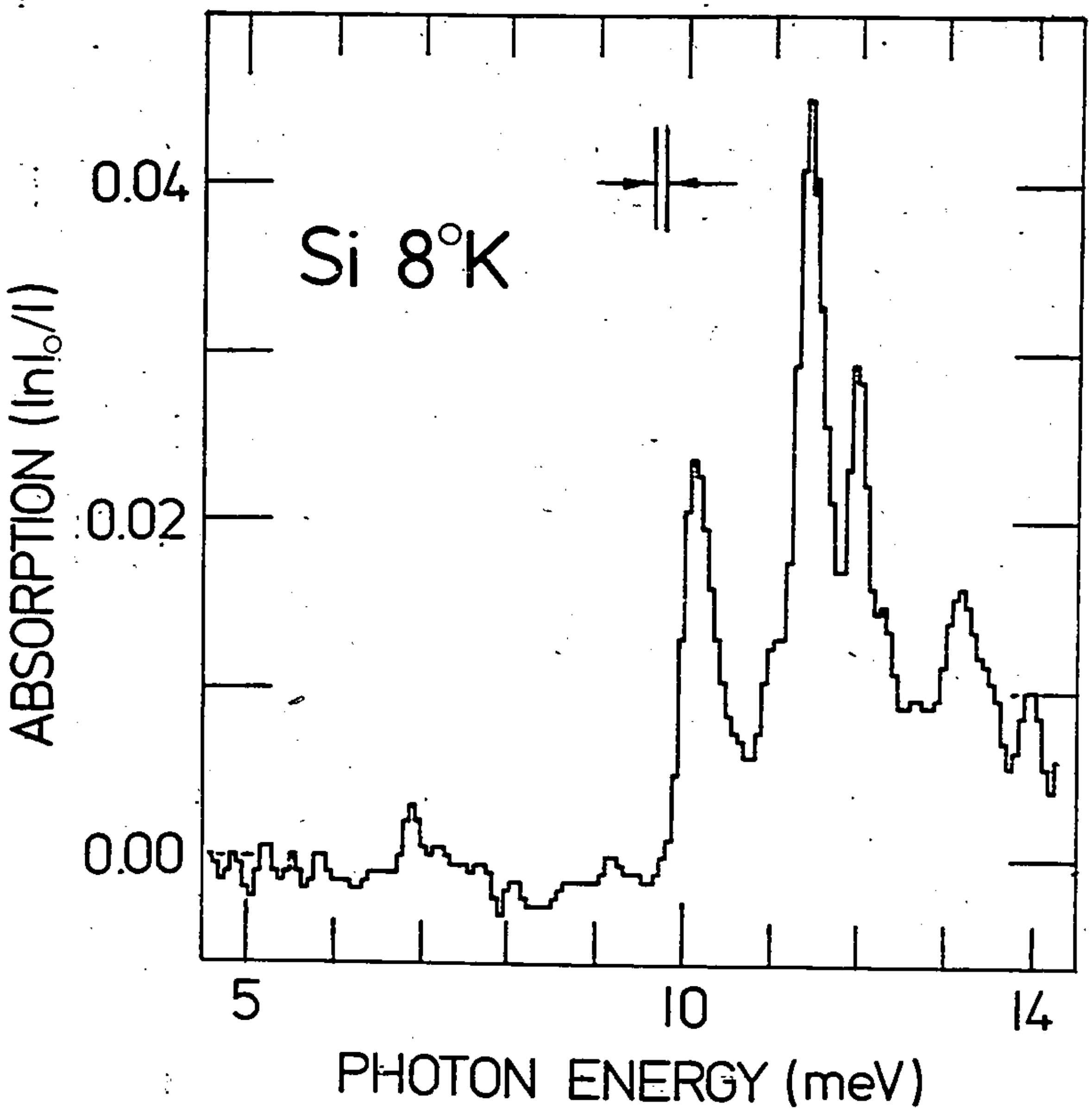
Si 8°K
0.04
0.02
0.00
ABSORPTION (lnI_o/I)
5
10
14
PHOTON ENERGY (meV)

Figure 5-4

Spectrum of the indirect excitons in silicon at 6K of temperature, 100 mW excitation power, and 0.1 meV of resolution. The insert shows the same spectrum but at 0.07 meV of resolution, obtained by removing the apodization of the interferogram source of this spectrum. The structure below 9.5 meV is due to noise.

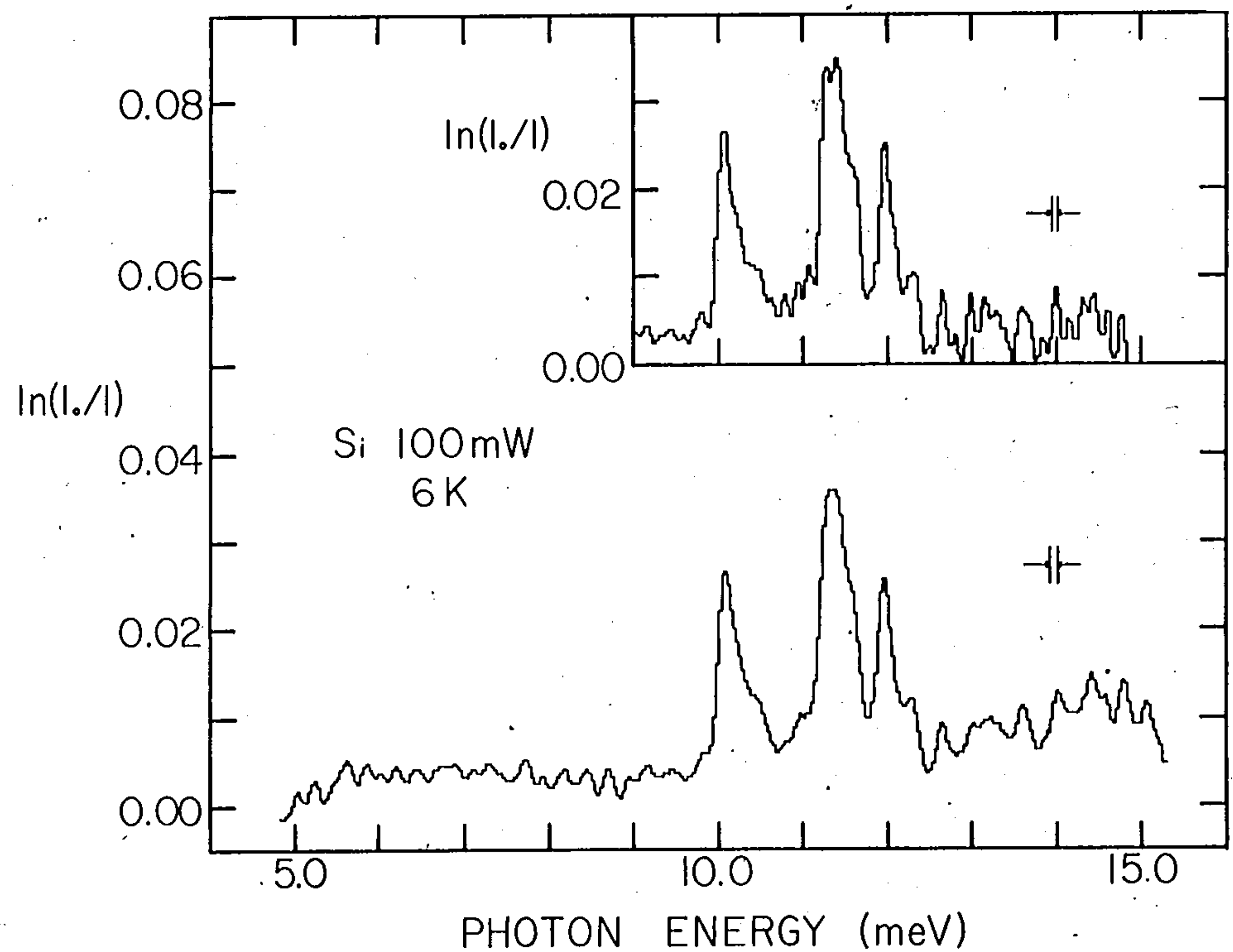

0.08
0.06
0.04
0.02
0.00
ln(I₀/I)
ln(I₀/I)
0.02
0.00
Si 100mW
6K
5.0
10.0
15.0
PHOTON ENERGY (meV)

97b

go to lower temperatures to increase the resolution of the lines. This also implied a smaller excitation power and, as a consequence, a smaller absorption. This put a practical limit on the maximum resolution that could be achieved. Figure 5-3, with a resolution of 0.2 meV, shows three prominent lines at 10.10, 11.42 and 11.98 meV. All of these peaks can be measured with an uncertainty of 0.03 meV in their position. Figure 5-4 presents the exciton absorption at a resolution of 0.1 meV. The following set of peaks are observed in this figure with an intensity several times that of the baseline noise: 10.08, 10.43, 10.97, 11.35 and 12.30 meV. There is also another peak at 9.84 meV, but with an intensity barely twice as big as that of the noise. The peak at 11.35 meV has been resolved as two peaks in the spectrum shown in the insert in the figure, with positions at 11.28 and 11.39 meV. Also, for this spectrum, the shoulder corresponding to a line at 11.68 meV is more evident. The uncertainty on the position of all these peaks is 0.02 meV. An examination of the four figures reveals that the peaks at 11.40 and 11.97 meV grow more in intensity with temperature than the peaks at 10.1 and 12.31 meV. The lines as 10.08 and 10.43 meV combine into a peak that appears at 10.20 meV at 13K and at 10.35 meV at 16.5K. This can be interpreted as a stronger temperature dependence for the peak at 10.43 meV. Also, the resulting peak of the peaks at 11.28 and 11.39 meV shifts from 11.35 meV at 6K to 11.40 meV at 16.5K. This suggests that with the rising temperature, the intensity of the peak at 11.39 grows faster than that of the peaks at 11.28 and 11.68 meV. Transitions from the shallower ground state $1S^{3/2}_{1/2}$ are going to be more temperature-dependent, as in the case of the excitons in germanium. Their temperature-dependence is given by the activation factor $\exp(-\Delta/kt)$, where is the anisotropy ground state splitting. When the intensity of the peaks at 11.4 and 12.0 meV is expressed in terms of that of the peak at 10.1 meV, their activation factor found is 0.36 ± 0.03 meV and 0.28 ± 0.03 meV respectively. The value of this ground state splitting for the excitons in silicon has been measured as $\Delta = 0.31 \pm 0.03$ in luminescence by Hammond and Silver (1978). Recently, a more detailed calculation by Lipari and Altarelli (1978) puts the theoretical value of this splitting as $\Delta = 0.32$ meV, as compared with the value of $\Delta = 0.46$ meV reported in Table 3-6. Hence, the values of the activation energy obtained for the peaks at 11.45 and 12.0 meV compare favorably with the values for Δ reported in the literature.

Of the exciton peaks observed, there are several pairs which are separated by values of 0.31 ± 0.04 meV when the uncertainty of the peaks is considered. They are (9.84, 10.08), (10.97, 11.28), (11.39, 11.68) and (11.97, 12.30) meV. For the last two pairs, the low energy "partner" transition from the shallower ground state $1S^{3/2}_{1/2}$ shows the appropriate temperature dependence expected. The peak at 10.08 meV corresponds very probably to a transition from the lower ground state $1S^{3/2}_{3/2}$. Its partner observed at 9.84 ± 0.03 is very weak. It is not expected to grow relatively more than by a factor of 1.4 at 13K. Thus, it will remain always very small and because of the important thermal broadening of the exciton lines (by factor of 3 from 8K to 13K using three gaussion lines to fit the spectra), it is completely masked by the line at 10.08 meV.

In Figure 5-5, a tentatively proposed energy scheme for the 1S to 2P transition based on these experimental spectra is presented. There are three transitions unobserved of the twelve expected. The transition at 10.43 has an apparent temperature dependence which is suggestive of a transition from the $1S^{3/2}_{1/2}$ ground state. As its expected partner at 10.7 meV is likely very weak and has not been observed, it has been indicated with a dotted line. The two remaining missing transitions, as for the case of excitons in Ge, quite probably correspond to transitions to a level which is so close in energy to some other that their transitions overlap and cannot be detected at the resolutions achieved.

A comparison of the levels obtained from the observed transitions, shown in Figure 5-5, with the calculated levels by LA in Table 3-6, shows good agreement for only two states at 10.08 and 12.30 meV (LA: 10.01 and 12.31 meV). For the

Figure 5-5

A tentative assignment of the observed far infrared $1S \rightarrow 2P$ exciton transitions in silicon. The energies in meV are measured from the ground state $1S^{3/2}_{3/2}$ of the exciton.

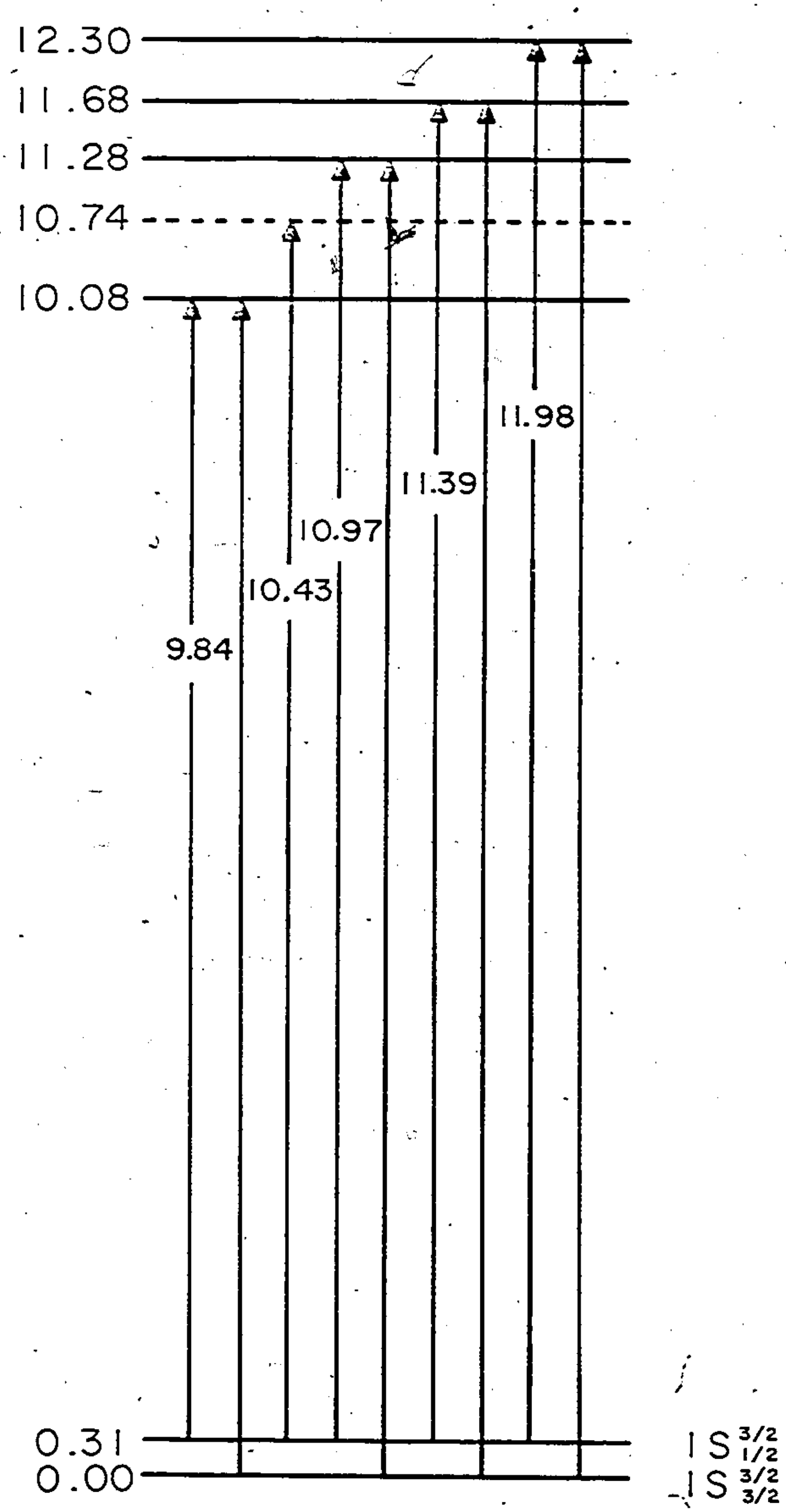
12.30
11.68
11.28
10.74
10.08
9.84
10.43
10.97
11.39
11.98
0.31
0.00
$1S^{3/2}_{1/2}$
$1S^{3/2}_{3/2}$

rest of the states, the difference in energy is of the order of 0.10 meV or more. However, in the calculations presented in that table, the energy of the anisotropy splittings is also overestimated by more than 50%. As mentioned before, LA have recalculated this splitting and obtained a far better agreement with the experimental results. It is felt that a fair comparison with the LA model can be done only when the energies of the 2P states for the excitons in silicon are also calculated in the same approximation in which the anisotropy splitting was done.

3. Condensation of the Exciton Gas into Electron-Hole Drops in Silicon

At the temperatures that the exciton spectra were studied, the exciton gas is expected to be in coexistence with small drops of electron-hole fluid (EHD) (Pokrovskii, 1972). A manifestation of this coexistence is the increase of exciton absorption strength with increasing temperatures up to a certain threshold temperature T_{th}. This threshold temperature varied with the excitation power. Above this temperature, the exciton absorption remained constant until ionization started to be appreciable above 30K.

Figure 5-6 shows the observed values of the absorption signal produced by the excitons in the spectral region, limited by a KCl filter, to 0 to 17.5 meV. From Figure 6-6, it can be estimated that around 50% of the total exciton absorption is located in this spectral region. It will be shown in the next chapter that the absorption produced by the EHD is completely negligible in this spectral region. The absorption signal due to excitons is proportional to the exciton concentration. At high temperatures, when all the drops have evaporated, the observed relation between excitation power and absorption coefficient can be used to calculate an absolute calibration between the absorption coefficient and exciton concentration. This calculation was done using two different methods. Both use the exciton spectrum at 240 mW and 23K (Figure 6-6), where the EHD are already absent.

The first method is the spectroscopic one proposed by Timusk (1976), which makes use of the well-known sum rule for the imaginary part of the dielectric constant $\varepsilon_2(\omega)$:

$$\int_0^\infty \omega\varepsilon_2(\omega)\,d\omega = \frac{\pi}{2}\,\omega_p^2\varepsilon_o \qquad (5\text{-}1)$$

where the plasma frequency of the excitons is given in terms of the exciton concentration n_{ex} by:

$$\omega_p^2 = \frac{4\pi e^2}{\varepsilon_o m^*}\,n_{ex} \qquad (5\text{-}2)$$

Here, $m^* = 0.122 m_0$ is the translational mass of the excitons in silicon (Altarelli and Lipari, 1977). The integrand in Equation (5-1) can be written in terms of the absorption constant $\alpha(\omega)$ as follows:

$$\omega\varepsilon_2(\omega) = 2nK\omega = cn\alpha(\omega) \qquad (5\text{-}3)$$

where $\sqrt{\varepsilon} = n + ik$. Making the approximation $n \approx \sqrt{\varepsilon_o}$, Equation (5-1) can be finally written as:

$$\int_0^{\infty} [\alpha(\omega) d] d\omega = \frac{2\pi^2 e^2}{c\gamma\varepsilon_o m^*} n_{ex} d \qquad (5-4)$$

where both the integrand and the right side of this equation have been multiplied by d, the diffusion length of the exciton. This was done because the measured quantity is ln(Io/I) = $\alpha(\omega)$d. From Equation (5-4), the integrated absorption signal will give the exciton concentration if d is known. Unfortunately, there are almost no measured values of d in silicon and none to the best of our knowledge under the focused excitation conditions at which the experimental work presented in this thesis was done. However, Dite et al (1977), using a value of d = 100 μm, constructed a phase diagram consistent with densities measured by spectroscopic methods and onset measurements, similar to the ones presented here. Their phase diagram is also consistent with that obtained by Shah et al (1977). Hence, their value for d was adopted in the present work.

The second procedure used to calibrate the exciton density is the kinetic method. This method uses the generation rate equation for the electron and holes produced by the radiation of the laser. When there is only exciton gas present, the exciton concentration is given by:

$$n_{ex} = \eta(1 - R) \frac{P}{V} \frac{\tau_{ex}}{h\nu} \qquad (5-5)$$

where η is the quantum efficiency for photoproduction of carriers, assumed to be equal to 1; R is the reflection coefficient of the crystal R = .3; P is the incident power,

$h\nu$ is the photon energy corresponding to λ = 6471A°; τ_{ex} = 3 x 10^{-6} sec. (Dite et al, 1977) is the exciton lifetime; and V is the volume occupied by the exciton gas. This volume depends not only on d but also on the geometry of the exciton distribution. For simplicity, $V = \pi r^2 d$ is used to compare with the spectroscopic results. Here, r = 0.16 cm is the radius of the illuminated spot. With these parameters, a value is obtained for n_{ex}, which is twice that from the spectroscopic method. As the kinetic method has added the uncertainty of the geometrical distribution of the exciton gas to the uncertainty in d, it was assumed the spectroscopic value is essentially correct, and $V = 2\pi r^2 d$ was adopted as the expression for the volume occupied by the exciton gas in any subsequent calculation. The result of the calculation is n_{ex} = 8.7 x 10^{14} at 240 mW and 23 K. The uncertainty is quite large and can be as large as a factor of 2.

Figure 5-6 shows the concentration of excitons as a function of temperature for three different excitation powers. The calibration outlined above was used to determine the absolute concentrations. The variation with temperature is very similar to that observed for excitons in Ge by Gershenzon et al (1976). They determined the exciton concentration by monitoring the 3.14 meV exciton line. The solid lines are the fit of the Pokrovskii (1972) model for the coexistence of the exciton gas with the EHD. This model is discussed below.

4. Pokrovskii's Model of the Coexistence of an Exciton Gas With EHD

This model proposes that under equilibrium conditions, the number of electron and hole pairs condensed in drops of uniform radius R at a given temperature is governed by three equations of which only two are independent.

The first equation establishes that in equilibrium, the generation rate per unit volume g of electron-hole pairs is equal to the rate of exciton recombination plus the rate of electron and hole recombination inside the drops.

$$g = \frac{n_{ex}}{\tau_{ex}} + \frac{\rho_o}{\tau_o} = \frac{n_{ex}}{\tau_{ex}} + \frac{4\pi}{3} R^3 N_o \frac{n_o}{\tau_o} \qquad (5\text{-}6)$$

where $\rho_o = \frac{4\pi}{3} R^3 N_o$; n_o is the number of electron-holes contained in the drops per unit volume; N_o is the concentration of drops per unit volume; n_o is the electron-hole density inside the drops; and τ_o is the recombination lifetime for an electron-hole pair inside the drop.

The second equation expresses the change rate of electron-hole pairs inside the drops per unit volume as the sum of three terms: the recombination of electron and holes; the evaporation of an electron-hole pair in the form of an exciton; and the capture of excitons from the surrounding gas:

$$\frac{d\rho_o}{dt} = \pi R^2 N_o n_{ex} v - 4\pi R^2 N_o A_r e^{-\phi/kT} - \frac{4\pi}{3} R^3 N_o \frac{n_o}{\tau_o} = 0 \qquad (5\text{-}7)$$

in equilibrium.

The last equation which is really the sum of Equations (5-6) and (5-7) expresses the decay rate of the exciton concentration as:

$$\frac{dn_{ex}}{dt} = g + 4\pi R^2 N_o A_r e^{-\phi/kT} - \frac{n_{ex}}{\tau_{ex}} - \pi R^2 N_o v n_{ex} . \qquad (5\text{-}8)$$

In these equations, $A_r e^{-\phi/kT}$ represents the evaporation rate of excitons from the drop, where ϕ is the condensation energy or "work function" of an exciton; A_r is a Richardson type of constant which will be a parameter obtained from the experiment. Usually, the constant would have involved a quadratic term in the temperature, but in Pokrovskii's model, this temperature dependence is neglected in comparison with the more strongly temperature-dependent exponential factor $e^{-\phi/kT}$. The velocity v for the exciton is the average thermal velocity of a classical Boltzmann distribution.

$$v = \sqrt{\frac{8kT}{\pi m^*}} . \qquad (5\text{-}9)$$

Equations (5-6) and (5-7) can be used to predict the exciton concentration observed in the experiment at a given temperature as a function of the parameters involved. In order to compare directly with the experiment, these equations have to be rearranged. The radius of the drops can be eliminated from these equations as well as ρ_o to obtain a single equation for n_{ex} as a function of the temperature and all the other parameters. The radius can be written as:

$$R^2 = \left(\frac{3}{4\pi n_o}\right)^{2/3} \left(\frac{\rho_o}{N_o}\right)^{2/3} \equiv b^2 \frac{\rho_o^{\ 2/3}}{N_o^{\ 2/3}} \tag{5-10}$$

with $b^2 = 1.70 \times 10^{-13} cm^2$. Substituting in Equation (5-8), dividing by $\rho_o^{\ 2/3} \pi b^2 v N_o^{\ 1/3}$ and using

$$\rho_o = \tau_o \left(g - \frac{n_{ex}}{\tau_{ex}}\right) \tag{5-11}$$

one gets:

$$0 = \frac{1}{\pi b^2 v \tau_o^{\ 2/3} N_o^{\ 1/3}} \left(g - \frac{n_{ex}}{\tau_{ex}}\right)^{1/3} + \frac{4A_r}{v} e^{-\phi/kT} - n_{ex}. \tag{5-12}$$

To fit the experiment, this equation was written as follows:

$$Be^{-\phi/kT} = n_{ex} - A\left(g - \frac{n_{ex}}{\tau_{ex}}\right)^{1/3} \tag{5-13}$$

with

$$A = \frac{1}{b^2 v \tau_o^{\ 2/3} N_o^{\ 1/3}} \tag{5-14}$$

$$B = \frac{4A_r}{v} \tag{5-15}$$

where A is a constant dependent on the excitation power and weakly on the temperature. For the actual fit, A was assumed constant for all temperatures. B is determined by the threshold temperature and exciton concentration, where $g = n_{ex}/\tau_{ex}$ as:

$$B = n_{ex}(T_h)\ e^{\phi/kT_h}. \tag{5-16}$$

As a consequence, B depended on the actual value of the work function.

5. Results and Discussion

The solid lines in Figure (5-6) are the fit of the Pokrovskii model with ϕ = 5 meV, and A = 4.20×10^7, 3.77×10^7 and 5.10×10^7 cm^3. These values correspond to excitation powers of 60, 120 and 240 mW respectively. The fit was done by estimating the first value of ϕ from the slope of a straight line passing through the experimental points at the threshold temperatures. This gave ϕ values in the range 4.6 to 6.8 meV. The uncertainty came from the difficulty in determining the threshold temperatures from Figure (5-6). The resulting range of A served as a first estimate of this parameter. Then ϕ and A were systematically varied and the best fit was determined by inspection. The fit was very sensitive to the value of ϕ and the best fits were obtained with 5 meV.

This value of the work function is 60% of the spectroscopic value of $\phi = 8.2 \pm 0.2$ meV (Hammond, McGill and Mayer, 1976) obtained from luminescence measurement. A similar situation exists for the condensation energy of excitons in Ge where several different onset or thermodynamic types of experiments have given values for ϕ that are on the average 65% of the value obtained from spectroscopic experiments. The work function is expected to be a function of the radius of the drops and the temperature. The dependence with respect to the radius can be studied as follows: the energy required to evaporate a drop of radius R of ν particles is:

Figure 5-6

Observed exciton concentrations at different temperatures in silicon. The decreasing concentrations at lower temperatures are an indication of the condensation of excitons into EHD. The solid lines are the fit of the Pokrovskii's model as discussed in the text.

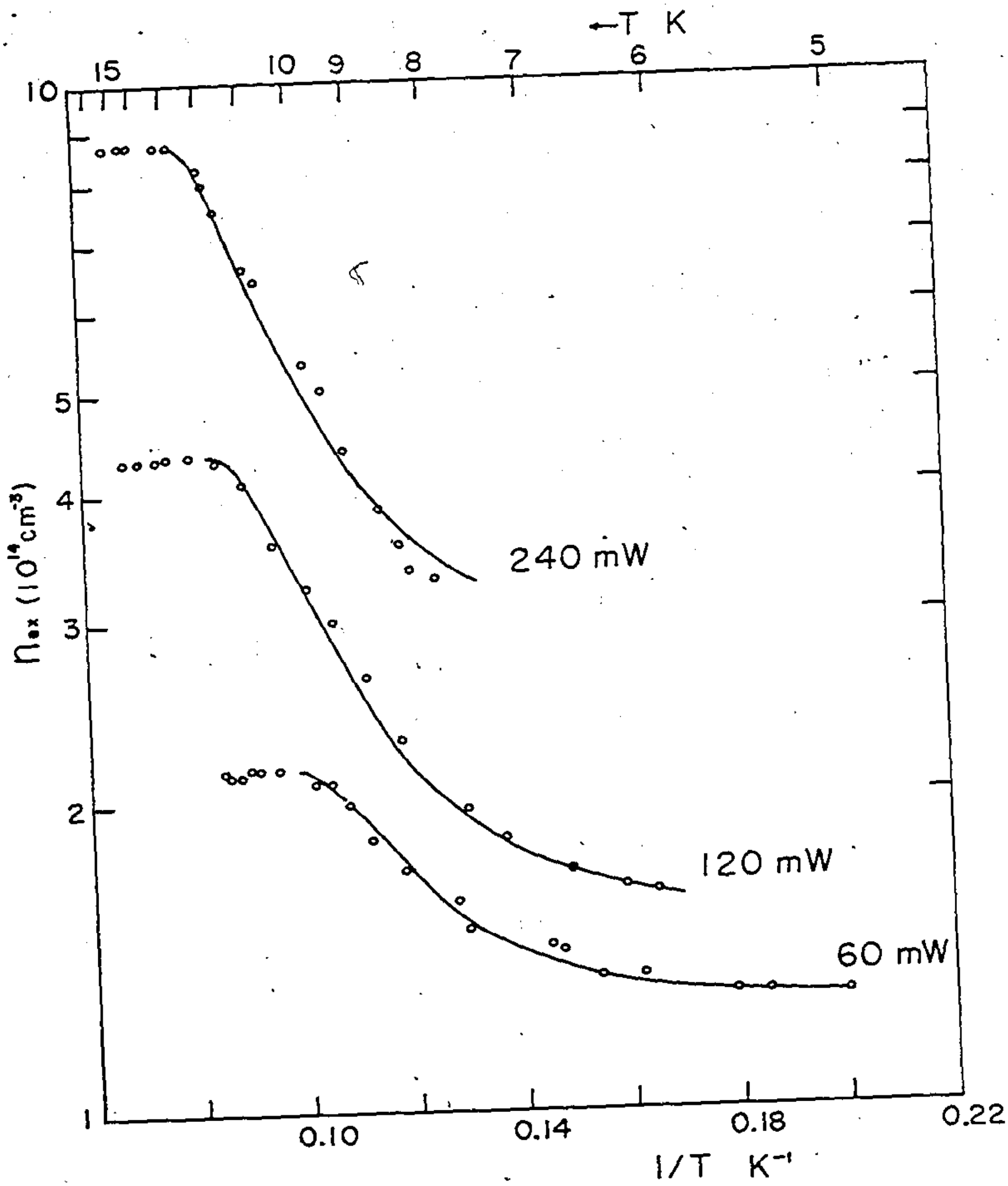
←T K
15
10
9
8
7
6
5
10
5
4
3
2
1
n_{ex} ($10^{14}cm^{-3}$)
240 mW
120 mW
60 mW
0.10
0.14
0.18
0.22
1/T K⁻¹

$$\Phi(\nu) = \nu\phi - 4\pi R^2\sigma \tag{5-17}$$

where σ is the surface energy and ϕ here represents the condensation energy for a drop of infinite radius. Differentiating with respect to ν to obtain $\phi(R)$ the condensation energy for one exciton:

$$\phi(R) = \phi - 4\pi\sigma\frac{dR^2}{d\nu} \tag{5-18}$$

and using

$$\nu = \frac{4\pi}{3} R^3 n_o$$

one gets:

$$\phi(R) = \phi - \frac{2\sigma}{Rn_o} . \tag{5-19}$$

The value of σ has been measured recently as $\sigma = 125 \times 10^{-4}$ erg/cm^2 by Collet et al (1977). Using $R = 0.3$ µm as a typical radius as obtained below, this correction amounts to only 0.15 meV. Hence, it is not possible to attribute most of the difference to the small size of the drops in silicon. Recent work on nucleation theory (Westervelt 1979) seems to resolve these discrepancies.

The values of A obtained from the fit can be used with Equation (5-14) to estimate N_o, the concentration of drops per unit volume. From Dite et al (1974) $\tau_o = 1.5 \times 10^{-7}$ sec and hence, the values estimated for N_o are of the order of 1.2×10^7 to 3.0×10^7 drops per cm^3. This number for N_o was checked using Equation (5-6) for $R = 0.3$ µm corresponding from Figure (5-7) to 12K with an excitation power of 240 mW. In these conditions, it was determined that 15% of the electron-hole pairs generated are condensed eventually into EHD.

The radius of the drops at a given excitation power and temperature can also be obtained from the experimental points of Figure (5-6) and the Pokrovskii's Equations (5-6) and (5-7). From these two equations, it follows that:

$$R = \frac{3v\tau_o}{4n_o}(n_{ex} - Be^{-\phi/kT}) \tag{5-20}$$

Here, $n_o = 3.4 \times 10^{18}$ cm^3 and $v = 1.78 \times 10^6\sqrt{T}$. Figure (5-7) shows the calculated values of R using this equation for the different excitation powers. The values obtained for the radius compare very favorably with those obtained by Capizzi et al (1975), R = 0.75 μm, and the estimate of Hensel et al (1976), R $\sim$ 0.1 μm.

The observed temperature dependence of the radius is in good qualitative agreement with that expected from homogeneus nucleation theory (Westervelt et al, 1975). From this theory, it is known that the embryos need to achieve a minimum radius to be able to grow into a stable drop. This radius is an increasing function of the temperature for a given excitation (supersaturation) power. However, when the recombination rate of electron hole pairs inside the drops is added to the classical rate equations, as this term increases as R^3 while the capture or emission of drops increases as R^2, there is a maximum possible value for the radius. For further increments of T, the evaporation and recombination start to overcome the capture rate and the stable radius starts to decrease in size.

As a conclusion to these last three sections of the chapter, it can be said that the Pokrovskii model provides an adequate description of the observed exciton concentrations. At lower temperatures, as suggested by the results for the excitation power of 240 meV, the Pokrovskii model might not be adequate to predict the behaviour of the exciton gas in coexistence with the drops of electron-hold fluid. Typical sizes of EHD in silicon obtained varied around 0.1 to 0.6 μm, and the drop concentration is of the order of 10^7 drops per cubic centimeter.

Figure 5-7

Estimated radius of the electron-hole drops in silicon. The estimate was done using the experimental points presented in Figure 5-6 and Equation (5-17) obtained from Pokrovskii's model.

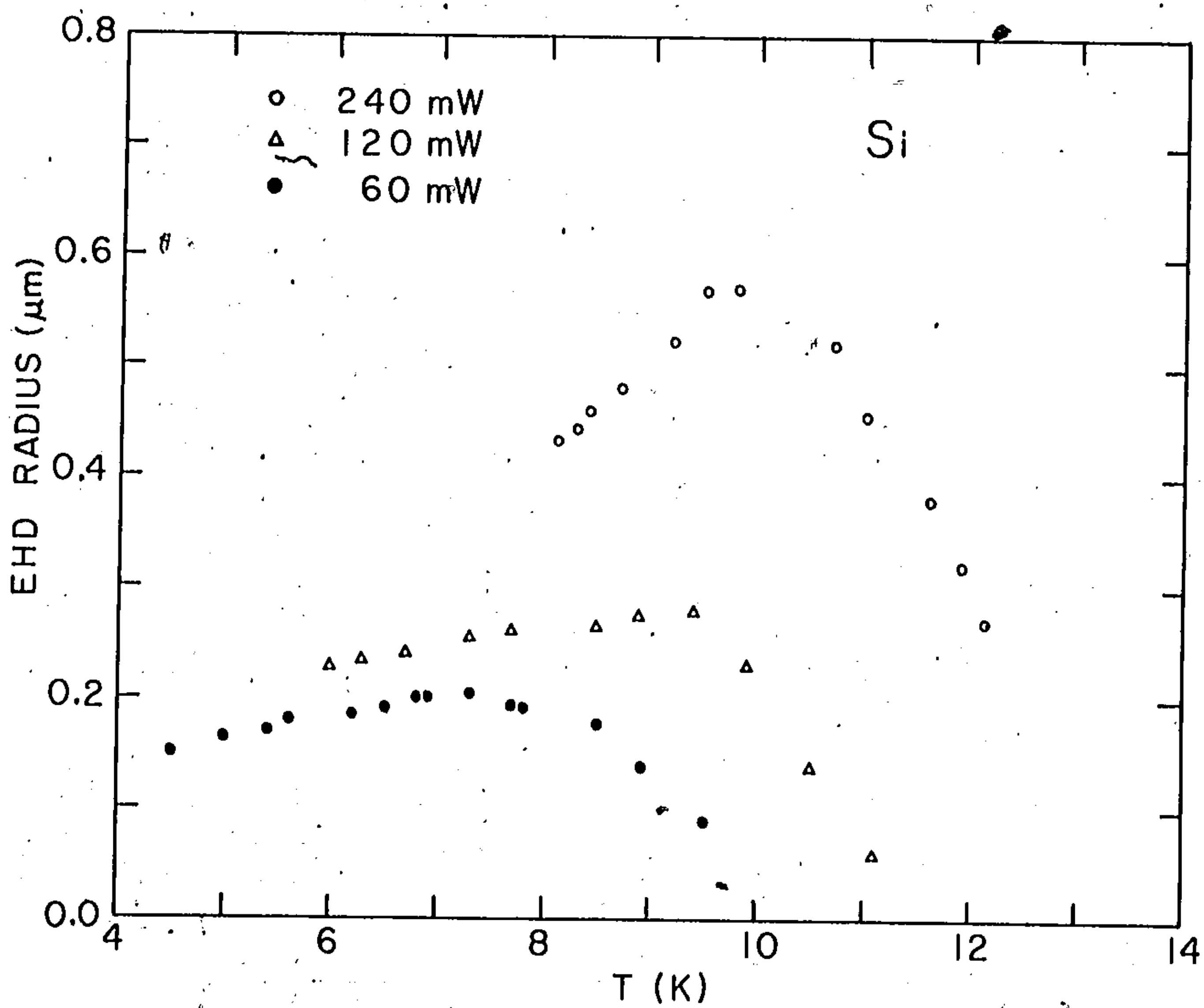

0.8
0.6
0.4
0.2
0.0
EHD RADIUS (μm)
4
6
8
10
12
14
T (K)
240 mW
120 mW
60 mW
Si

CHAPTER VI

FAR INFRARED ABSORPTION BY ELECTRON-HOLE DROPS IN SILICON

1. Introduction

In silicon the electron-hole drops, (EHD) are condensed in small drops of radius R typically of the order 0.2 μm as obtained in the previous chapter. The corresponding absorption spectrum is expected to be in the spectral region between 5 and 50 meV, which corresponds to wavelengths of 250 to 25 μm. The problem of the attenuation of radiation by small metallic drops can be described by the Mie expansion for the scattering and absorption coefficients (M. Kerker 1969). The Mie theory is applicable for small drops that satisfy the relation $R \ll \lambda/\sqrt{\varepsilon_0}$, where λ is the wavelength of the radiation incident and ε_0 is the dielectric constant of the medium in which the drops are embedded. For silicon, using $\varepsilon_0 = 11.4$ the inequality restricts the application of the Mie expansion to drops with radius $R < 0.75$ μm for the spectral region under consideration. This condition is very well satisfied for the EHD in this material. As a result the first term of the Mie expansion provides an adequate approximation for the absorption coefficient, because the following terms involve at least an extra factor of $(\varepsilon_0^{1/2}R/\lambda)^2 \ll 1$.

The Mie expansion expresses the absorption coefficient as a function of the dielectric constant of the absorbing drops at the frequency of the incident radiation. Therefore it is necessary to discuss and include all the mechanisms that contribute to the dielectric constant of the EHD. A theoretical fit to the observed experiment will provide a value for the plasma frequency of the EHD and from it, an estimate of the electron-hole pairs density inside the drops can be obtained. In sec. 2 of this chapter the theory of the absorption of radiation by the EHD is discussed in some detail. In sec. 3 the experimentally observed spectra are presented while in the last section the fit of the theory to experiment is discussed.

2. Theory of absorption of radiation by EHD

The complex refractive index of a material is given by:

$$N(\omega) = n(\omega) + iK(\omega) \equiv \sqrt{\varepsilon(\omega)} \tag{6.1}$$

where $n(\omega)$ is the refractive index and $K(\omega)$ is the extinction coefficient of electromagnetic waves of the material. The absorption coefficient, the fraction of energy absorbed in passing through unit thickness of the material is given by:

$$\alpha(\omega) = \frac{2K(\omega)\omega}{c} \tag{6.2}$$

or from eq. (6.1)

$$\alpha(\omega) = \frac{2\omega}{c} \operatorname{Im}(\varepsilon(\omega)^{1/2}) . \qquad (6.3)$$

Thus it is necessary to know the contribution to the total dielectric constant produced by the cloud of EHD in the material.

Consider the drops as noninteracting metallic spheres of radius R and dielectric constant ε. In a uniform electric field $\vec{E}$, each sphere contributes a polarization,

$$\vec{P} = \frac{\varepsilon-\varepsilon_0}{\varepsilon+2\varepsilon_0} \varepsilon_0 R^3 \vec{E} . \qquad (6.4)$$

Adding this polarization to that of the crystal leads to an effective dielectric constant of the system given by:

$$\varepsilon_{eff} = \varepsilon_0 [1 + 4\pi N_0 R^3 \frac{\varepsilon-\varepsilon_0}{\varepsilon+2\varepsilon_0}] \qquad (6.5)$$

where N_0 is the number of drops per unit volume. This dipolar approximation is valid in the case in which the radius of the drop is so small compared with the effective wavelength of the radiation in the crystal, $\lambda/\sqrt{\varepsilon_0}$, that the field is essentially uniform throughout the drop at a given time. For EHD in silicon $N_0 \sim 10^7/\text{cm}^{-3}$, $R \sim 10^{-5}$ cm, and $(N_0 R^3)$ is smaller than unity. Then to get the absorption coefficient it is possible to use the first term involving $N_0 R^3$ in the binomial expansion for $\varepsilon_{eff}^{1/2}$. In this case the absorption coefficient can be written as

$$\alpha(\omega) = \frac{4\pi\omega}{c} N_0 R^3 \sqrt{\varepsilon_0}\ \mathrm{Im}\left(\frac{\varepsilon-\varepsilon_0}{\varepsilon+2\varepsilon_0}\right) . \qquad (6.6)$$

This dipolar contribution is equivalent to keeping only the first term in the Mie expansion.

In order to evaluate the absorption coefficient (6.6) it remains to calculate the dielectric constant that describes the response of the metallic drops to the incident radiation. Murzin, (1973), Murzin et al. (1975), and independently Rose, Shore and Rice (1975) have considered the mechanism for absorption by the drops to be the excitation of damped plasma oscillations of the electrons and holes, along with interband transitions between the hole bands, with energies in the region considered.

In the general case the frequency and wave-vector dependent dielectric constant of a semiconductor within the random phase approximation is given by (Ehrenreich and Cohen 1959):

$$\varepsilon(q,\omega) = \varepsilon_0 - \frac{4\pi e^2}{q^2} \sum_{\vec{k}} \sum_{ij} \frac{(f^i_{\underline{k}} - f^j_{\underline{k}})(E^i_{\underline{k}} - E^j_{\underline{k}+\underline{q}})}{(E^i_{\underline{k}} - E^j_{\underline{k}+\underline{q}})^2 - (\omega+i\gamma)^2} \left|\rho^{ij}_{\underline{q}}\right|^2 \qquad (6.7)$$

Here the indices i, j are summed over $\vec{k}$ states in the different bands; $\rho^{ij}_{\underline{q}}$ denotes the matrix element of the density operator, between the state $\underline{k}$ in the ith band and the state $\underline{k}+\underline{q}$ of the jth band; $f^i_{\underline{k}}$ and $f^j_{\underline{k}+\underline{q}}$ are the thermal occupation factors of these states. Strictly speaking this expression for $\varepsilon(\underline{q},\omega)$ is valid for infinitesimal values of γ only, but it has been customary to assume that the expression holds even for the more realistic cases in which the damping constants have finite values. The summation over the bands can be divided into two parts. The first part contains those transitions in which the initial and final state $\vec{k}, \vec{k}+\vec{q}$ are in the same band. These are called intraband transitions. The second part consists of transitions in which the initial and final state are in different bands. These are called interband transitions. Thus,

$$\varepsilon(\underline{q},\omega) = \varepsilon_0 + \varepsilon_{intra} + \varepsilon_{inter} \quad (6.8)$$

The $\underline{q}$ vector is provided by the incident radiation and is very small when compared with the $\underline{k}$ vectors of the electron and hole states. In this limit of small $\vec{q}$ the energy difference between two states in the same band is negligible compared with the term $(\omega+i\gamma)^2$ in the denominator. In this case the contribution of intraband transitions to the dielectric constant is the Drude expression

$$\varepsilon_{intra} = -\frac{\varepsilon_0 \omega_p^2}{\omega(\omega+i\gamma)} \quad (6.9)$$

where following general use we have put $\gamma = 2\gamma_d$. In this expression one has to include the intraband transitions in the electron, heavy hole and light hole bands. Here ω_p^2 is the plasma frequency which in the spherical approximation for the hole bands is given by:

$$\omega_p^2 = \frac{4\pi e^2}{\varepsilon_0}\left(\frac{n_e}{m_{oe}} + \frac{n_1}{m_1} + \frac{n_2}{m_2}\right) \quad (6.10)$$

where n_e, n_1 and n_2 are the density of electrons, heavy holes and light holes inside the drop, m_{oe}, m_1 and m_2 are the optical masses of the electron, heavy hole and light hole, respectively. In the spherical approximation for the hole bands the relative concentration of the two types of holes are in the ratio

$$\frac{n_2}{n_1} = \left(\frac{m_{\ell h}}{m_{hh}}\right)^{3/2} \equiv \rho^{3/2} \qquad (6.11)$$

where $m_{\ell h}$ and m_{hh} are the density-of-states masses of the light and heavy holes respectively. Using the fact that the concentration of holes is equal to the concentration of electrons inside the drop, i.e. $n_1+n_2 = n_e \equiv n_0$ we can write the expression for the plasma frequency as

$$\omega_p^2 = \frac{4\pi e^2}{\varepsilon_0} n_0 \left(\frac{1}{m_{oe}} + \frac{1}{m_1}\frac{1}{1+\rho^{3/2}} + \frac{1}{m_2}\frac{\rho^{3/2}}{1+\rho^{3/2}}\right) . \qquad (6.12)$$

The density-of-states masses of the electron and the two holes are given for silicon in table 3-1 where the optical mass of the electron is also given. The optical masses of the heavy and light holes can be calculated in the spherical approximation used by Murzin et al (1975): $m_{1,2} = m_o/A\mp\sqrt{B^2 + \frac{C^2}{5}}$. This formula gives $m_1 = 0.462\ m_o$ and $m_2 = 0.156\ m_o$ for Si. Murzin et al. also calculated numerically these masses using the actual band structure for Ge and found no change to the light-hole optical mass and a 20% difference for the heavy-hole optical mass. This is due to the fact that while the light-hole band is almost spherical the heavy-hole band has considerable cubic warping. The situation is similar for the hole bands in silicon.

For the calculation of the interband contribution it is necessary to introduce an interband damping constant called γ_2 different from the Drude damping constant. The interband matrix elements of the density operator have been evaluated in the spherical approximation between the two hole bands by Combescot and Nozières (1972). For small q values:

$$|\rho_{\underline{q}}^{ij}|^2 = \frac{3}{4}\sin^2(\vec{k},\vec{k}+\vec{q}) = \frac{3}{4}\frac{q^2}{k^2}\sin^2\alpha \qquad (6.13)$$

where $(\vec{k},\vec{k}+\vec{q})$ represents the angle between the vectors $\vec{k}$ and $\vec{k}+\vec{q}$. The equation (6.7) for ε_{inter} can be expressed in integral form using spherical coordinates for the quasimomentum $\underline{k}$ in the form:

$$\varepsilon_{inter}(\omega) = -4\pi e^2\varepsilon_0 \int_k \int_0^{2\pi} \int_0^{\pi} \frac{f_{1(k)}-f_{2(k)})(E_{1k}-E_{2k})}{(E_{1k}-E_{2k})^2-(\omega+i\gamma)^2} \frac{2\sin\theta}{(2\pi)^3}\, d\theta d\phi dk \quad (6.14)$$

As $\vec{q}$ can make any angle α with $\vec{k}$, the angular average of $<\sin^2\alpha> = \frac{2}{3}$ over a sphere has been used in arriving at (6.14).

When the actual energy expressions (3.1) are used for the hole bands, the interband contribution to $\varepsilon(\underline{q},\omega)$ cannot be expressed in analytical form. This contribution was computed numerically and represented by

$$\varepsilon_{inter} = \varepsilon_1 + i\varepsilon_2 \ . \tag{6.15}$$

Figure 6-1 shows the real and imaginary parts of the interband dielectric constant calculated with the Fermi energy for the holes of Hammond, McGill and Mayer (1976) and the value of γ_2 = 12 meV used to fit the experimental data discussed in the next section.

Finally the total dielectric constant for the EHD can be written

$$\varepsilon(\omega) = \varepsilon_0 - \varepsilon_0 \frac{\omega_p^2}{\omega(\omega+i\gamma)} + \varepsilon_1 + i\varepsilon_2 \ . \tag{6.16}$$

Hence from Eq. (6.6) the absorption constant is

$$\alpha(\omega) = \frac{4\pi\omega}{c} \sqrt{\varepsilon_0}\, N_d R^3 \frac{\varepsilon_2'(\gamma^2\omega^2+\omega^4) \mp \gamma\omega\omega_0^2}{[\omega_0^2-\varepsilon_1'\omega^2+\varepsilon_2'\gamma\omega-\omega^2]^2+[\gamma\omega+\varepsilon_1'\gamma\omega+\varepsilon_2'\omega^2]^2} \tag{6.17}$$

where $\varepsilon_1' = \varepsilon_1/3$, $\varepsilon_2' = \varepsilon_2/3$ and $\omega_0^2 = \omega_p^2/3$.

3. Experimental Results

Vertical interband transitions are possible for photon energies between two limits, $h\nu_1$, and $h\nu_2$, determined by the Fermi energy of the holes and the structure of the two hole bands. The direction <100> gives the minimum possible value for $h\nu_1$, and the maximum value $h\nu_2$ is along the <111> direction, as can be checked using the energy expression (3.1) for the hole bands. It is schematically illustrated in figure 6-2. In

123-6

Figure 6-1

Real and imaginary parts of $\bar{\varepsilon} = \varepsilon/\varepsilon_0$, the calculated interband dielectric constant divided by ε_0. The interband damping constant used is $\gamma_2 = 12$ meV. The effect of this high value of the damping is to broaden considerably both parts of the dielectric constant compared with calculations for small γ_2.

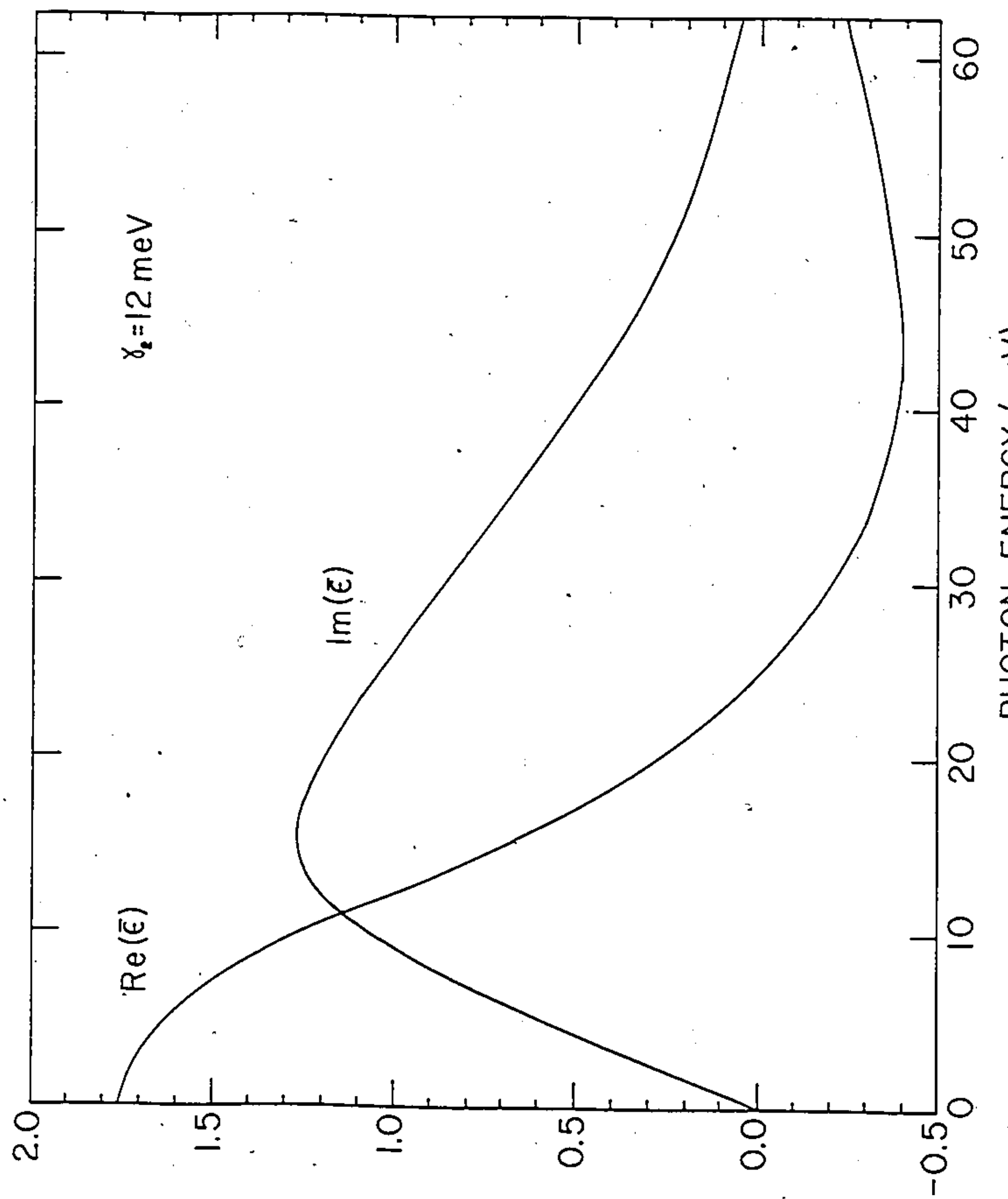

γ_2=12 meV
Re($\bar{\epsilon}$)
Im($\bar{\epsilon}$)
2.0
1.5
1.0
0.5
0.0
-0.5
0
10
20
30
40
50
60
PHOTON ENERGY (meV)

Figure 6-2

Schematic drawing of the allowed interband transitions that contribute to the EHD absorption. E is the hole energy, E_F is the Fermi energy (14.4 meV for the EHD in silicon), $\hbar\omega_1$ is the energy threshold for the transitions and $\hbar\omega_2$ is the highest possible energy for the transitions.

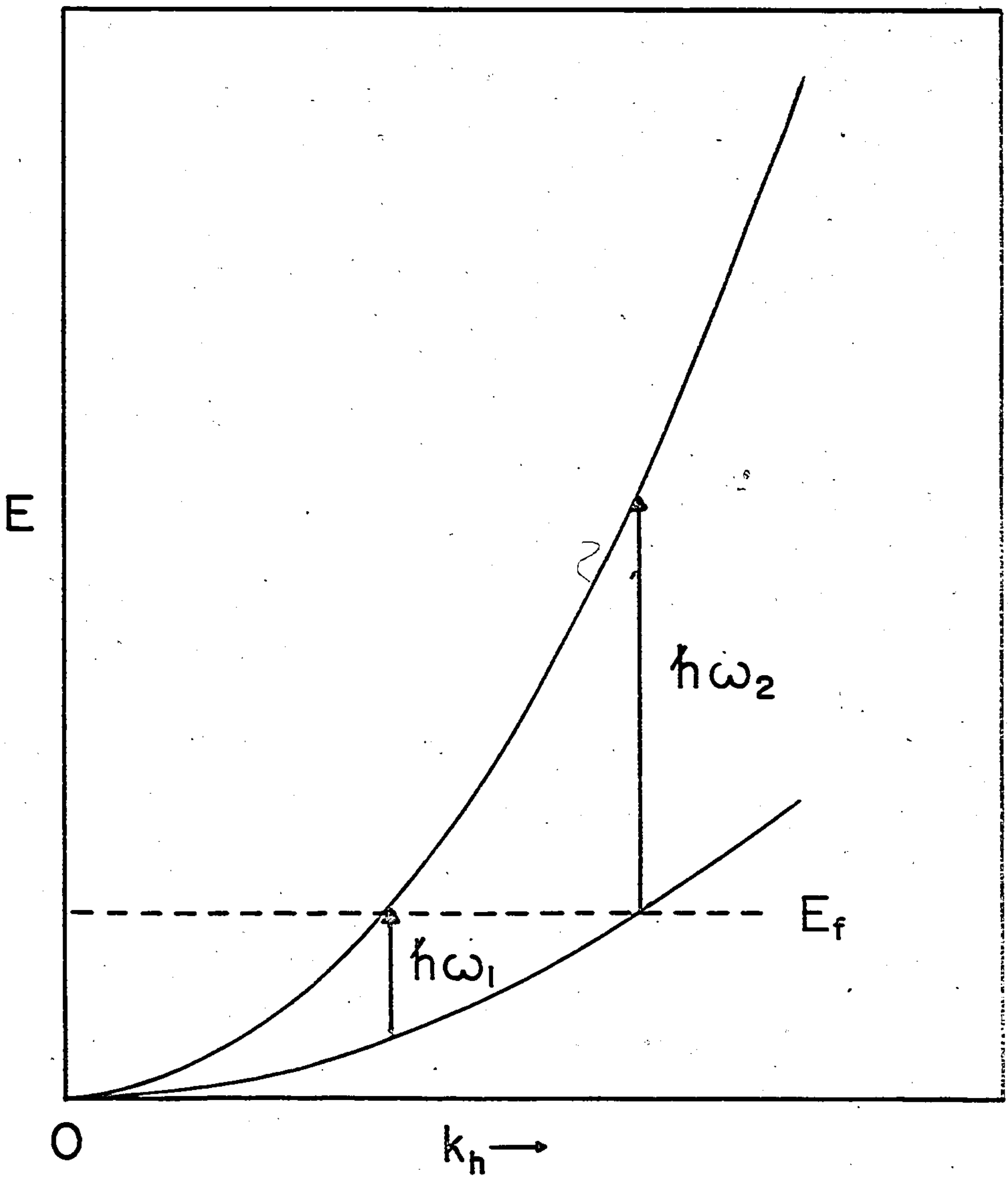
E
$\hbar\omega_2$
E_f
$\hbar\omega_1$
O
$k_h \longrightarrow$

silicon the Fermi energy of the holes at $T = 0$ K is given by Hammond et al. (1976) as $E_{fh} = 14.4$ meV. With this Fermi energy the values obtained for the spectral limits are 3.97 and 60.04 meV for the interband contribution to the EHD absorption. From the same work of Hammond et al. $n_0 = 3.3\times10^{18}$ cm^{-3} at $T = 0$ K for silicon. Then using the Drude resonant frequency $\omega_0 = \omega_p^2/3$ for the absorption coefficient (6.17), one finds that the maximum of the EHD absorption should be around 30 meV. These criteria determine the spectral region that has to be probed for the experimental observation of the EHD spectrum.

Figure 6-3 shows the measured absorption at 14 K and an incident excitation laser power of 360 mW in silicon, in the spectral region from 7 to 46 meV. Two distinctive features are apparent in this spectrum: the strong absorption centered at 11.5 meV and the broad absorption that peaks at 34.2 meV. The peak at 11.5 meV is due to free excitons and has already been discussed in chapter five. The broad peak is the resonance absorption due to the EHD drops. This identification is based on two points: first, its position corresponds to a plasma frequency that is consistent with the estimated value of the EHD density in silicon, and second, its temperature dependence agrees with the EHD model.

All reported temperatures have been corrected for heating due to the laser, using the exciton line width, which varies directly with temperature as discussed in chapter 5. The assumption is made that the drops and excitons are in thermal equi-

Figure 6-3

Absorption spectrum of excitons and EHD in silicon at 14 K and 360 mW. The peak at 11.5 meV is due to excitons. The broad absorption with maximum at 34.2 meV is the resonant absorption of the EHD. The dotted line shows the absorption due to transitions to the continuum from the different exciton states.

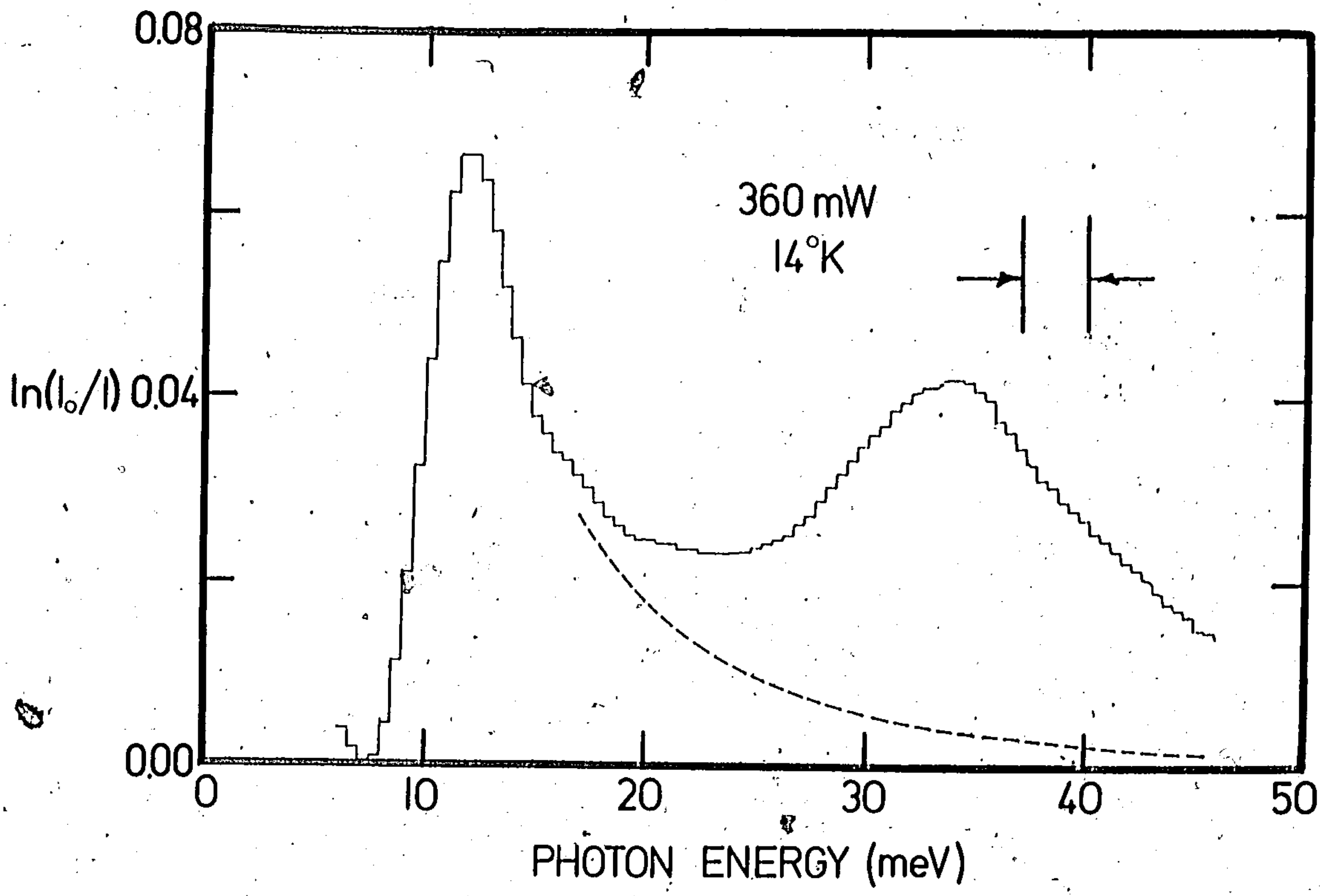
0.08
ln(I₀/I) 0.04
0.00
0
10
20
30
40
50
PHOTON ENERGY (meV)
360 mW
14°K

librium with each other. The corrections amount to 3 K and 4 K with 240 mW and 360 mW of excitation.

The temperature dependence of the 34 meV band is characteristic of the coexistence of the electron-hole fluid with the exciton gas. Fig. 6-4, 6-5 and 6-6 show the silicon absorption in the far infrared under an excitation power of 240 mW at three different temperatures. The EHD absorption is strongest at low temperatures and decreases as the temperature is raised to become unobservable about 20 K as shown in Fig. 6-6. At the same time a shift of the resonant frequency toward the low frequency region can be observed, characteristic of the decrease in density of the electron hole fluid with increasing temperature. In the same temperature range the exciton peak at 11.5 meV increases in strength up to 20 K and then remains constant at still higher temperatures. For experiments done at lower excitation levels, the saturation of the exciton absorption occurs at lower temperatures as illustrated in fig. (5-6). These phenomena were first observed in luminescence by Pokrovskii (1972) and are characteristic of a gas in equilibrium with a condensed phase.

To be able to compare with the theoretical expression for the absorption coefficient (6.6) or (6.17) it is necessary to obtain the actual EHD line shape from the experiment. From the spectrum of Figure 6-3 two corrections were made to get this line shape. First it is necessary to subtract the high-frequency

Figure 6-4

Absorption spectrum at 240 mW and 10 K of the excitons and EHD in silicon. Notice that the resonant EHD absorption has its peak at approximately 34.2 meV, the same value as at 360 mW and a temperature of 14 K.

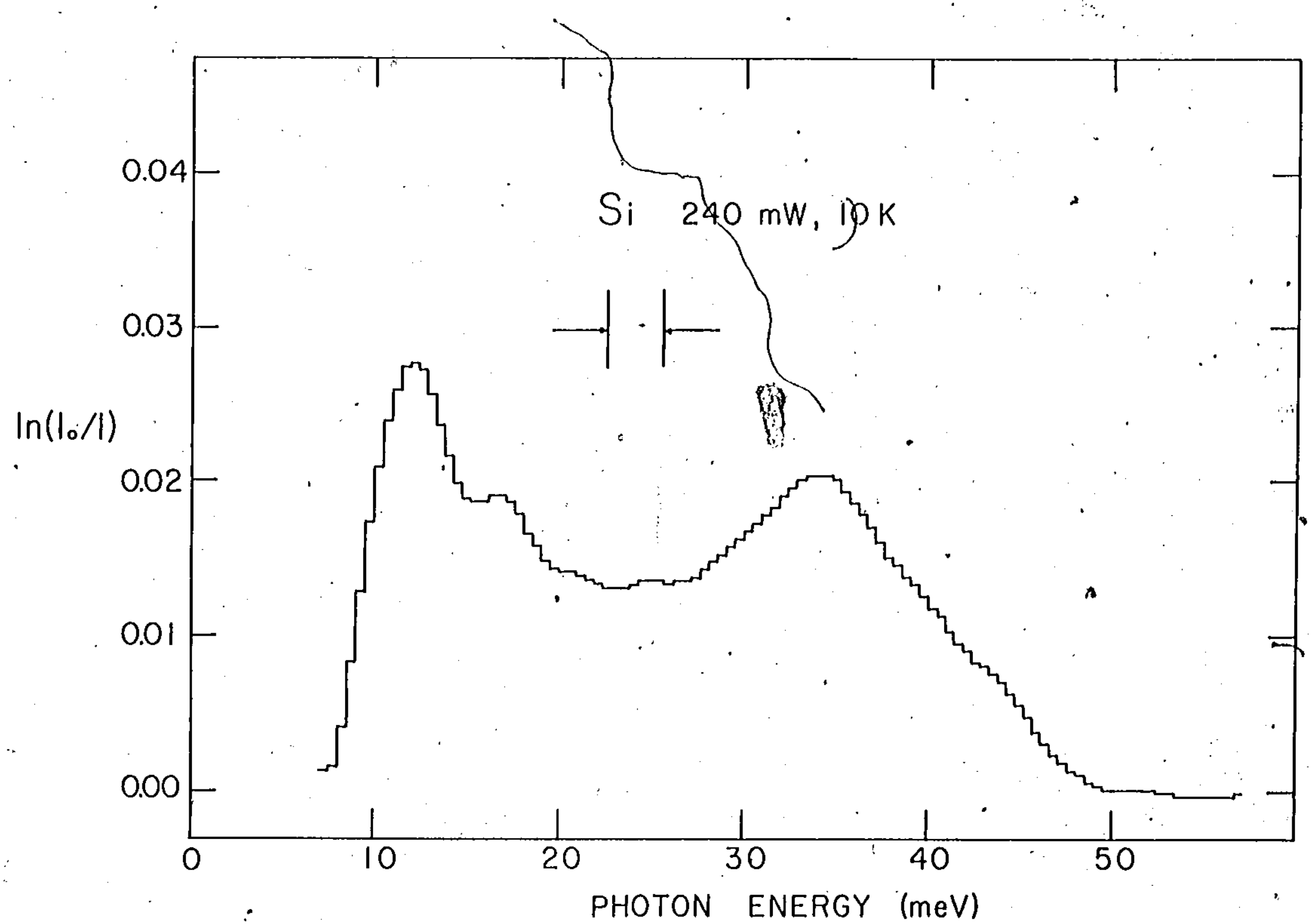
Si 240 mW, 10 K
0.04
0.03
0.02
0.01
0.00
ln(I₀/I)
0
10
20
30
40
50
PHOTON ENERGY (meV)

Figure 6-5

Absorption spectrum of the excitons and EHD at 240 mW and 13.5 K. The maximum of the resonant EHD absorption has decreased to a position of 33.1±0.2 meV, reflecting a decrease in e-h plasma density of the drop. At the same time the exciton peak at 11.5 meV has almost doubled in size while the EHD absorption has noticeably decreased.

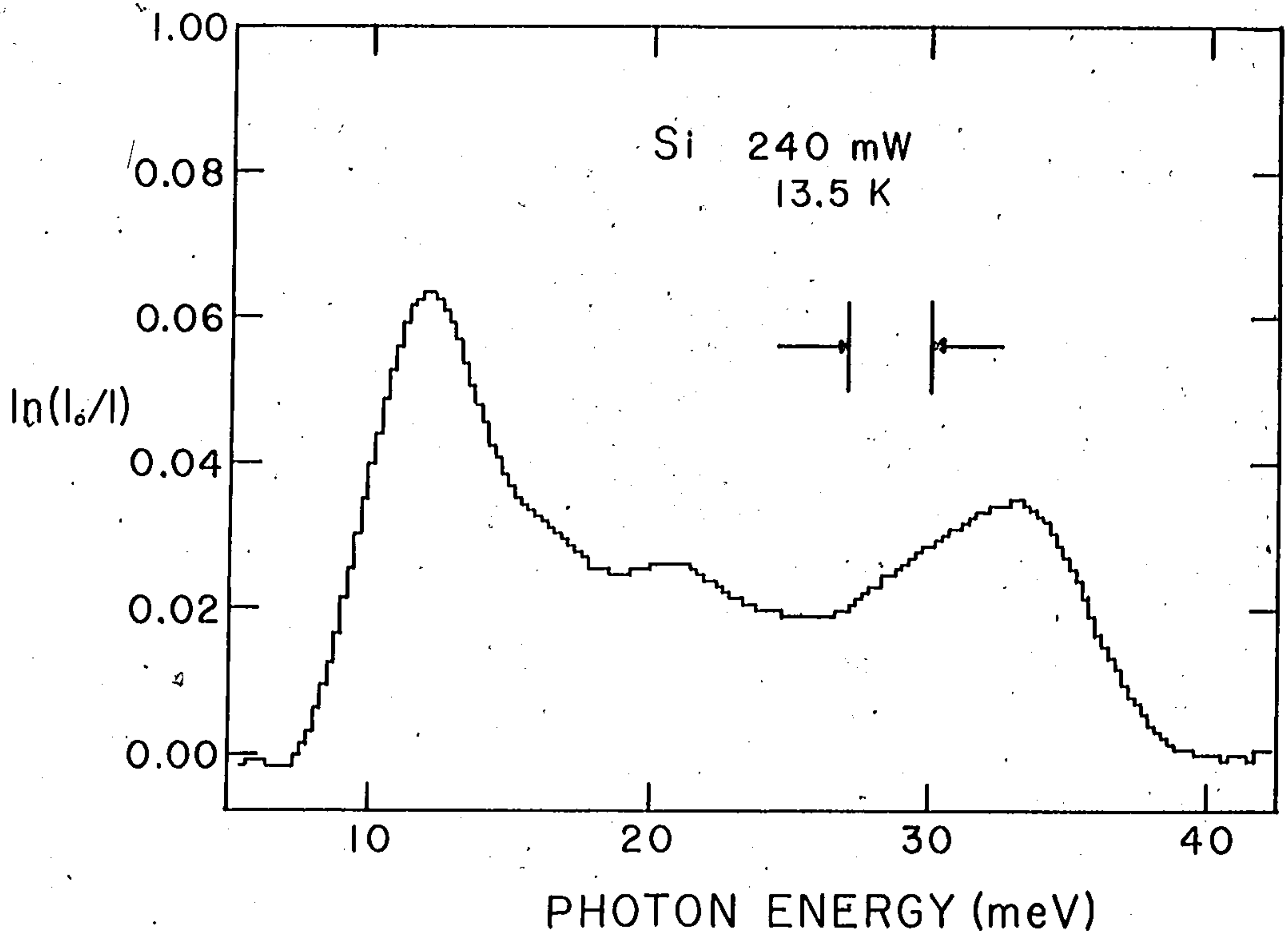
Si 240 mW
13.5 K
ln(I₀/I)
1.00
0.08
0.06
0.04
0.02
0.00
10
20
30
40
PHOTON ENERGY (meV)

Figure 6-6

Exciton absorption spectrum at 240 mW and 23 K in silicon, showing the 11.5 meV peak and the absorption due to transitions to the continuum. The drops have evaporated at this temperature.

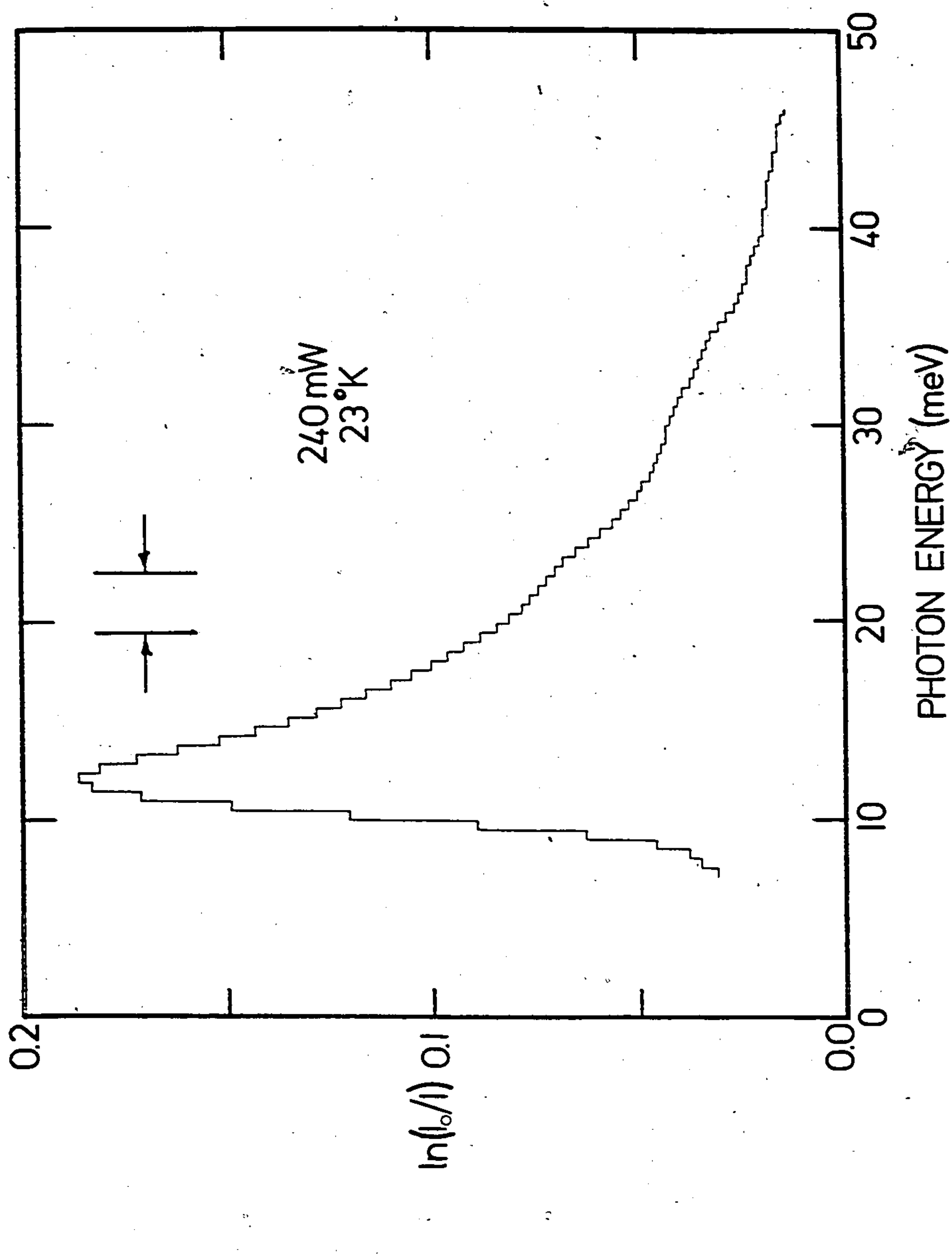
240 mW
23°K
PHOTON ENERGY (meV)
ln(I₀/I)
0.0
0.1
0.2
0
10
20
30
40
50

tail of the exciton absorption. Secondly one must allow for the slight base-line shift due to nonlinearities of the Ge bolometer used as a detector. To make the first correction the high-frequency tail of the exciton at 23 K of figure 6-6 has been studied. At this high temperature the exciton absorption has become constant, a sign that all the drops have evaporated and indeed the band at 34 meV is absent. It has been found that the exciton absorption constant $\alpha_{ex}(\omega)$ can be well described by a relation of the form $\alpha \sim \omega^{-\beta}$ with $\beta \simeq 2.5$ for frequencies in this tail. A very similar relationship holds for the photoionization of excitons in germanium (Buchanan and Timusk 1976) while for parabolic bands in a hydrogenic model an index $\beta = -8/3$ is expected (Bethe and Salpeter 1957). The dashed line shown in Fig. 6-3 was obtained by such an extrapolation.

To estimate the shift of the baseline, the adopted method was to assume a constant line shape for the exciton peak at various levels of excitation. When the drops had evaporated it was found that at the resolution used, the intensity of the point at 15 meV was always very close to 60% of the peak at 11.5 meV. For figure (6-3) this base line correction was -0.004 and for the curve at 23°K in fig. (6-6) it was -0.006 units of $\ln(I_0/I)$.

Fig. (6-7) shows the absorption of the EHD in silicon at 14K with the exciton tail removed. The points are the corrected experimental values. The uncertainties due to the two corrections mentioned above are the largest contributions to the

Figure 6-7

Absorption due to electron hole drops at 360 mW and 14 K, obtained from Fig. 6-3. The points represent the corrected experiment as described in the text, and the solid line is the fit of the theory.

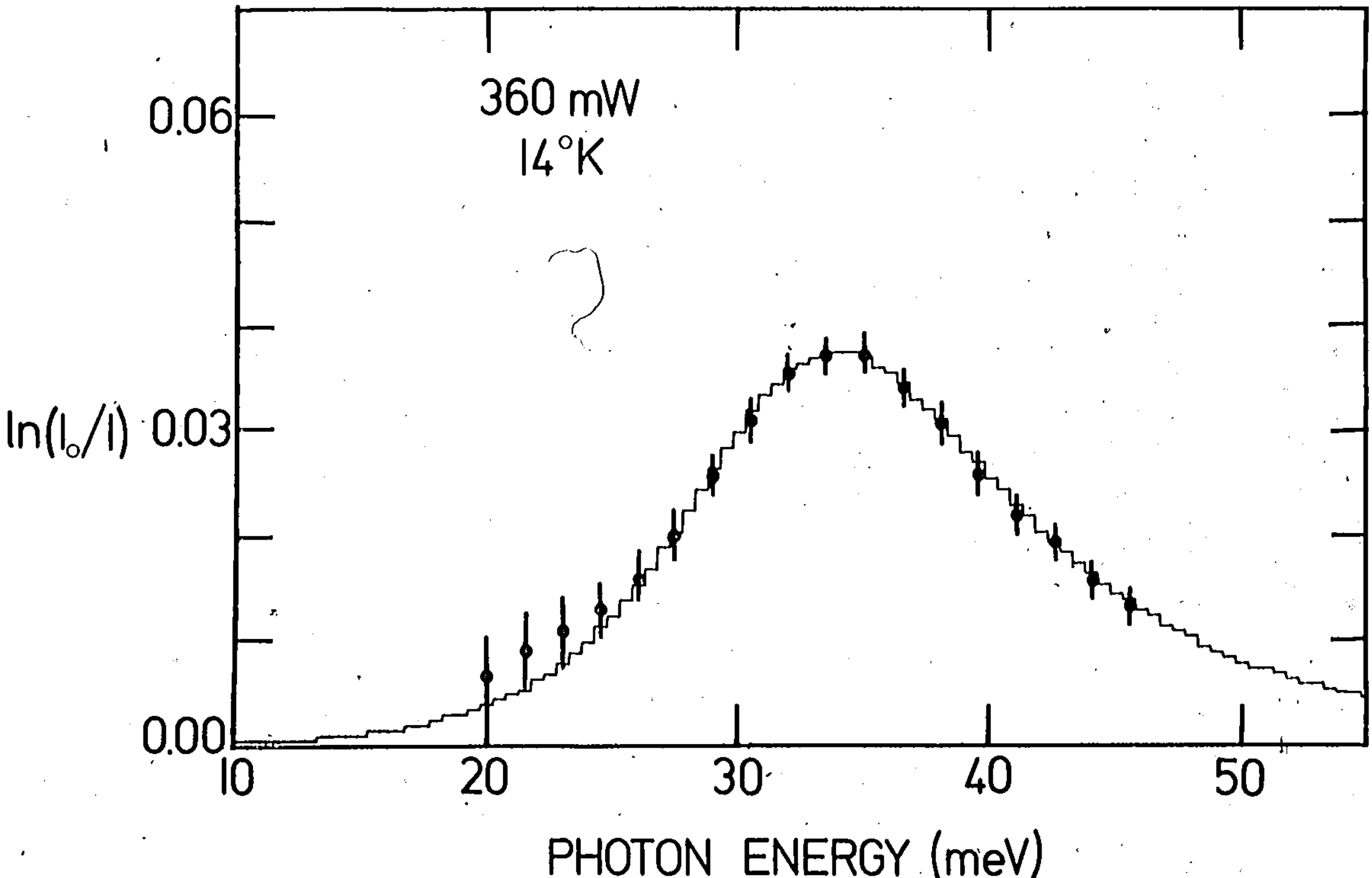

1326

error bars, particularly at lower frequencies where the exciton absorption is strongest. Any errors arising from these corrections, however, have little effect on the position of the maximum of the curve. The stepped line in the figure is the fit of the theory. In the calculations for $\alpha(\omega)$ the parameters ω_p, γ and γ_2 were varied to fit the experimental points. The best combination of these parameters was $\omega_p = 51.9\pm0.4$ meV, $\gamma = 4.2\pm0.8$ meV and $\gamma_2 = 12\pm2$ meV.

The calculated line shape is seen to be in good agreement with experiment. When doing the fit it was found that the position of the resonant frequency depends almost exclusively on the value of the plasma frequency ω_p and to a very minor extent (less than 1%) on the values of γ and γ_2. The width of the curve depends on both γ and γ_2, but by trial and error it was found that the most important contribution comes from the value of γ as can be guessed from eq. (6-17). In doing the fit first the values of ω_p and γ were varied, and then the value of γ_2 was varied to improve the fit.

Using the value of ω_p obtained from the fit and eq. (6-12). The density of electron-hole pairs at 14 K, inside the drop, was calculated to be $n_0 = (3.37\pm0.27)\times10^{18}\,cm^{-3}$. Allowance was made for the 20% uncertainty in the heavy-hole optical mass. This value is in good agreement with theoretical estimates for the EHD, as shown in table 6-1, but it is somewhat larger than the result of Hammond et al (1976), although the regions of uncertainty in both experimental results overlap.

As discussed by Murzin et al (1975) and Hensel, Phillips and Thomas (1976), the main damping mechanism responsible for the intraband and interband transitions is electron-hole scattering. The strength of this scattering saturates at some energy larger than the Fermi energy of the holes at a value of $\gamma \sim 0.1E_{fh} = 1.4$ meV. Recently Zarate and Timusk (1979) have pointed out that for very small drops of electron-hole fluid, surface scattering has to play an important role, especially when $\tau_s = V_f/R$ is smaller than the scattering time due to electron-hole collisions. In silicon, using the mass of the heavy holes and R = 0.5 μm, as a typical radius expected for high excitation powers, $\gamma_s = 1/\tau_s \sim 2$ meV. The sum of the contributions of these two mechanisms gives a damping constant that is of the right magnitude for the Drude damping constant but somewhat smaller than the interband damping constant γ_2. Murzin et al (1975) have calculated for the EHD in Ge that the effect on their absorption of increasing the interband damping value is almost identical to the effect of raising the temperature of the drops. As suggested by these results of Murzin et al, the higher experimental value of γ_2 may be partially due to thermal broadening which is not explicitly taken into account in the calculation of ε_{inter} at T = 0 K.

Table 6-1

The electron-hole densities of drops in silicon.

	$n_o \times 10^{18}$ cm^{-3}
This work (14°K)	3.37 ± 0.27
Hammond and McGill (14°K)	3.04 ± 0.13
Pokrovskii[a)] (4.2°K)	3.7
Theoretical[b)] (0°K)	3.1 - 3.4

a) Pokrovskii (1972)

b) Hensen, Phillips and Thomas (1976)

An extra piece of information that can be obtained from the experiment and from eq. (6-17) is the value of $N_0R^3d = 1.7\times10^{-7}$ cm, obtained from the values of $\alpha(\omega)d = 0.03$ at $\omega = 34$ meV. For the radius of the EHD typical values will be around 0.5 μ from Chapter 5. Using the value of the exciton diffusion length d = 0.01 cm used by Dite et al (1976) for the EHD in equilibrium with the exciton gas and assuming that the drops are uniformly distributed spheres of radius R, the drop concentration is estimated to be $N_0 \sim 10^8$ drops/cm^3. The generation rate of electron-hole pairs can be used to check this value of N_0R^3d. If the fraction of the total number of e-h pairs that are eventually condensed into drops is represented by f, the following expression represents the total number of these pairs generated per unit time

$$fP = \frac{4\pi}{3} N_0 R^3 \frac{n_0}{\tau_0} V_0 \qquad (6.18)$$

where P is the generation rate of the electron-hole pairs produced by the laser, τ_0 is the lifetime of an e-h pair inside the drop, which for Si is equal to 1.5×10^{-7} sec. (Cuthbert 1970) and $n_0 = 3.37\times10^{18}$ cm^{-3}. For simplicity the volume occupied by the exciton gas was used, which in the last chapter was determined as $V = 2\pi r^2 d$, where r is the radius of the laser spot. Substituting these numbers we get a value on the right hand side of the equation which is 3.7 times higher than the calculated generation rate on the left hand side. As f cannot be greater than unity, this result suggests that the volume V_0 in which the drops are distributed might be as much as one order of magnitude smaller than the volume occupied by the exciton gas.

Before finishing this chapter there is an important point to discuss in reference to the EHD absorption spectrum in silicon. As discussed in chapter III, the valence band of this material is such that the split-off hole band is 44 meV below the two hole bands at $\vec{k} = \vec{0}$. Then it is necessary to study the possible contribution to the absorption by interband transitions from the two hole bands to this split-off band, called for short the s.o. band from here on. In the spherical approximation the allowed transition from the light hole band to the s.o. band will extend from 39 meV to 44 meV at 0° K. Transitions from the heavy-hole band will cover a range from 44 meV to 62 meV.

The dielectric constant for these transitions was calculated assuming that the angular average of the square of the dimensionless density matrix element (6-13) was given by

$$\left| \rho_{q}^{i,s.o.} \right|^2 = \frac{\eta^2 q^2}{k^2}$$

where i represents any of the two heavy or light hole bands, and η represents the strength of the coupling between the states in the two different bands. This matrix element is expressed in this way because when Ehrenreich and Cohen (1959) obtained the expression for the dielectric constant (6-7), they showed that for k small when compared with those k at the Brillouin zone boundary $\rho_{\underline{q}}^{i,s.o.} = \langle \vec{k}\ i | \vec{k} + \vec{q}\ j \rangle$ i.e. the matrix element at the density operator is equal to the coupling between states in the two different bands. This coupling is expected to be small between states in either the heavy or light-hole bands and states in the s.o. band. In the expansion in q of the squared matrix element (6.19) only the term in q^2 was kept because the dielectric constant (6-7) is calculated in the limit of very small q and the contribution of the whole sum in that equation is divided by q^2. Thus terms involving smaller powers of q cannot exist because they will give unphysically divergent contributions at all frequencies. Terms of higher order will give vanishing contributions in this limit. The dielectric constant for transitions to the s.o. band was calculated at values of $\gamma_{s.o} = 0.01$ and 12 meV. The real and imaginary parts of the calculated dielectric constants showed strong peak values at 44 meV and rapidly varying structure for Reε for frequencies around this value. Then if $\eta \sim 1$ the shape of the absorption given by the dipolar cross section (6.17) will be sharply modified with a strong peak at 44 meV, independent of the electron-hole density inside the drop, and higher in intensity than the maximum observed at 34.2 meV. Figure (6-4) shows the absorption spectrum of the excitons and the EHD in silicon at 10 K and 240 mW of excitation, in a spectral range that extends to 57 meV. The figures makes clear that there is no evidence for any secondary maximum at frequencies around 44 meV, and that at most there is a very weak bulging of the absorption barely visible between 42.5 and 46 meV. Then $\eta \lesssim 0.1$, because for smaller values of η the contribution of the s.o. band would be completely unobservable.

CHAPTER VII

CONCLUSIONS

In this thesis, the first experimental observation of the far infrared absorption spectrum of indirect excitons in silicon has been presented. By studying the temperature dependence of the exciton transitions, it has been possible to identify most of the 1S to 2P transitions. Overall, this spectrum shows a more hydrogenic nature than the spectrum for the excitons in germanium, as was predicted by LA. However, a comparison with those values predicted by LA for each individual transition, suggests that the exciton energy levels in silicon should be recalculated within their model, including more terms in the exciton wavefunctions. Their last recalculation of the ground state splitting for this exciton was done in this fashion. A better comparison with experiment could then be made and a theoretical identification of the observed transitions attempted.

The absorption spectrum of the indirect exciton in germanium has also been studied in this work. For most of the observed transitions for this exciton, there is good agreement with the results of LA. In particular, two new peaks have been observed that are also in positions predicted by LA's calculations. However, their model still does not provide an adequate characterization of the two strong lines at 2.87 and 3.03 meV. Also in these experiments, it was not possible to obtain a clear indication of the presence of the predicted 1S→2P transition line at 1.28 meV.

The response of this exciton spectrum to a small external magnetic field was also presented. A model was proposed to explain the observed response. The model included (in the magnetic Hamiltonian) the interaction of the exciton orbital angular momentum, the hole angular momentum and the electron spin with the magnetic field. Using this magnetic model and the theoretical identification of the 1S and 2P exciton states proposed by LA, a good fit was obtained for most of the observed transitions in the presence of the magnetic field. A precise identification within the LA's model of the nature of the strong transition line at 3.03 meV would be very helpful in further testing of the magnetic model and the general theoretical scheme of the exciton levels proposed by those two authors.

A study of the concentration of the exciton gas in coexistence with EHD in silicon was also presented in this work. It was found that Pokrovskii's model for the rate equations of the concentrations of the excitons and the electron-hole pairs inside the drops, agreed well with the observed temperature dependence of the exciton concentration. Within the framework of Pokrovskii's model, estimates for the drop radius were obtained. It was found that the drops in silicon are small with typical values for the radius between 0.2 to 0.6 μm.

The first experimental observation of the far infrared absorption of EHD in silicon has been reported in this thesis. It was found that the first term in the Mie expansion for the absorption coefficient of the drops was adequate to explain the line shape of the absorption. The dielectric constant used in the Mie expansion included (as the main contributing mechanisms) interband transitions between the valence bands, which are degenerate at $\vec{k} = \vec{0}$, along with damped plasma oscillations of the electron-hole fluid. The fit of the theory is good enough to allow an estimate of the electron-hole density inside the drops, independent of any previous experimental work on the subject. In the process of doing the fit, it was found that the position of the resonant maxima was almost entirely dependent on the plasma frequency of the drops, which in turn depends directly on the square root of the electron-hole density of the drops. This fact suggests that the far infrared absorption of the EHD would be very suitable for measuring the dependence of this density with temperature. This would check the high density boundary of the coexistence of the electron-hole fluid with the exciton gas in the phase diagram for silicon, constructed by Dite et al and Shah et al.

In stress experiments, a decrease of the electron-hole density in the drops is expected when the stress is applied in most crystallographic directions. The observation of the far infrared absorption by the EHD would be a very convenient method to monitor the change of this density with the applied stress. These experiments would help in understanding the modifications experienced by the absorption mechanisms, i.e., the interband transitions in the valence bands and the damped oscillations of the electron and holes in the drops, when the crystal is subject to stress.

In conclusion, the far infrared Fourier transform spectroscopy was found to be a very powerful technique for the study of the exciton absorption spectra in silicon and germanium, as well as that of the EHD in silicon. The information obtained by this technique would be complemented for the case of the exciton spectra in these materials by studying their far infrared emission spectra at high resolution. It is expected that these measurements would improve the experimental situation. In these experiments, some of the more troublesome sources of noise are absent. This is so because, in emission experiments, the only extra radiation present at the frequencies in consideration is the blackbody emission from the surroundings. Hence, apart from the intrinsic electronic noise of the equipment, the only extra source of noise would be fluctuations in the blackbody emission. The feasibility of these experiments has been established by Vavilov et al (1970), who detected the emitted far infrared radiation of the EHD in Ge, and by the observed far infrared emission of the excitons in silicon by Kobayaski and Narita (1976).

APPENDIX A

DESCRIPTION OF AN INTERFACE TO THE MINICOMPUTER

1. The Stepping Motor Interface

The interface allows the NOVA 2 minicomputer control of a stepping motor. This motor drives the movable mirror of the Michelson interferometer, or the piston which carries half of the strip mirrors that form the grating in a Lamellar grating interferometer (R. Bell, 1972).

The logic circuit of the interface is shown in fig. A-1. It consists of three main units: The clock unit that provides pulses at a frequency of 312 Hz, the counter unit, that receives the number of steps to be performed, and the flag unit. The flag unit sets flag flip flops that the minicomputer uses to determine whether the interface is busy driving the motor or if it is clear to receive more steps to perform.

The clock unit consists of a crystal oscillator (Connor-Winfield Co. 1C5NL) of frequency 153.6 KHz, and TTL logic gates that divide this frequency down to 312 Hz. The counter unit consists of two TTL binary counters (SN 74161) that count up to 255 steps and of several gates that decode the signals sent by the computer and a couple of pnp transistors (2N3638) that amplify the inverted step pulses to -20 volts. The flag unit also consists of TTL circuitry. It sets a Busy or a Done

FIGURE A-1

Logic circuit of the interface. The boundaries of the three component units are indicated by the faint broken lines. The bars over the signals mean that the lines that come from the computer are normally high, i.e. at +5 volts, and change to low when the signals are put on line. The DATA 8 to 15 lines are abbreviated D8 to D15, the same as DØ.

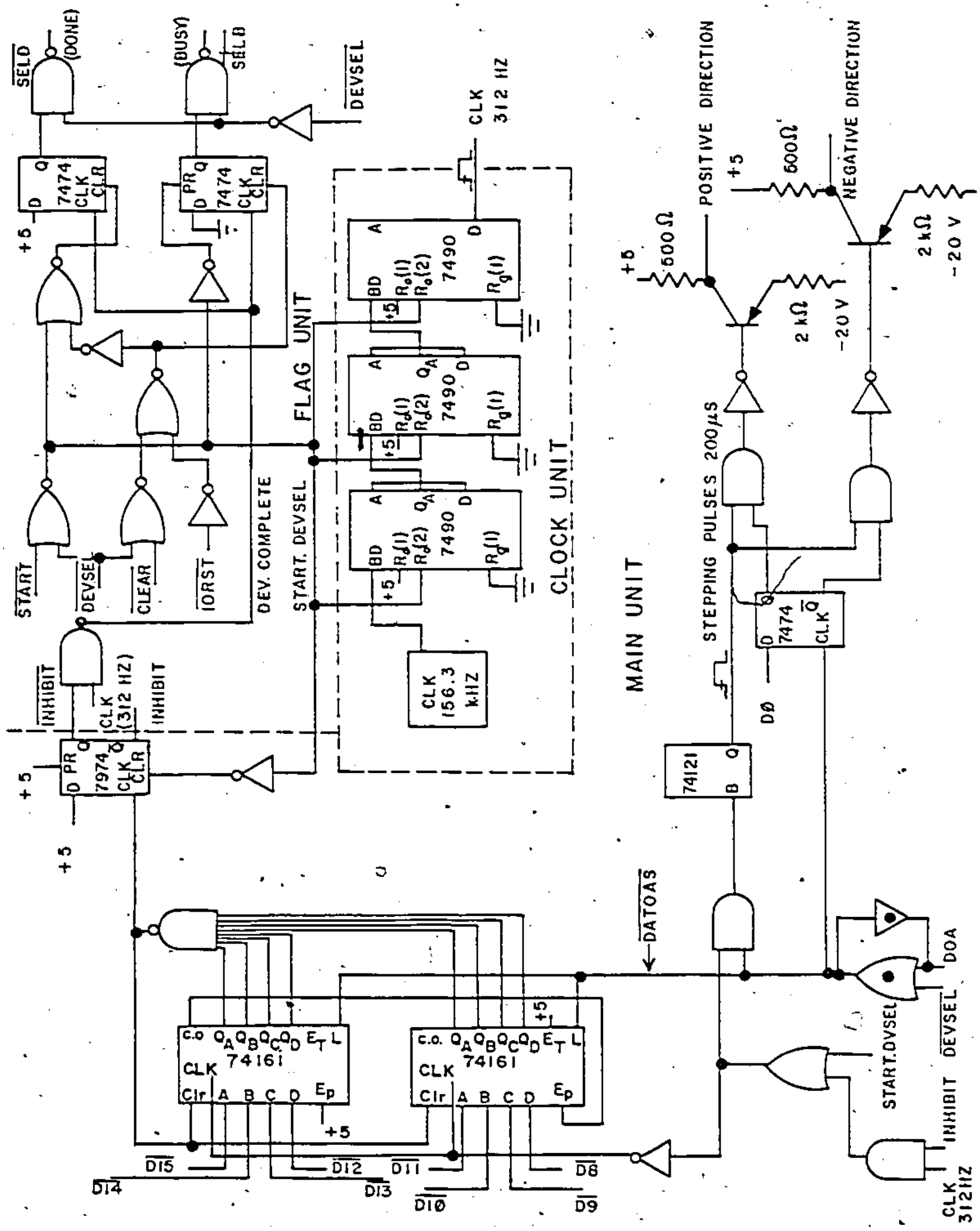
FLAG UNIT
CLOCK UNIT
MAIN UNIT
SELD
(DONE)
(BUSY)
SELB
DEVSEL
7474
7490
7974
74121
74161
CLK 312 HZ
CLK 156.3 kHZ
START
CLEAR
IORST
DEV. COMPLETE
START. DEVSEL
INHIBIT
STEPPING PULSES 200μS
POSITIVE DIRECTION
NEGATIVE DIRECTION
600Ω
2 kΩ
-20 V
+5
DATOAS
DOA
DØ
START.DVSEL
DI5
DI4
DI3
DI2
DI1
DIØ
D9
D8

flag according to the state of the device.

2. Operation

The minicomputer provides a series of signals that are used to transmit or to receive information to or from the interfaces. This is done using a specially designed interface bin unit. The bin receives the signals, buffers them and makes them available to the interface whose code matches the one provided by the minicomputer instruction.

The actual process is as follows: The interface loads the number of steps to be executed, from an accumulator of the computer. This number is put in a series of lines called the data lines in one's complement arithmetic. This corresponds to the inverted binary number. This operation is performed when the instruction DOAS AC, 55 is executed. AC is the accumulator number, 55 the stepping motor interface code. DOAS corresponds to the following signals sent to the interface: DEVSEL, DATOA, START. The sequence of command pulses is illustrated in fig. (2). In the figure it can be seen that the pulse $\overline{\mathrm{DATOA \cdot DEVSEL}}$ (called for short DATOAS) and the $\overline{\mathrm{DATA}}$ signals are latched until the DEVSEL signal is disabled. This operation is a modification of the two first signals as provided by the NOVA-2. The operation is done by the open collector buffer which is connected to the output of the OR gate whose inputs are $\overline{\mathrm{DEVSEL}}$ and $\overline{\mathrm{DATOA}}$, shown at the lower left corner of fig. A-1.

FIGURE A-2

Important signals involved in the operation of the interface. The figure shows the sequence in time of the pulses. The time scale is expanded to the left of the dotted line to exhibit times of the order of nanoseconds. The figure also illustrates how the operation of the interface ceases 3.2 ms after the Inhibit line is disabled.

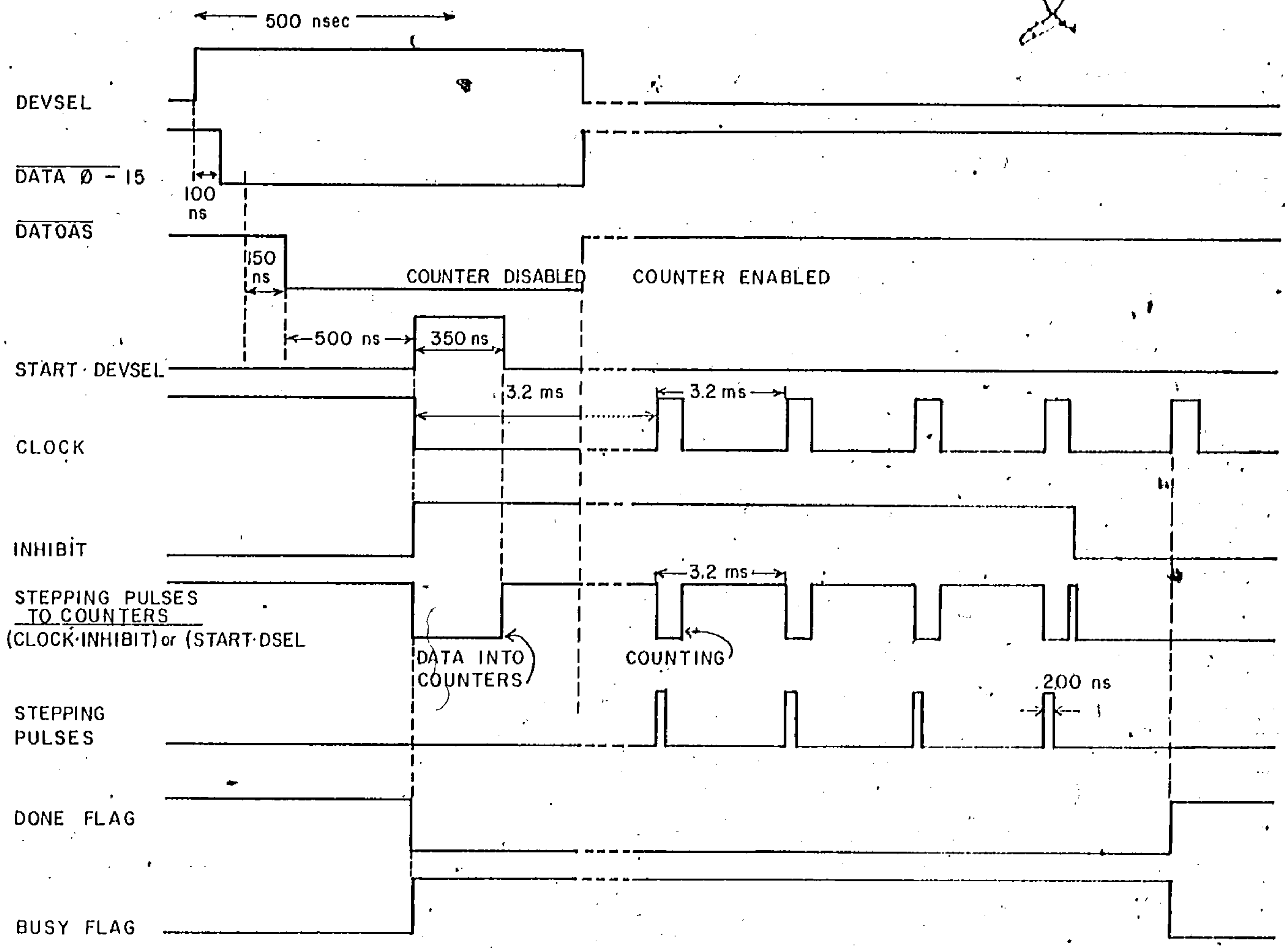
500 nsec
DEVSEL
DATA Ø - 15
100 ns
DATOAS
150 ns
COUNTER DISABLED
COUNTER ENABLED
500 ns
350 ns
START · DEVSEL
3.2 ms
3.2 ms
CLOCK
INHIBIT
3.2 ms
STEPPING PULSES TO COUNTERS
(CLOCK·INHIBIT) or (START·DSEL
DATA INTO COUNTERS
COUNTING
200 ns
STEPPING PULSES
DONE FLAG
BUSY FLAG

```
700   STA     3,777    ;  Store main program source address
701   LDA     Ø,1ØØØ   ;  Load number of steps into Ac. Ø
7Ø2   SKPDN   55       ;  Is Interface Busy?
7Ø3   JMP     .-1      ;  Yes, keep waiting.
7Ø4   DOAS    Ø,55     ;  Transfer from the number of
                          steps to Interface.
7Ø5   JMP     .777     ;  Return to Main program.
1ØØØ  N                ;  Number of steps.
```

APPENDIX B

THE SYMMETRY GROUPS USED TO CLASSIFY EXCITON STATES
-THEIR CHARACTER TABLES AND COMPATIBILITY RELATIONS

1. Introduction

A very compact revision of the space groups used is given. The most important references used for this appendix are Tinkham (1963); and Bassani and Parravicini (1975).

In a crystal, the atoms are arranged in a periodic array, and this fact severely restricts the kind of rotational symmetries that the crystal can have. The complete set of rotations and the inversion operation that leave a crystal invariant, form a group called the point group of the crystal. A crystal also has the basic property of remaining unchanged under lattice translation by

$$\vec{T} = n_1 \vec{a}_1 + n_2 \vec{a}_2 + n_3 \vec{a}_3 \qquad \text{(B-1)}$$

where n_1, n_2, n_3 are integers and $\vec{a}_1$, $\vec{a}_2$, $\vec{a}_3$ are the primitive translations which define the unit cell. The translations (B-1) can be indicated by the symbol $\{E|\vec{T}\}$ where E indicates the identity operation.

The complete set of symmetry operations that leave a crystal unchanged, i.e., the translations, rotations and inversions combined, form a group called the space group of the crystal.

The elements of the space group are going to be denoted by $\{R|\vec{b}\}$ where R is a real orthogonal matrix indicating the proper or improper rotation to execute. An improper rotation consists of a rotation followed by the inversion operation. The vector $\vec{b}$ is given by $\vec{b} = \vec{T} + \vec{f}$, where $\vec{T}$ is a translation vector as (B-1); and $\vec{f}$ is a fractional translation required for some rotations for crystals with a basis of more than one. The application of a symmetry operation $\{R|\vec{b}\}$ to a vector $\vec{d}_i$ determining the positions on the basis of a lattice point in the unit cell gives:

$$\{R|\vec{b}\}\ \vec{d}_i = \vec{d}_j + \vec{T} \qquad \text{(B-2)}$$

where $\vec{T}$ is one of the translation vectors (B-1); and $\vec{d}_j$ specifies an atom of the same kind in the unit cell. If the fractional translations are zero, the space group is said to be symmorphic to the point group.

2. Matrix Representation and Classes of the Group

In a matrix representation, we associate a square matrix $\Gamma(A)$ to each group element, such that:

$$\Gamma(A) \cdot \Gamma(B) = \Gamma(AB) \qquad \text{(B-3)}$$

A matrix representation is called reducible if a similarity transformation exists that simultaneously block diagonalizes all the matrices of the representation in the same way. If no such similarity transformation exists, the representation is called irreducible. In many quantum mechanical applications, each of the irreducible representations will display the transformation properties of a set of degenerate eigenfunctions.

Hence, the number of irreducible representations can give the number of distinct energy levels.

A reducible representation D can always be decomposed in the form:

$$D = \sum_a n_a D^a \tag{B-4}$$

where n_a indicates the number of times the irreducible representation D^a is contained in D, and in group theory is shown to be given by:

$$n_a = \frac{1}{h} \sum_R X^a(R)^* X(R) \tag{B-5}$$

where h is the number of elements in the group; $X^a(R)^*$ is the complex conjugate of the character of the irreducible representation D^a, corresponding to the group element R; and X(R) is the corresponding character of the reducible representation D.

A class is the set of elements obtained by applying all the R elements of the group in a similarity transformation $R\,S\,R^{-1}$ to some group element S. The trace of a matrix is invariant under any similarity transformation. Hence, by definition of class, all elements in the class have the same trace. The character of a matrix representation is defined as the set of traces of all symmetry operations in the group, denoted by X(R). It is customary to specify the character of a representation by simply giving each of the common traces of the operations in a class of the group. This is denoted by $X_k^j(Cn)$ for the kth class in the jth representation.

3. Irreducible Representations of Electron States in the Diamond Structure

As a consequence of the well-known Bloch Theorem, the irreducible representations of the translation group are given by:

$$\{E|\vec{T}\} \text{ is represented by } e^{-i\vec{K}\cdot\vec{T}} \tag{B-6}$$

where the $\vec{k}$ vectors are the ones used to classify the electron states in a crystal, and are defined by:

$$\vec{k} = \frac{m_1}{N_1}\vec{h}_1 + \frac{m_2}{N_2}\vec{h}_2 + \frac{m_3}{N_3}\vec{h}_3 \tag{B-7}$$

where $N_1 N_2 N_3 = N$ is the number of lattice points in the crystal; m_1, m_2, m_3 are integer numbers which satisfy $m_i = 0, 1, \ldots, N_i - 1$; and $\vec{h}_1$, $\vec{h}_2$, $\vec{h}_3$ are the primitive reciprocal lattice vectors.

If the point group operations R are carried successively on some vector $\vec{k}$, it has generated what is known as the star of $\vec{k}$. Values of $\vec{k}$ at some special points of the Brillouin zone and at some special directions will be unchanged under some of the symmetry operations. For $\vec{k}$ vectors on the boundary of the Brillouin zone, the symmetry operations will satisfy the relation:

$$\{R|\vec{K}\} = \vec{K} + \vec{h}. \tag{B-8}$$

This state and the $\vec{k}$ state are identical via the reciprocal lattice vector. These points are of special interest because only there can symmetry based degeneracy exist among functions with the same $\vec{K}$.

The operations R_k that leave $\vec{k}$ unchanged (modulo $\vec{h}$) form a group called the small point group of $\vec{k}$. The symmetry operations $\{R|\vec{b}\}$ formed from these rotations and all the translations constitute a group called the little group of the $\vec{k}$ vector. In order to specify the irreducible representations of the little group, it is sufficient to list the character of the elements of the form $\{R|\vec{f}\}$ since the character of $\{R|\vec{f} + \vec{T}\}$ is $e^{i\vec{k}\cdot\vec{T}}$ x the character of $\{R|\vec{f}\}$.

The diamond space group is the full cubic group O_h. The diamond group is not symmorphic because some of the symmetry operations of the full cubic group O_h appear in the space group associated with the fractional translation $\vec{f} = \frac{a}{4}$ (1,1,1).

<u>The group O_h</u>. The full cubic group O_h is the direct product of the cubic group O with the parity group C_i which consists of the identity and the inversion operation, i.e., $O_h = O \times C_i$. Thus, the full cubic group consists of the following elements grouped in ten classes:

E	the identity.
$8C_3$	rotations by $\frac{2\pi}{3}$ and by $\frac{4\pi}{3}$ around any of the four <111> diagonal axes.
$3C_4^2$	rotations by π around any of the three <100> axes.
$6C_4$	rotations by $\frac{\pi}{2}$ and $\frac{3\pi}{2}$ around the three <100> axes.
$6C_2$	rotations by π around any of the six diad axes <110>.

and five similar classes of improper rotations obtained by multiplying every rotation by the inversion operator. The number in front of the symbol for the operation denotes the number of elements in the class.

In the following presentation of the character tables, only those of the groups involved in the classification of states in indirect excitons in Ge and Si are presented. These are mainly the tables of the additional representations corresponding to the extended double groups of the points Γ and L, and line Δ of the diamond Brillouin zone.

Double Groups. The double groups are introduced to deal with the fact that states of half integer spim change sign when a rotation of 2π is performed. Hence, they are unchanged by 4π rotations. To cope with this situation, the fiction is introduced that the crystal is taken into itself not under a rotation by 2π, but after a rotation of 4π. A new group element, $\overline{E}$, is also introduced, which represents a rotation by 2π and has the property $\{E|\vec{O}\}^2 = \{E|\vec{O}\}$, i.e., the identity. The multiplication of a general rotation operator, R, with the $\{E|\vec{O}\}$ element is denoted by $\{\overline{R}|\vec{O}\}$. In this case, there have to be extra representations to allow for the fact that new elements have been added to the group.

4. Character Tables

In the point Γ on the diamond Brillouin zone, $\vec{k} = \frac{2\pi}{a}(0,0,0)$. The small point group of $\vec{k}$ is the entire group O_h. The characters of the additional irreducible representations of the double group of point Γ are simply given by the characters of the extended point group O_h in Table B-1.

The line Δ is the line running along the <100> direction. Here, $\vec{k} = \frac{2\pi}{a}(\delta,0,0)$, with $0 < \delta < 1$. The small point group of $\vec{k}$ is given by the operations that leave x unchanged. This small group is the group C_{4v}. This group is composed of a four-fold axis along the Δ direction, and four reflection planes at 45° of each other containing the four-fold axis. The irreducible representations of are obtained by multiplying the characters of the irreducible representations of the group C_{4v} by the phase factor $e^{-i\vec{k}\cdot\vec{f}} = e^{-i\pi/2\delta}$. Table B-2 presents the characters of the simple group and Table B-3 lists the characters of the additional representations of the double group.

The point L is at the centre of the hexagonal surface of the B. Zone. Here, $k = \frac{\pi}{a}(1,1,1)$. The small group is the set of rotations that interchange (x,y,z) and the inversion, i.e., it is $D_{3d} = C_{3v} \times C_i$. C_{3v} is a group with a three-fold axis along the <111> diagonal and 3 reflection planes containing this axis at 60° of each other. Table B-4 presents the character table of the simple group, and Table B-5 shows the characters of the additional representations of the double group.

5. Compatibility Relations

Consider a group G and a subgroup S. Given a matrix representation of G, it is possible to choose only those matrices corresponding to the elements of the subgroup S. In this way, we obtain a representation of S. The representation thus obtained for the subgroup is, in general, reducible. This representation can then be decomposed into a number of irreducible representations of the subgroup that are said to be compatible with the irreducible representation of G.

The compatibility relations forthe points Γ, L and Γ and the line Δ, are given in Table B-6. Table B-7 shows the optical transitions allowed for exciton states with symmetry either at the point L or at the Δ line, obtained using the decomposition Equations B-4 and B-5.

Finally, the identification of angular momentum states that belong to a given double group representation of Table 3-4 can be worked out from the tables of the work "symmetry adapted functions for double groups II. Cubic point groups" by Cracknell and Joshua (1970).

Table B-1 Additional irreducible representations of the double group of k, at point Γ of the diamond structure.

Point Γ	E	$\bar{E}$	$3C_4^2$ $3\bar{C}_4^2$	$6C_4$	$6\bar{C}_4$	$6C_2$ $6\bar{C}_2$	$8C_3$	$8\bar{C}_3$	I	$\bar{I}$	$3IC_4^2$ $3I\bar{C}_4^2$	$6IC_4$	$6I\bar{C}_4$	$6IC_2$ $6I\bar{C}_2$	$8IC_3$	$8I\bar{C}_3$
Γ_6^+	2	-2	0	$\sqrt{2}$	$-\sqrt{2}$	0	1	-1	2	-2	0	$\sqrt{2}$	$-\sqrt{2}$	0	1	-1
Γ_7^+	2	-2	0	$-\sqrt{2}$	$\sqrt{2}$	0	1	-1	2	-2	0	$-\sqrt{2}$	$\sqrt{2}$	0	1	-1
Γ_8^+	4	-4	0	0	0	0	-1	1	4	-4	0	0	0	0	-1	1
Γ_6^-	2	-2	0	$\sqrt{2}$	$-\sqrt{2}$	0	1	-1	-2	2	0	$-\sqrt{2}$	$\sqrt{2}$	0	-1	1
Γ_7^-	2	-2	0	$-\sqrt{2}$	$\sqrt{2}$	0	1	-1	-2	2	0	$\sqrt{2}$	$-\sqrt{2}$	0	-1	1
Γ_8^-	4	-4	0	0	0	0	-1	1	-4	4	0	0	0	0	1	-1

The notations are taken from R.J. Elliott, (1954).

The first column lists the representations. The rest list the characters of the classes.

Table B-2 Irreducible representations on symmetry line Δ of the diamond structure.

Representation	$\{E\|0\}$	$\{\delta_{2x}\|0\}$	$\{\delta_{4x}^{-1}\|f\},\{\delta_{4x}\|f\}$	$\{I\delta_{2z}\|f\},\{I\delta_{2y}\|f\}$	$\{I\delta_{2yz}\|0\},\{I\delta_{2y\bar{z}}\|0\}$
Δ_1	1	1	$e^{-i\pi/2\delta}$	$e^{-(\pi/2)\delta}$	1
Δ_1^1	1	1	$e^{-i\pi/2\delta}$	$e^{-i(\pi/2)\delta}$	-1
Δ_2	1	1	$-e^{-i\pi/2\delta}$	$e^{-i(\pi/2)\delta}$	-1
Δ_2^1	1	1	$-e^{-i\pi/2\delta}$	$-e^{-i\pi/2\delta}$	1
Δ_5	2	-2	0	0	0

The rotation operations are denoted in the crystallographic notation. An example illustrates well its meaning. For instance, $I\delta_{2x\bar{z}}$ represents a rotation by $2\pi/2$ about the axis whose director cosines on the x,y,z axis are $\bar{1}$, 0, $\underline{1}$. The I denotes that an inversion follows this rotation.

Table B-3 Additional irreducible representations of the double group of k, on line Δ of the diamond structure.

Line Δ	$\{E\|0\}$	$\{\bar{E}\|0\}$	$\{\delta_{2x},\bar{\delta}_{2x}\|0\}$	$\{\delta_{4x}^{-1},\delta_{4x}\|f\}$	$\{\bar{\delta}_{4x}^{-1},\bar{\delta}_{4x}\|f\}$	$\{I\delta_{2x},I\delta_{2\underline{y}},I\bar{\delta}_{2z},I\bar{\delta}_{2\underline{y}}\|f\}$	$\{I\delta_{2\underline{y}\bar{z}},I\delta_{2yz},I\bar{\delta}_{2\underline{y}z},I\bar{\delta}_{2\underline{y}\bar{z}}\|0\}$
Δ_6	2	−2	0	$\sqrt{2}e^{-i(\pi/2)\delta}$	$-\sqrt{2}e^{-i(\pi/2)\delta}$	0	0
Δ_7	2	−2	0	$-\sqrt{2}e^{-i(\pi/2)\delta}$	$\sqrt{2}e^{-i(\pi/2)\delta}$	0	0

The notations are taken from R.J. Elliott (1954). The first column labels the representations. The characters are given in all the other columns.

Table B-4 Irreducible representations at symmetry point L of the diamond structure.

Point L	$\{E\|0\}$	$\{\delta^{-1}_{3xyz}\|0\}$ $\{\delta_{3xyz}\|0\}$	$\{I\delta_{2x\bar{y}}\|0\}$ $\{I\delta_{2\bar{x}z}\|0\}$ $\{I\delta_{2y\bar{z}}\|0\}$	$\{I\|f\}$	$\{I\delta^{-1}_{3xyz}\|0\}$ $\{I\delta_{3xyz}\|0\}$	$\{\delta_{2x\bar{y}}\|0\}$ $\{\delta_{2\bar{x}x}\|0\}$ $\{\delta_{2y\bar{z}}\|0\}$
L_1	1	1	1	1	1	1
L_2	1	1	-1	1	1	-1
L_3	2	-1	0	2	-1	0
L_1^1	1	1	1	-1	-1	-1
L_2^1	1	1	-1	-1	-1	1
L_3^1	2	-1	0	-2	1	0

Table B-5 Additional irreducible representations of the double group of k at point L of the diamond structure.

Point L	$\{E\|0\}$	$\{\bar{E}\|0\}$	$\{\delta^{-1}_{3xyz}\|0\}$ $\{\delta_{3xyz}\|0\}$	$\{\bar{\delta}_{3xyz}\|0\}$ $\{\bar{\delta}_{3xyz}\|0\}$	$\{I\delta_{2x\bar{y}}\|0\}$ $\{I\delta_{2\bar{x}z}\|0\}$ $\{I\delta_{2y\bar{z}}\|0\}$	$\{I\bar{\delta}_{2x\bar{y}}\|0\}$ $\{I\bar{\delta}_{2\bar{x}z}\|0\}$ $\{I\bar{\delta}_{2y\bar{z}}\|0\}$	$\{I\|f\}$	$\{\bar{I}\|f\}$	$\{I\delta^{-1}_{3xyz}\|f\}$ $\{I\delta_{3xyz}\|f\}$	$\{I\bar{\delta}^{-1}_{3xyz}\|f\}$ $\{I\bar{\delta}_{3xyz}\|f\}$	$\{\delta_{2x\bar{y}}\|f\}$ $\{\delta_{2\bar{x}z}\|f\}$ $\{\delta_{2y\bar{z}}\|f\}$	$\{\bar{\delta}_{2x\bar{y}}\|f\}$ $\{\bar{\delta}_{2\bar{x}z}\|f\}$ $\{\bar{\delta}_{2y\bar{z}}\|f\}$
L_4^+	1	-1	-1	1	i	-i	1	-1	-1	1	i	-i
L_5^+	1	-1	-1	1	-i	i	1	-1	-1	1	-i	i
L_6^+	2	-2	1	-1	0	0	2	-2	1	-1	0	0
L_4^-	1	-1	-1	1	i	-i	-1	1	1	-1	-i	i
L_5^-	1	-1	-1	1	-i	i	-1	1	-1	-1	i	-i
L_6^-	2	-2	1	-1	0	0	-2	2	-1	1	0	0

The first column labels the representations. The characters are given in all other columns. The notations are taken from R.H.Parmenter (1955).

Table B-6 Compatibility relations between the additional irreducible representations of the double groups of $\vec{k}$ used in this work, at symmetry points Γ, L and line Δ.

Point Γ	Γ_6^+	Γ_7^+	Γ_8^+	Γ_6^-	Γ_7^-	Γ_8^-
Line Δ	Δ_6	Δ_7	$\Delta_6+\Delta_7$	Δ_6	Δ_7	$\Delta_6+\Delta_7$
Point Γ	Γ_6^+	Γ_7^+	Γ_8^+	Γ_6^-	Γ_7^-	Γ_8^-
Point L	L_6^+	L_6^+	$L_4^++L_5^++L_6^+$	L_6^-	L_7^-	$L_4^-+L_5^-+L_6^-$

This table and $\Gamma_{15} \otimes \Gamma_8^+ = \Gamma_6^- + \Gamma_7^- + 2\Gamma_8^-$ give the group classification of P states of indirect exciton in Ge and Si, as discussed at the end of Chapter III.

Table B-7 Allowed optical transitions at the high symmetry point L and line Δ of the Brillouin Zone for the diamond structure. Only the representations used for the indirect excitons in Ge and Si are entered in the table.

Dipole Operator Representation				
Point L	L_i:	L_4^+	L_5^+	L_6^+
$L_1^1+L_3^1$	$L_i \otimes (L_1^1+L_3^1)$:	$L_4^-+L_6^-$	$L_5^-+L_6^-$	$L_4^-+L_5^-+L_6^-$
Line Δ	Δ_i	Δ_6		Δ_7
$\Delta_1+\Delta_5$	$\Delta_i \otimes (\Delta_1+\Delta_5)$:	$2\Delta_6+\Delta_7$		$\Delta_6+2\Delta_7$

In the first column, the representation of the small group of $\vec{k}$ according to which the electromagnetical dipole operator transforms is given. In the other columns, the decomposition of the product representation is given.

APPENDIX C

EVALUATION OF THE ENERGY MATRIX OF THE MAGNETIC EXCITON HAMILTONIAN

In terms of the angular momentum $\vec{F} = \vec{L} + \vec{J}$ the magnetic Hamiltonian (4-6) can be written as

$$H_{mag} = -g_e \vec{L}\cdot\vec{h} + g_h \vec{F}\cdot\vec{h} - g_e \vec{S}_e\cdot\vec{h}. \quad \text{(C-1)}$$

Under the assumptions discussed in chapter four, the wavefunction can be written as

$$\Psi_\pm = \sum_i a_i |n, L^i, J, F^i, F_z^i> \alpha_\pm . \quad \text{(C-2)}$$

The subscript plus or minus (±) represents the electron spin component up or down respectively and a_i is the square root of the normalized percentage contribution to the state nL_{F_z} to the probability amplitude. Then it is necessary to calculate the following matrix elements:

$$<nL'JF',F_z'|F_z|nLJF,F_z> = \delta_{FF'}\delta_{F_z'F_z} hF_z \quad \text{(C-3)}$$

$$<nL'JF',F_z'|L_z|nLJF,F_z> \quad \text{(C-4)}$$

and sum all contributions from the state participating in (C-2). The term which involves the spin of the electron gives a constant contribution for all the exciton states, and in principle it will have to be added to all diagonal matrix elements. But this is equivalent to performing an energy shift for the zero of energy and hence it is equivalent to the addition of a constant diagonal matrix to the energy matrix. Then it does not have any effect at all in the diagonalization. To include, then, its contribution to the eigenergies of the full magnetic Hamiltonian, it is necessary to add $\pm 0.5\ g_e \beta |\vec{h}|$ for $S_e = \mp \frac{1}{2}$ to all of them. This result is a consequence of the non participation of the electron spin in any coupling scheme, and not from any of the approximations used in this work. This has a very important effect on the spectrum. The electron spin does not flip in dipolar transitions, hence as a consequence of the constant contribution to the energy for all levels of the spin, the energy of these transitions will be the same independently of the spin state of the electron.

The matrix element (C-4) can be valuated using the Wigner-Eckhart theorem and the 3-j and 6-j symbols to calculate the reduced matrix element in the coupled scheme $\vec{F} = \vec{L} + \vec{J}$, as described by (Edmonds 1974):

$$\langle nL'JF'F_z'|L_z|nLJFF_z\rangle = (-1)^{L+J+1-F_z+F'+F}\langle n'L'||L||nL\rangle$$
$$\times\ [(2F+1)(2F'+1)]^{1/2}\begin{pmatrix} F' & 1 & F \\ -F_z' & 0 & F_z \end{pmatrix}\begin{Bmatrix} L' & F' & J \\ F & L & 1 \end{Bmatrix} . \qquad \text{(C-5)}$$

The Wigner or 3-j symbol $\begin{pmatrix} F' & 1 & F \\ -F_z' & 0 & F_z \end{pmatrix}$ is different from zero only for $F_z' = F_z$ and $F = 1,0,-1$. The reduced matrix element $\langle n'L'||L||nL\rangle$

can be also calculated using the Wigner-Eckhart theorem in the L space:

$$\langle n'L'M_L'|L_z|nLM_L\rangle(-1)^{L-M_L}\begin{pmatrix} L' & 1 & L \\ -M_L' & 0 & M_L \end{pmatrix}\langle n'L'||L||nL\rangle \qquad \text{(C-6)}$$

where L_z corresponds to the zero component of the spherical vector operator L. Using

$$\langle n'L'M_L'|L_z|nLM_L\rangle = \delta_{M_LM_L'}\ \delta_{nn'}\ \delta_{LL'}\ \hbar M_L \qquad \text{(C-7)}$$

Choosing $M_L' = M_L = L$ and using

$$\begin{pmatrix} L & 1 & L \\ -L & 0 & L \end{pmatrix} = \frac{1}{(2L+2)^{1/2}}\left[\frac{(2L)!(2L)!}{(2L+1)!(2L-1)!}\right]^{1/2} \qquad \text{(C-8)}$$

the value of the reduced matrix can finally be written

$$\langle n'L'||L|nL\rangle = \delta_{nn'}\delta_{LL'}\ \hbar[L(L+1)(2L+1)]^{1/2} \qquad \text{(C-9)}$$

which imposes the condition that only matrix elements with n=n', L=L' can be different from zero. Using the result (C-9) one is left only with the two following different matrix elements to calculate:

$$\langle nLJFF_z|L_z|nLJFF_z\rangle = 1 + \frac{L(L+1)}{F(F+1)} - \frac{15}{4F(F+1)} \qquad \text{(C-10)}$$

$$< nLJ,F+1,F_z|L_z|nLJ,F,F_z> = \tag{C-11}$$

$$\hbar\left[\frac{(F+F_z+1)(F-F_z+1)(L+J+F+2)(L+F+1-J)(J+F+1-L)(L+J-F)}{(2F+1)(2F+2)^2(2F+3)}\right]^{1/2}$$

where the tables for the 3-j and 6-j symbols in Edmonds were used. In (C-10) the substitution $J = 3/2$ has been done already. These diagonal elements can be calculated in a more straightforward way using $(L+J)^2 = F^2$ and the Wigner-Eckhart theorem, or even the vector model. The contribution of the exciton Hamiltonian H_{ex} $(h = 0)$, is only different from zero for the diagonal terms and was added in consequence, before proceeding to perform the diagonalization.

BIBLIOGRAPHY

1. Altarelli, M. and Lipari, N.O., Phys. Rev. B, 7, 3798, 1973.

2. Altarelli, M. and Lipari, N.O., Phys. Rev. B, 9, 1733, 1974.

3. Altarelli, M. and Lipari, N.O., Phys. Rev. B, 15, 4898, 1977.

4. Baldereschi, A. and Lipari, N.O., Phys. Rev. B, 8, 2693, 1973.

5. Baldereschi, A. and Lipari, N.O., Phys. Rev. B, 9, 1525, 1974.

6. Bassani, F. and Parravicini, P.G., Electronic States and Optical Transitions in Solids. Edited by R.A. Ballinger, Pergamon Press, New York, 1975.

7. Baym, G., Lectures on Quantum Mechanics, Benjamin, London, 1974.

8. Bell, R.J., Introducing Fourier Transform Spectroscopy, Academic Press, New York, 1972.

9. Bethe, H.A. and Salpeter, E.E., Quantum Mechanics of One-and-two-electron Atoms, Academic Press, New York, 1957.

10. Brinkman, W.F. and Rice, T.M., Phys. Rev. B, 7, 1508, 1973.

11. Buchanan, M. and Timusk, T., Proceedings of the 13th International Conference on the Physics of Semiconductors, Rome. Edited by F.G. Fumi, 1976.

12. Burstein, E., Physics of Solids in Intense Magnetic Fields. Chania, Greece. Edited by E.D. Haidemenakis, Plenum Press, New York, 1969.

13. Button, K.J., Roth, L.M., Kleiner, W.K., Zwerdling, S. and Lax, B., Phys. Rev. Lett., 2, 161, 1959.

14. Capizzi, M., Voos, M., Benoit a la Guillaume, C., and McGroddy, J.C., Solid State Commun., 16, 709, 1975.

15. Cardona, M., Proceedings of the Enrico Fermi School of Physics. 52nd course on atomic structure and properties of solids, p. 514, 1972.

16. Collet, J., Pugnet, M., Barrau, J., Brousseau, M. and Maaref, H., Solid State Commun., 24, 335, 1977.

17. Combescot, M. and Nozieres, P., Solid State Commun., 10, 301, 1972.

18. Cracknell, A.P. and Joshua, S.J., Proc. Camb. Phil. Soc., 67, 647, 1970.

19. Cuthbert, J.D., Phys. Rev. B. 1, 1552, 1970.

20. Dimmock, J.O., Semiconductors and Semimetals, Vol. 3, 259, 1967. Edited by R.K. Willardson and A.C. Beer, Academic Press, New York, 1967.

21. Dite, A.F., Lysenko, V.G. and Timofeev, V.B., Physics Status Solidi (b), 66, 53, 1974.

22. Dite, A.F., Kulakovskii, V.D. and Timofeev, V.B., Zh. Eksp. Teor. Fis., 72, 1156, 1976. (Sov. Phys. JETP 45, 604, 1977).

23. Dresselhauss, G., Kip, A.F. and Kittel, C., Phys. Rev. 95, 568, 1954.

24. Dresselhauss, G., J. Phys. Chem. Solids, 1, 14, 1956.

25. Drew, D.H. and Sievers, A.J., J. Appl. Optics, 8, 2067, 1967.

26. Edmonds, A.R., Angular Momentum in Quantum Mechanics. Princeton, New Jersey, 1974.

27. Ehrenreich, H. and Cohen, M.H., Phys. Rev., 115, 786, 1959.

28. Elliot, R.J., Phys. Rev., 96, 130, 1954.

29. Elliot, R.J., Phys. Rev., 96, 268, 1954.

30. Frova, A., Thomas, G.A., Miller, R.E. and Kane, E.O., Phys. Rev. Lett., 34, 1572, 1975.

31. Gershenzon, E.M., Goltsman, G.N. and Ptitsina, N.G., Sov. Phys. JETP, 43, 116, 1976.

32. Hammond, T.C., McGill, T.C. and Mayer, J.W., Phys. Rev. B, 13, 3566, 1976.

33. Hammond, R.B. and Silver, R.N., Solid State Commun., 28, 993, 1978.

34. Hensel, J.C. and Feker, G., Phys. Rev. B, 3, 2623, 1971.

35. Hensel, J.C. and Suzuki, K., Phys. Rev. B, 9, 4219, 1974.

36. Hensel, J.C., Phillips, T.G. and Thomas, G.A., Solid State Physics, Vol. 32, 88. Edited by H. Ehrenreich, F. Seitz and D. Turnbull, Academic Press, New York, 1976.

37. Herman, F., Proc. Inst. Radio Engrs., 43, 1703, 1955.

38. Hutchings, M.T., Solid State Physics, Vol. 16. Edited by F. Seitz and D. Turnbull, Academic Press, N.Y., 1964.

39. Irvin, J.C., Bell Syst. Tech. J., 41, 387 1962.

40. Johnson, E.J., Proceedings of the 9th Int. Conf. on the Physics of Semiconductors, Moscow, 1968. Edited by S.M. Ryvkin, Nauka, Leningrad.

41. Keldysh, L.V., Proceedings of the 9th Int. Conf. on the Physics of Semiconductors, Moscow, 1968. Edited by S.M. Ryvkin, Nauka, Leningrad.

42. Kerker, M., The Scattering of Light and Other Electromagnetic Radiation. Academic Press, New York, 1969.

43. Kittel, C., Quantum Theory of Solids. Wiley, New York, 1963.

44. Knox, R.S., Solid State Physics, Supp. 5. Edited by F. Seitz and D. Turnbull, Academic Press, New York, 1963.

45. Kobayaski, M., and Narita, S., Physics of Highly Excited Solids. Edited by M. Veta and Y. Nishina, Springer, New York, 1976.

46. Kononenko, V.L., Mandel'shtam, T.S., Murzin, V.N., Vavilov, V.S. and Zayats, V.A., Proceedings of the 12th Int. Conf. of the Physics of Semiconductors, Stuttgart, 1974. Edited by M.H. Pilkuhn.

47. Koster, G.F., Solid State Physics, Vol. 5. Edited by F. Seitz and D. Turnbull, Academic Press, New York, 1957.

48. Lipari, N.O. and Baldereschi, A., Phys. Rev. 3, 2497, 1971.

49. Lipari, N.O. and Altarelli, M., Solid State Commun., 12, 1137, 1976.

50. Lipari, N.O. and Altarelli, M., Phys. Rev. B, 3, 439, 1971.

51. Lipari, N.O., Altarelli, M. and Tosatti, E., Solid State Commun., 21, 979, 1977.

52. Lipari, N.O. and Altarelli, M., Bull. Amer. Phys. Soc., 23, 426, 1978.

53. Luttinger, J.M. and Kohn, W., Phys. Rev., 97, 869, 1955.

54. Luttinger, J.M., Phys. Rev., 102, 1030, 1956.

55. MacFarlane, G.G., McLean, T.P., Quarrington, J.E. and Roberts, V., Phys. Rev., 108, 1377, 1957.

56. MacFarlane, G.G., McLean, T.P., Quarrington, J.E. and Roberts, V., J. Phys. Chem. Solids, 8, 397, 1959.

57. McLean, T.P. and Loudon, R., J. Phys. Chem. Solids, 13, 1, 1960.

58. Muro, K. and Nisida, Y., J. Phys. Soc., Japan, 40, 1069, 1976.

59. Murzin, V.N., Fiz. Tekh. Poluprov., 7, 1610, 1973. (Sov. Phys. Semicond., 7, 1074).

60. Murzin, V.N., Zayats, V.A. and Kononenko, V.L., Fiz. Tverd. Tela, 17, 2684, 1975. (Sov. Phys. Solid State, 17, 1783, 1976).

61. Parmenter, R.H., Phys. Rev., 100, 573, 1955.

62. Pokrovskii, Ya. and Svistunova, K., Zh. Eksper. Tear. Fiz. Pisma, 9, 435, 1969.

63. Pokrovskii, Ya., Phys. Status Solidi (a), 11, 385, 1972.

64. Rice, T.M., Bull. Amer. Phys. Soc., 20, 470, 1975.

65. Rose, J.H. and Shore, H.B., Bull. Amer. Phys. Soc., 20, 470, 1975.

66. Roth, L.M. and Lax, B., Phys. Rev. Lett., 3, 217, 1959.

67. Shah, J., Dayem, A.H. and Combescot, M., Solid State Commun., 24, 71, 1977.

68. Shaklee, K.H. and Nahory, R.E., Phys. Rev. Lett., 24, 942, 1970.

69. Shinada, M. and Sugano, S., J. Phys. Soc. Japan, 21, 1936, 1966.

70. Thewalt, M.L., M.Sc. Thesis, University of British Columbia, 1975.

71. Timusk, T. and Silin, A., Phys. Status Solidi (b), 69, 87, 1975.

72. Timusk, T., Phys. Rev. B, 13, 3511, 1976.

73. Timusk, T., Navarro, H., Lipari, N.O. and Altarelli, M., Solid State Commun., 25, 217, 1978.

74. Tinkham, M., Group Theory and Quantum Mechanics. McGraw-Hill, New York, 1963.

75. Vavilov, V.S., Guzeev, N.V., Zayats, V.A., Kononenko, V., Mandel'shtam, T.S. and Murzin, V.N., Sov. Phys. JETP Lett. 17, 345, 1973.

76. Vavilov, V.S., Zayats, V.Z. and Murzin, V.N., Sov. Phys. JETP Lett., 10, 1950, 1969.

77. Vavilov, V.S., Zayats, V.A. and Murzin, V.N., Proceedings of the 10th Int. Conf. on the Physics of Semiconductors, Cambridge, England. Edited by S.P. Keller, J.C. Hensel and F. Stern (NBS, Springfield, Va.), 1970.

78. Westervelt, R.M., Phys. Stat. Sol. (b), 74, 727, 1976.

79. Westervelt, R.M., Private Communication to T. Timusk, 1979.

80. Zarate, H.G. and Timusk, T., Phys. Rev. B, 19, 5223, 1979.